Silicon-Germanium Interdiffusion and Its Impacts on Enhanced Mobility MOSFETs

by

Guangrui Xia

M. Eng., Materials Science and Engineering,
Cornell University, Aug. 2000
M. S., Electrical Engineering,
Massachusetts Institute of Technology, Aug. 2003

Submitted to the Department of Electrical Engineering and Computer Science in Partial Fulfillment of The Requirements for the Degree of
Doctor of Philosophy in Electrical Engineering

at the

Massachusetts Institute of Technology

April 2006

© 2006 Massachusetts Institute of Technology
All rights reserved

Signature of Author…………………………………………………………...……………
Department of Electrical Engineering and Computer Science
April 25, 2006

Certified by……………………………………………………………...………….…………
Judy L. Hoyt
Professor of Electrical Engineering and Computer Science
Thesis Supervisor

Accepted by…………………………………………………..…………………….………
Arthur C. Smith
Chairman, Department Committee on Graduate Students
Department of Electrical Engineering and Computer Science

Silicon-Germanium Interdiffusion and Its Impacts on Enhanced Mobility MOSFETs

by

Guangrui Xia

Submitted to the Department of Electrical and Computer Engineering on April 28, 2006 in Partial Fulfillment of the Requirements for the Degree of Doctor of Philosophy in Electrical Engineering.

Abstract

As complementary metal-oxide-semiconductor field-effect transistors (MOSFETs) scale, strained Si and SiGe technology have received more attention as a means of enhancing performance via improved carrier mobility. One of the biggest challenges for strained Si and SiGe technology is Si-Ge interdiffusion during thermal processing.

Two different aspects of Si-Ge interdiffusion are explored in this work. The first part of this work demonstrates that Si-Ge interdiffusion and ion implantation damage during the fabrication of strained Si MOSFETs have significant impact on electron mobility and thus device performance. Long channel n-MOSFETs with different thermal processing and implant conditions were fabricated on both CZ Si wafers and strained Si/relaxed $Si_{0.8}Ge_{0.2}$ heterostructures. In order to avoid scattering by ionized dopant impurities, neutral Si and Ge were implanted into the channel at six different doses ranging from 4 x 10^{12} cm^{-2} to 1 x 10^{15} atoms/cm^2. It is shown that the mobility enhancement factor is degraded by RTA and ion implantation. For each RTA condition, there is a threshold implantation dose, above which the strained Si mobility starts to degrade significantly. The degradation is larger for devices with higher thermal budgets or implantation doses. Si-Ge interdiffusion at the strained Si/relaxed $Si_{0.8}Ge_{0.2}$ interface was found to be the major mobility degradation mechanism for devices with higher thermal budget, while for devices with lower thermal budget, residual ion implantation damage in the strained Si channel is considered to be the key degradation mechanism.

Two-dimensional simulations are performed to generate as-implanted damage profiles of 30-nm scale MOSFETs. By comparing the 2D damage profiles with those generated by Si blanket implants, it is shown that 30-nm p-MOSFETs are more likely to suffer from mobility degradation than n-MOSFETs.

The second part of this work, which is the main focus of this thesis, systematically investigated the Si-Ge interdiffusivity in epitaxial strained Si/$Si_{1-y}Ge_y$/strained Si/relaxed $Si_{1-x}Ge_x$ and strained Si/relaxed $Si_{1-x}Ge_x$ heterostructures for Ge fractions between 0 and 0.56 over the temperature range of 770 – 920 ºC. Based on the interdiffusivity extracted from experiments, an analytic model was established for interdiffusion simulation. To the best of our knowledge, this work is the most complete study of Si-Ge interdiffusion and modeling to date.

Boltzmann-Matano analysis was applied to extract interdiffusivity from the diffused Ge profiles of strained Si/relaxed $Si_{1-x0}Ge_{x0}$ heterostructures. A model for the interdiffusivity suitable for use in the process simulator TSUPREM-4 was formulated. Si-Ge interdiffusivity was found to increase by 2.2X for every 10% increase in Ge fraction for interdiffusion under relaxed strain. Significantly enhanced Si-Ge interdiffusion was observed in $Si_{1-y}Ge_y$ layers under biaxial compressive strain. Si-Ge interdiffusivity was found to increase by 4.4X for every 0.42% increase in the magnitude of compressive strain, which is equivalent to 10% decrease in the substrate Ge fraction x_0. These results were incorporated into an interdiffusion model that successfully predicts the interdiffusion of various SiGe heterostructures. Examples of the impact of interdiffusion on device design and process integration issues were given.

Thesis Supervisor: Professor Judy L. Hoyt

Title: Professor of Electrical Engineering and Computer Science

Acknowledgements

Upon the completion of this work, I finally have the chance to acknowledge the contributions and express my deep appreciation for many people who have been helpful and supportive for my work and myself along the way. Without them, this work would not have been possible.

My advisor Professor Judy Hoyt has given me the biggest help and encouragement for my work. It was she who introduced me to the research of strained Si and SiGe technology, and helped me to build up the knowledge and skills almost from scratch. She is always patient and enthusiastic to explain and discuss the problems with me both on the theoretical part and experimental details. She is always there to help no matter how busy she is or how trivial the problem is. With her intelligence, diligence, perseverance, and enthusiasm, she has set a good example for us to learn from. Working with her not only taught me how quality research is achieved, but also how an excellent researcher is made.

I wish to thank Professor Dimitri A. Antoniadis and Professor Akintunde I. Akinwande for being my thesis committee members and giving me many good comments and suggestions. I would like to thank Professor George Malliaras, my advisor at Cornell University, for his generous help in the first year of my graduate study.

Many people in the Microsystems Technology Laboratory (MTL) have contributed their expertise to this work. Hasan Nayfeh together with many of my fellow students in the MTL such as Keith Jackson, Jim Fiorenza, Isaac Lauer, Andy Fan, John Kymisis, Athony Lochfield, Ali Khakifirooz and Larry Lee have given me the greatest help on device fabrication and measurement. I am deeply indebted to Hasan for using his processing flow, which I modified for my work, and for using his mask set and lots of useful discussions with him on all aspects of the research. Thanks to all MTL staff who not only trained me on the tools, but also shared their experience with me. I especially

wish to thank Paul Tieney for his help on the lithography tools, Bernard Alamariu for his help on the diffusion tubes, Kurt Broderick for his help on TRL tools. Thanks to all my fellow students in Hoyt group and MTL labmates: Cait, Dennis, Gary, Ingvar, Kusokari, Leo, Liangyu, Luis, MK, Muyiwa, Niamh, Nisha, Nicole, Pouya, Satoshi, Tonya, our assistants Celia, Lindsay, Rose and Debb: you make the lab and building 39 so enjoyable. I would like to thank Professor Robert Hull, Dr. Dalaver H. Anjum and Dr. Jian Li at University of Virginia for their TEM work and discussions, Dr. Ken Rim at IBM for his help and lots of good suggestions, Dr. M. J. Lee from Professor Fitzgerald's group for providing epitaxial wafers and help on TEM imaging, and Dr. M. Canonico at Freescale Semiconductor for Raman measurements. Cait and Nisha proofread the thesis for me; thanks a lot.

Outside the lab, I would like to thank my friends Lei Zuo, Yani Qian, Jianyi Cui, Hao Wang, Hui Wang, Gen Pei, Liangyu Chen, Ling Chao, Hsin-Ni Ho, Xuan Zhang and my undergraduate classmates of Tsinghua University for their friendship. It is so nice to have friends like you.

My family has given me so much love and warmth. I would like to express my deepest gratitude and love to them by dedicating this thesis to them. My parents, Weiqi Xia and Guiying Zhao, have sacrificed so much of their own for me to grow up in a healthy and caring environment and get the best education. They are the first and most important teachers to me. My sister Guanghua has always been a caring sister and the pillar of support for me since I was young. Now she takes all the family responsibilities when I am studying abroad. My husband Xiaodong Lu has brought his love, care and a home to me. My family has been my emotional rock and source of happiness for so many years. Thanks a lot. I wish all of you healthy and happy forever.

To Dad, Mom, sister and Xiaodong

献给爸爸, 妈妈, 姐姐和笑冬

Contents

Abstract 3
Acknowledgements 5
To Dad, Mom, sister and Xiaodong 7
Contents 9
List of Figures 11
List of Tables 17

CHAPTER 1 Introduction 19
1.1 Strained Si and SiGe CMOS Technology 21
1.1.1 Process-induced Strain and Global Strain by Epitaxy 21
1.1.2 Heterostructure Based Enhanced Mobility MOSFETs 23
1.1.3 Mobility Enhancement 26
1.2 Direction and Organization of Thesis 30
1.3 Chapter Summary 31

CHAPTER 2 Impact of Thermal Processing and Ion Implantation on the Mobility Enhancement in Strained Si *n*-MOSFETs 33
2.1 Introduction to the Processing of Si/SiGe 34
2.1.1 Critical Thickness and Strain Relaxation in Strained $Si/Si_{1-x}Ge_x$ 34
2.1.2 Strain Relaxation and Thermal Stability of Strained $Si_{1-x}Ge_x/Si$ 36
2.1.3 Background on Processing Influence on Mobility Enhancement in Strained Si 37
2.2 Experiment Design and Fabrication 40
2.3 Electrical Characteristics and Medici Simulations 45
2.4 Mobility Dependence on Processing Factors 49
2.5 Mobility Degradation Mechanisms 56
2.6 Impact on Technology 63
2.7 Chapter Summary 65

CHAPTER 3 Si-Ge Interdiffusivity Extraction from Experiment: Boltzmann-Matano Analysis 67
3.1 Introduction to Si-Ge Interdiffusion 67
3.1.1 SiGe Devices and Motivation for this Work 67
3.1.2 Literature Overview 69
3.2 Interdiffusivity Extraction Method: Boltzmann-Matano Analysis 71
3.3 Epitaxial Structure Design and Growth 75
3.4 Practical Application of Boltzmann-Matano analysis 78
3.4.1 Initial Verification and Example of Boltzmann-Matano Analysis 78
3.4.2 Pseudo-Boltzmann-Matano analysis 80
3.4.3 Error from SIMS Broadening Effect 82
3.5 Experiment Matrix Design 85
3.6 Summary of Extracted Interdiffusivity 88
3.7 Chapter Summary 90

CHAPTER 4 Si-Ge Interdiffusion and Its Impact on Heterostructure MOSFET Design and Process Integration 91
4.1 Interdiffusion for strained Si/relaxed SiGe structures 91
4.1.1 Summary of Extracted Interdiffusivity 91
4.1.2 Refining the Interdiffusivity Results 94
4.1.3 Interdiffusivity Modeling 99
4.1.4 Tensile Strain Characterization 102
4.1.5 Discussion on Tensile Strain Impact on Interdiffusion 107
4.2 Interdiffusion under Compressive Strain 108
4.2.1 Enhanced Interdiffusion under Compressive Strain 108
4.2.2 Compressive Strain Characterization 110
4.2.3 Extraction and Modeling of Interdiffusivity under Compressive Strain 111
4.2.4 Strain Coupling Factor and Its Origin 115
4.2.5 Error Analysis 119
4.2.6 On the Uniqueness of the Diffusivity Model for the Strain Effect 120
4.3 Discussions 122
4.3.1 Comparison with literature 122
4.3.2 Interdiffusion Mechanisms and the Impact of Strain 123
4.4 Surrounding Layer and Threading Dislocation Effects 124
4.4.1 Surrounding Layer Effect 124
4.4.2 Threading Dislocation Effect 126
4.5 Impact on Technology 128
4.5.1 Impact on HOI and Dual-channel MOSFET Design 129
4.5.2 Interdiffusion during RTA 132
4.5.3 Implant Damage Enhanced Interdiffusion 133
4.6 Summary of Chapter 4 136

CHAPTER 5 Summary and Future Work 139
5.1 Summary and Major Contributions of this Thesis 139
5.2 Suggestions for Future Work 141

Appendix A Example of Source Code for Electron Mobility Calculation. 147
Appendix B Fabrication Steps of Strained Si *n*-MOSFETs. 155
Appendix C Example of Source Code for MEDICI Simulations of C-V. 157
Appendix D Temperature profiles in furnace anneals 161
Appendix E Matlab code for Boltzmann-Matano Analysis 162
Appendix F The effect of initial condition of interdiffusion 166
Appendix G SIMS noise and Matano plane position 168
Appendix H Calculation of Thermal Mismatch Strain 172
Appendix I Ge dose conservation in TSUPREM-4 simulation 174
Appendix H TSUPREM-4 Source Code for Interdiffusion Simulation 176
Bibliography: 179

List of Figures

Figure 1-1 The number of papers published in SiGe and Ge area at IEDM since 1999 for various devices. 20
Figure 1-2 Cross section TEM image of an Intel 90 nm node p-MOSFET with SiGe source/drain. Figure courtesy of Dick James at Chipworks. [5]. 22
Figure 1-3 The epitaxial heterostructure of strained Si on a relaxed $Si_{1-x}Ge_x$ substrate... 24
Figure 1-4 The structure of a long channel surface strained Si *n*-MOSFET. 25
Figure 1-5 Structures of (a) heterostructure on insulator (HOI) and (b) heterostructure on bulk (also called "dual-channel") MOSFETs. 26
Figure 1-6 Effective electron mobility of unstrained Si MOSFETs in ref [19] (red lines) and strained Si MOSFETs in ref [7] (black lines) at 300 K and 77 K. 27
Figure 1-7 Measured (symbols) effective mobility enhancement ratios compared to calculations for the phonon-limited MOS mobility (solid line) for strained Si *n*-MOSFETs. From [23]. 29
Figure 1-8 Comparison of hole mobility ratios in strained Si and dual-channel *p*-MOSFETs as a function of vertical effective field, E_{eff}. Figure courtesy of I. Aberg. The citations for Lee, Leitz, Jung, Ghani, Rim and Takagi are references 10, 8, 9, 3, 25 and 19 respectively. 29
Figure 1-9 Conduction band energy splitting in strained Si. 30
Figure 2-1 Calculated kinetically limited critical thickness for strained $Si_{1-x}Ge_x$/Si at various growth temperatures from D. Houghton [31]. Metastable strained layers that are thicker than the critical thickness predicted by the Matthews and Blakeslee theory [29] can be achieved by low temperature epitaxial growth. 35
Figure 2-2 Comparison between the effective mobility data of Rim and Nayfeh for strained Si *n*-MOSFETs on $Si_{0.8}Ge_{0.2}$ substrate and unstrained control devices [7], [35]. 38
Figure 2-3 (a) Structure of strained Si *n*-MOSFETs after processing. (b) Energy band alignment for a surface strained Si *n*-MOSFET. 40
Figure 2-4 Damage profiles for Si implant doses $\phi 1$ to $\phi 4$, compared to those of boron implants (doses 7 x 10^{13} cm^{-2} and 5 x 10^{14} cm^{-2}, both implanted at 10 keV). The profiles were simulated by UT-MARLOWE. 100% percent amorphization is defined to correspond to an as-implanted interstitial concentration of 5 x 10^{21} cm^{-3}. The right axis shows the as-implanted interstitial concentration profile for these implant conditions. 43
Figure 2-5 Damage profiles of the Ge implant conditions $\phi 5$ and $\phi 6$, simulated by UT-MARLOWE. The right axis shows the as-implanted interstitial concentration profile for these implant conditions. 43
Figure 2-6 Split C-V measurements for a strained Si and a bulk *n*-MOSFET. 45
Figure 2-7 Total capacitances C_{tot} vs. V_{gate} for strained Si with (a) RTA1, 1000 °C for 1 sec, and (b) RTA2, 1000 °C for 10 sec. 47
Figure 2-8 (a) C_{tot} curves simulated by Medici with different thicknesses of the strained Si layer compared with the measured Ctot. The simulation with 100 Å strained Si layer matches the measured data better than that of 70 Å. (b) band

diagram of a strained Si MOSFET in the depletion regime. Holes are accumulated at the strained Si/ relaxed $Si_{0.8}Ge_{0.2}$ interface due to the band discontinuity. 48
Figure 2-9 The effective mobility vs. E_{eff} for strained Si n-MOSFETs with different implantation conditions in the channel, for (a) devices with RTA1, 1000 °C for 1 sec, and (b) devices with RTA2, 1000 °C for 1 sec. The measurements were made on 100 x 100 μm^2 devices. 50
Figure 2-10 Comparison of the effective mobility curves for strained Si MOSFETs with or without reoxidation. The implant conditions are ϕ1 and ϕ4, with same annealing step RTA1. 52
Figure 2-11 The effective mobility vs. E_{eff} for the CZ control devices with different implantation conditions for (a) devices with RTA1, and (b) devices with RTA2. The measurements were made on 100 x 100 μm^2 devices. 52
Figure 2-12 Effective mobility vs. vertical effective field E_{eff} for strained Si and CZ control devices with different RTAs. The doses are the lowest, 4 x 10^{12} cm^{-2} and the highest 5 x 10^{14} cm^{-2}. RTA1, 2, 3 are 1000°C for 1 sec, 1000°C for 10 sec and 950°C for 10 sec respectively. 54
Figure 2-13 Effective mobility at E_{eff}=0.7 MV/cm for strained Si and CZ control devices of different species, doses and RTA, for (a) devices with Si implant, (the equivalent boron dose is shown on the upper x axis), and (b) devices with Ge implants. 54
Figure 2-14 Cross section TEM micrographs for strained Si devices with RTA1 (1000 °C for 1 sec) and Si implants, for (a) devices with no implant, and (b) devices with Si implant φ4 (dose 5 x 10^{14} cm^{-2}). TEM courtesy of D. H. Anjum at the University of Virginia.. 56
Figure 2-15 Cross-section TEM micrographs for a strained Si device with RTA1 (1000 °C for 1 sec) and Si implant φ4 (dose 5 x 10^{14}). This is an image of higher magnification taken on the same sample as shown in Figure 2-14 (b). TEM courtesy of D. H. Anjum at University of Virginia. 57
Figure 2-16 Cross-section TEM micrographs for strained Si devices with RTA2 (1000 °C for 10 sec) and Si implants for (a) devices with Si implant φ2 (dose 2.7 x 10^{13} cm^{-2}), and (b) devices with Si implant φ4 (dose 5 x 10^{14}). TEM courtesy of D. H. Anjum at University of Virginia. 57
Figure 2-17 Cross-section TEM pictures for strained Si devices with RTA1 (1000 °C for 1 sec) and Ge implants for (a) devices with Ge implant φ5 (dose 3 x 10^{13} cm^{-2}), and (b) devices with Ge implant φ6 (dose 1 x 10^{15}). TEM courtesy of D. H. Anjum at University of Virginia. 58
Figure 2-18 SIMS profiles for Ge in strained Si MOSFETs for (a) RTA1 (1000 °C 1 sec), and (b) RTA2 (1000 °C 10 sec). 59
Figure 3-1 Hole mobility for different Si cap thickness for a Heterostructure in Insulator (HOI) MOSFET structure shown on the right (x0=0.24, y=0.46) for different rapid thermal annealing conditions. Figure courtesy of I. Aberg. 68
Figure 3-2 A TEM image illustrating inhomogeneous Si-Ge intermixing and interdiffusion at the polysilicon/Ge interface in the contact region of a Ge photodiode. TEM image courtesy of O. O. Olubuyide (MIT) and John Yasaitis (Analog Devices, Inc.). 69

Figure 3-3 A diffusion couple with an initial step profile for Boltzmann-Matano analysis. The red curve is the diffused profile... 72
Figure 3-4 Graphical illustration of the Matano plane z_M. The areas under the concentration curve on either side of z_M are equal. Figure from Ron Harrington's online course notes at Rensselaer Polytechnic Institute, Troy, NY.. 75
Figure 3-5 A generic "step" structure 76
Figure 3-6 (a) The Ge profile of a generic "peak and step" structure y/x_0. (b) A 45/45 "peak and step" epitaxial structure. The growth temperatures are in the parentheses. The term "valley" refers to the strained Si layer directly on top of the relaxed $Si_{1-x0}Ge_{x0}$ layer since it is surrounded by two SiGe layers. The term "shoulder" refers to the diffused "step". 77
Figure 3-7 Ge SIMS profiles of BM20 and BM40 structures before and after 920º C 60 min inert annealing. 79
Figure 3-8 Extracted interdiffusivity from the application of Boltzmann-Matano analysis to SIMS profiles for BM20 and BM40 structures. 79
Figure 3-9 Ge SIMS profiles and the generated foot part of the profile for 56/56 structure that illustrates the profile used in the pseudo-Boltzmann-Matano analysis... 81
Figure 3-10 SIMS profile with two generated profiles in the low-Ge-fraction region, for a sample annealed at 880º C for 30 min. 81
Figure 3-11 Interdiffusivity extracted from the three profiles shown in Figure 3-10....... 82
Figure 3-12 SIMS profiles for as-grown BM20, BM40 and BM60 structures. The leading edges and rounded shoulders are due to SIMS broadening effects. 83
Figure 3-13 (a) unprocessed extracted interdiffusivity from SIMS profiles of BM20 and BM40 structures in Figure 3-7, and (b) processed interdiffusivity with the low x_{Ge} data blocked for the BM40 structure. 84
Figure 3-14 Interdiffusivity for strained Si/relaxed SiGe structures extracted by Boltzmann-Matano analysis and pseudo-Boltzmann-Matano analysis. These data were extracted from samples with different step heights. Crosses are interdiffusivity data extracted from BM20 structures; diamonds are data extracted from 40-45% steps in BM40 and 45/45 structures; and circles are from 56% steps in BM56 and 56/56 structures. 89
Figure 4-1 Interdiffusivity for strained Si/relaxed SiGe structures extracted by Boltzmann-Matano analysis and pseudo-Boltzmann-Matano analysis. These data were extracted from samples with different x_0. (a) The interdiffusivity data for all samples. Data in low Ge fraction ($x_{Ge} < 0.2$) region for samples with $x_0 > 0.4$ not shown for clarity. (b) The interdiffusivity data for samples with $x_0 > 0.4$. (c) Interdiffusivity curves extracted from samples with different x_0 for 880 and 920 ºC. In the lower x_{Ge} range ($x_{Ge} < x_0 /2$), interdiffusivity shows dependence on x_0. In (b) and (c), the interdiffusivity extracted from the generated foot part of the profiles using pseudo-Boltzmann-Matano analysis is not shown.. 93
Figure 4-2 As-grown and annealed SIMS profiles for structure 56/56 and the TSUPREM-4 simulation using the interdiffusivity data in Figure 3-14 (b). 95
Figure 4-3 (a) As-grown and annealed SIMS profiles and the profile simulated by TSUPREM-4 that best fits the peak drop of structure 56/56 annealed at 800C

for 13 hours. The corresponding interdiffusivity expression used in TSUPREM-4 is $D = 4.2x10^{-20}\exp(8.1 * x_{Ge})$. (b) Post-annealed Ge profile of structure 45/45 simulated by TSUPREM-4 using the same expression in (a), together with the as-grown and annealed SIMS profiles. 98
Figure 4-4 Interdiffusivity curves extracted from Boltzmann-Matano analysis of shoulder profiles (symbols) compared to $D_{R/T}$ refined using Tsuprem-4 to fit the SIMS peak profiles (solid lines). 101
Figure 4-5 TSUPREM-4 simulations using $D_{R/T}$ model for BM20 structure annealed at 800C for 80 hours (symbols), on (a) linear, and (b) semilog, axes. The as-grown profile is an ideal step (dashed line), and the SIMS measurement is shown by the solid line. 102
Figure 4-6 SIMS profile of sample BM60E annealed at 880C for 90 min. 104
Figure 4-7 UV-Raman spectra (364 nm excitation) of the Si-Si longitudinal optical (LO) phonon for the strained Si layer in sample BM60I. Tensile strain is preserved after 880 ºC 90 min annealing. Raman data courtesy of Dr. Michael Canonico at Freescale Semiconductor, Inc. 104
Figure 4-8 As-grown and annealed Ge SIMS profiles of (a) structure 56/56 and (b) structure 56/31, both annealed at 800° C for 120 min. Significantly faster diffusion is observed in (b) than (a). 109
Figure 4-9 Raman spectra (442 nm excitation) of the Si-Si longitudinal optical (LO) phonon for structure 56/31 before (solid line) and after (dashed line) 800°C 120 min anneal, along with an unstrained Si reference sample. The arrows on top of this figure indicate the calculated Raman peak positions for SiGe layers fully strained to the relaxed $Si_{0.70}Ge_{0.30}$ substrates. 111
Figure 4-10 (a) SIMS profiles and the TSUPREM4 simulation that best fits the annealed peak of structure 56/31; (b) the interdiffusivities D_R and D_C that generate the best fit profile in (a). 112
Figure 4-11 Extracted interdiffusivity curves for structure 56/31 (solid lines) and 45/15 (crosses) at temperatures in the range of 770-840 ºC. 113
Figure 4-12 Temperature dependence of D(x_{Ge}=0.4) under different strain status and the corresponding activation energies. The lines are the best fit lines using least square method. 118
Figure 4-13 Interdiffusivity curves and error bars for structure 56/31. The solid line is the interdiffusivity curve $D_{bestfit}$ that fits SIMS peak profile in Figure 4-10. The dashed and dotted lines are the diffusivity curves which predict peak drops that are off by -2, -1, +1, and +2 at%. The corresponding diffusivity ratios relative to D_{bestfit} are 0.52, 0.73, 1.4 and 2.0. 119
Figure 4-14 Relative error in D extraction caused by SIMS errors assuming SIMS gives errors within ± 2 at% and ± 1 at%. The solid line is the interdiffusivity curve $D_{bestfit}$ that fits SIMS peak profile. 119
Figure 4-15 Extracted interdiffusivity curves to check the uniqueness of the model concerning the impact of strain on the diffusivity. Series (a) consists of structure 56/15 and 45/15. Series (b) consists of structure 56/31 and 45/31.122
Figure 4-16 Comparison between interdiffusivity from Aubertine et al's work [48] and that extracted using Boltzmann-Matano analysis in this work without TSUPREM-4 refinement, for Ge fraction < 0.2. 1222

Figure 4-17 As-grown and annealed Ge profiles measured by SIMS for (a) structure 56/31, (b) structure 56/17/31, (c) structure 56/32/31 and (d) structure 56/47/31. 126

Figure 4-18 Interdiffusivity curves that best fit the annealed profiles in Figure 4-17 (a) to (d). The lines are the interdiffusivity extracted for structure 56/31, i.e. the D_R-D_C model. 126

Figure 4-19 (a) The epitaxial structure of the 30/00 on defected substrate. (b) As-grown and annealed Ge profiles measured by SIMS for structure 30/00 grown on CZ substrate with less than 1 x 10^2 cm^{-2} dislocation density and on defected substrate with about 1 x 10^7 cm^{-2} dislocation density. 128

Figure 4-20 Hole mobility enhancement factor for dual-channel p-MOSFETs as a function of Ge fraction y in the hole channel layer and Ge fraction x_0 in the virtual substrate after possessing. Figure from [64]. 130

Figure 4-21 An example of dual-channel MOSFET structure design. The RTA is at 900 ºC for 10sec. (a) structure 70/30 (b) structure 70/50. Ge diffusion in (b) is much less than in (a). 131

Figure 4-22 Measured Ge SIMS profiles for a HOI structure annealed by RTA compared with the interdiffusion model simulation. SIMS data courtesy of I. Aberg. 132

Figure 4-23 Post-annealed SIMS data for a dual-channel MOSFET source/drain region with boron implant. The dual-channel MOSFET structure is a 60A strained Si/ $Si_{0.4}Ge_{0.6}$/ relaxed $Si_{0.7}Ge_{0.3}$. The dashed line is generated to emulate the as-grown Ge profile based on CV measurement and thickness calculation. The Ge dose (area under curve) is the same for both profiles. 135

Figure 4-24 TSUPREM-4 fitting curves to the post-annealed SIMS profile in Figure 4-23. (a) $f_{implant}$ = 3000 (b) $f_{implant}$ = 5000 (c) $f_{implant}$ = 1000. 136

List of Tables

Table 2-1 The ion implantation conditions used in this work. The percentage amorphization and the average project range (R_p) are from UT-MARLOWE simulation. The implantation conditions of Si ϕ1 and ϕ2 are chosen to match the damage profile of boron with doses 7 x 10^{13} cm^{-2} and 5 x 10^{14} cm^{-2} at 10keV. 41
Table 2-2 The experimental matrix used in this work. For wafers with Si implants, there is one implant condition on each half of the wafer, i. e., N | ϕ2 means the left half of wafer has no implant, while the right half of the wafer is implanted with condition ϕ2. RTA1, 2, 3 are the annealing conditions: 1000°C for 1 sec, 1000°C for 10 sec and 950°C for 10 sec respectively. 44
Table 3-1 Sample matrix for "step" structures annealed at different temperatures and times. Sample in bold letters are those with SIMS profiles available. 86
Table 3-2 Sample matrix for "peak and step" structures annealed at different temperatures and times. Sample in bold letters are those with SIMS profiles available....... 87
Table 3-3 Sample matrix for "peak and step" structures with 30% peak annealed at different temperatures and times. Sample in bold letters are those with SIMS profiles available. 88
Table 4-1 Sample details and the interdiffusivity expressions that fit the SIMS peak drops at 800, 840 and 880 ºC. 99
Table 4-2 Raman sample matrix in this work with sample structures and annealing conditions. 106
Table 4-3 The slopes of D_C against x_{Ge} (s_C) on a semilog scale used in Tsuprem-4 that best fits the SIMS peak drops, and Q'_{inter} calculated based on s_C. 114
Table 4-4 Ge peak heights before and after 840C 30min anneals for structures in series (A) and (B). 121
Table 5-1 Summary of the biaxial strain coupling factor Q' and x_{Ge} dependence for SiGe interdiffusion under biaxial stress. 145

CHAPTER 1 Introduction

Semiconductor devices have been the basis for the electronics industry for several decades, and the silicon metal oxide semiconductor field effect transistor (Si MOSFET) is the most important of such devices. The continued scaling and the performance improvement of Si CMOS are behind the advancement of many electronic products, such as computers, cell phones, etc. However, physical limitations and processing difficulties are making MOSFET scaling more difficult. Many "technology boosters" have been proposed to extract more performance from scaled CMOS, such as the use of high-k gate dielectric materials, metal gate, multi-gate design, vertical structure, and ultra-thin body silicon-on-insulator (SOI). Another option to enhance the performance of CMOS is to use high mobility channel materials such as strained Si, SiGe, Ge and compound semiconductors. Strained Si is the first high mobility channel material that is widely used in industry. SiGe and Ge channel materials offer the potential for even higher mobility, and are now actively being researched for the next generation of enhanced mobility MOSFETs.

Apart from applications in MOSFETs, the SiGe and Ge-on-Si platforms are also attractive for use in a wide variety of electronic and optoelectronic devices. The most important example is the SiGe heterojunction bipolar transistor (HBT) for telecommunications, where SiGe is used to increase the operation frequency. Other examples are in the area of Si based microphotonics, where SiGe and Ge are utilized to build photodetectors and modulators for high speed telecommunications and on-chip interconnects. Low concentration SiGe ($< 10\%$) is also used in solar cells to expand the

absorption spectrum of sunlight to achieve higher efficiency. Figure 1-1 below shows the number of SiGe papers published in one of the largest electronic device conferences, the International Electron Devices Meeting (IEDM), since 1999. For each IEDM, there are about 250 to 300 papers. There is a clear trend of increasing research effort in SiGe and Ge devices, especially in MOS applications.

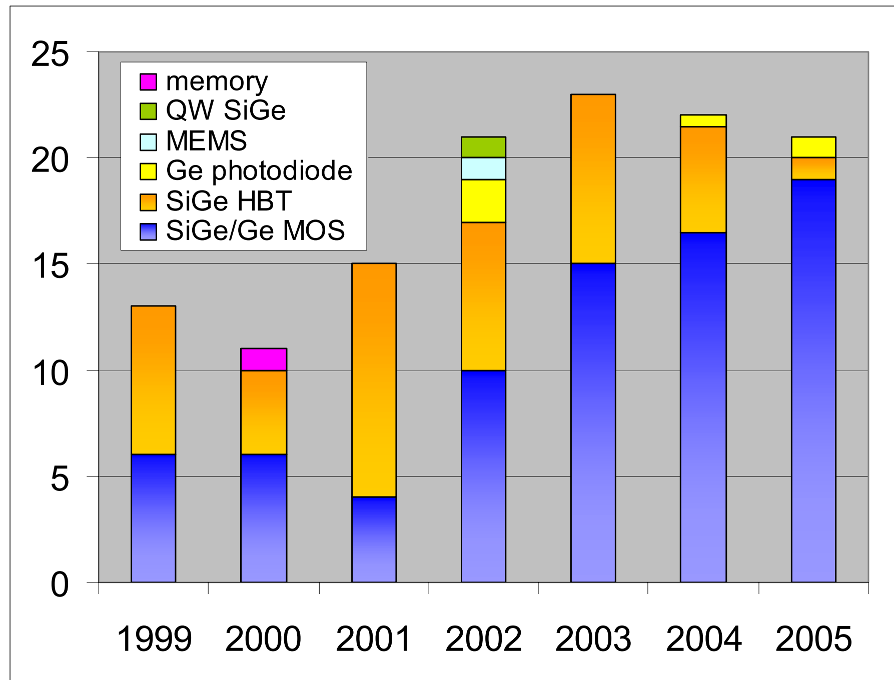

Figure 1-1 The number of papers published in SiGe and Ge area at IEDM since 1999 for various devices.

The advantages of using SiGe and Ge are multifold. First, as discussed above, SiGe and Ge have higher carrier mobility than Si, which provides a way to boost MOSFET performance. Secondly, Ge is highly compatible with Si compared with all other semiconductors. As a close relative to Si in the periodic table, Ge is completely miscible with Si, and Ge in the Si lattice is neutral. Ge has the same diamond lattice structure as Si with a 4.2% larger lattice constant at 300 K, and can be epitaxially grown on top of Si. Ge has an indirect bandgap of 0.66 eV at 300 K. These properties provide extra freedom

for strain and bandgap engineering in SiGe devices for electronic and optical applications. The last and the most important advantage is that Ge can be integrated using Si fabrication equipment with relatively few process modifications, which makes SiGe technology economically favorable compared with other high mobility materials, such as those in the III-V family.

However, using SiGe and Ge in Si structures does bring some challenges to process integration. Critical challenges include high quality epitaxial growth, Si-Ge interdiffusion during thermal processing and implant damage annealing. In this work, the primary focus is on the issue of Si-Ge interdiffusion including its impact on carrier mobility, interdiffusivity extraction and modeling and simulation.

1.1 Strained Si and SiGe CMOS Technology

1.1.1 Process-induced Strain and Global Strain by Epitaxy

To date, two different approaches are being used to introduce strain in Si MOSFET channels to improve transport properties. The first method, which is already to be implemented in manufacturing, uses process-induced strain, where strain is introduced on a local scale by fabrication steps. In these techniques, uniaxial strain is most commonly used. The stressors include high stress nitride liners [1, 2], embedded SiGe source and drain (e-SiGe) [3] as shown in Figure 1-1, shallow trench isolation (STI) [4] and stress memorization. The process-induced strain is now widely used in industry, and is the major performance booster in 90 nm node and beyond. The advantages of this method are its relatively low-cost, low defect density and the use of uniaxial strain, which provides more performance improvement for p-MOSFETs than biaxial strain. One character for process-induced strain is that it depends on device geometry, which makes it work better

for scaled devices, but at the same time adds complexity to process optimization and circuit design.

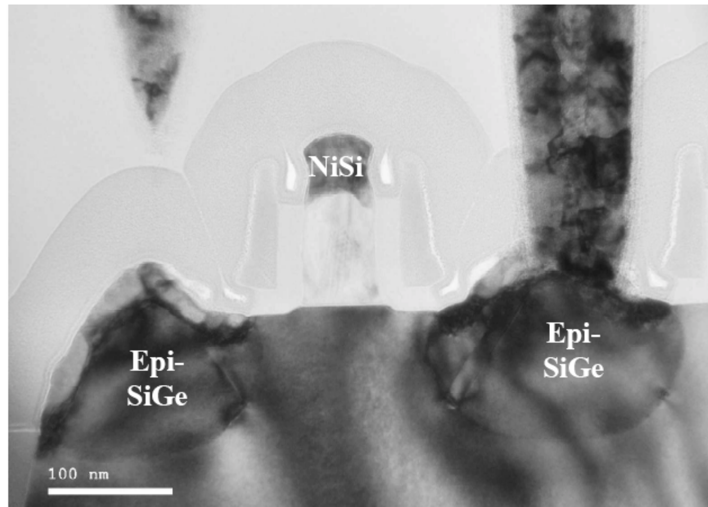

Figure 1-2 Cross section TEM image of an Intel 90 nm node p-MOSFET with SiGe source/drain. Figure courtesy of Dick James at Chipworks. [5].

The second approach is to introduce global biaxial strain by epitaxial growth of lattice mismatched layers such as strained Si on top of relaxed SiGe virtual substrate. This method was used in the discovery and early research on strain engineering for CMOS applications. Although this method has the disadvantage of higher dislocation density and higher cost, it has several advantages which are especially suitable for some types of applications and for research. One advantage is that global strain doesn't depend on device geometry, so a large amount of strain with well-known magnitude and character can be introduced in the channel. This makes it much easier to clarify the dependence of device performance on strain. Another advantage is that epitaxy allows bandgap engineering for carrier confinement. Epitaxial structures are also better for the study of strain, bandgap, and integration issues, as the strain and material properties of epitaxial structures are uniform in plane, and easier to model than three dimensional (3D)

process-induced strain. Finally, epitaxially grown heterostructures can be used to introduce new channel materials such as SiGe and Ge, which offer larger mobility enhancements than can be obtained with strain in Si alone. Based on these considerations and available facilities, epitaxial grown heterostructures are used in this work to study process integration issues of strained Si and SiGe.

In terms of mobility for these two methods, Uchida et al. compared the biaxial and uniaxial strain effects on carrier mobility in bulk and ultra-thin body (UTB) MOSFETs using externally applied mechanical stress [6]. This work demonstrated that in bulk n-MOSFETs, electron mobility enhancement is stronger in the order of biaxial tensile, <l00> uniaxial tensile, and <l10> uniaxial tensile strains, and that in bulk p-MOSFETs, hole mobility enhancement is stronger in the order of <110> uniaxial compressive, <l00> uniaxial compressive, and biaxial tensile strains. It is also demonstrated that uniaxial strain is effective to enhance both electron and hole mobility in UTB MOSFETs with Si thickness down to at least 2.5 nm and that biaxial tensile strain is also effective to enhance electron mobility in UTB MOSFETs with thickness of Si layer less than 5 nm. It was shown that subband structure engineering in UTB MOSFETs can cooperate with strain engineering to further enhance mobility.

Due to reasons stated above, this thesis work focuses on epitaxial heterostructures with biaxial strain, which are introduced in the next section.

1.1.2 Heterostructure Based Enhanced Mobility MOSFETs

Biaxial tensile strain is shown to enhance electron mobility up to 1.8X for n-MOS [7], while biaxial compressive strain together with high Ge concentration in the channel is shown to enhance hole mobility by up to 10X [8, 9, 10]. Various structures are

proposed for high mobility channel MOSFETs, examples of which are surface-channel strained Si MOSFETs, strained Si directly on insulator (SSDOI) [11], dual-channel, heterostructure on insulator (HOI) [12] and SiGe-on-insulator (SGOI) MOSFETs [13,14]. All of these are based on the epitaxial (epi) growth of $Si_{1-x}Ge_x$/strained Si heterostructures. In order to understand the epitaxial growth, a strained Si MOSFET, which is the structure used in the study of ion implantation and thermal processing impacts on mobility enhancement as discussed in Chapter 2, is taken as an example.

A relaxed $Si_{1-x}Ge_x$ layer is used as the virtual substrate of the strained Si MOSFET. The lattice constant of pure Ge is larger than that of Si by 4.2%. Thus, the $Si_{1-x}Ge_x$ virtual substrate has a larger lattice constant than the equilibrium lattice constant of Si. When a thin Si layer is epitaxially grown on a relaxed $Si_{1-x}Ge_x$ layer, the lattice of Si accommodates the larger lattice of the $Si_{1-x}Ge_x$ below. Therefore, tensile stain is introduced into the Si channel. Figure 1-3 shows the epitaxial heterostructure of strained Si on a relaxed $Si_{1-x}Ge_x$ substrate.

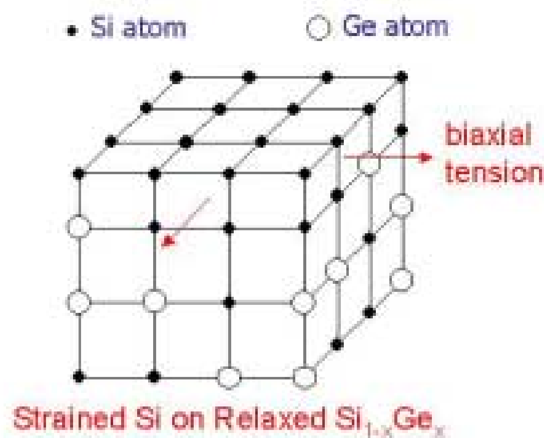

Figure 1-3 The epitaxial heterostructure of strained Si on a relaxed $Si_{1-x}Ge_x$ substrate.

Figure 1-4 shows the structure of a long channel surface strained Si *n*-MOSFET on top relaxed $Si_{0.8}Ge_{0.2}$ virtual substrate. The relaxed $Si_{0.8}Ge_{0.2}$ layer is epitaxially grown on a graded relaxed $Si_{1-x}Ge_x$ buffer layer, which is capped by a strained Si layer. The graded $Si_{1-x}Ge_x$ buffer layer is formed by increasing the Ge content from 0% to 20% over a thickness of 2 μm. The graded buffer layer is used to reduce the threading dislocation density in the relaxed $Si_{0.8}Ge_{0.2}$ cap and the strained Si channel. Utilizing the graded buffer technology, the threading dislocation density in the relaxed $Si_{0.8}Ge_{0.2}$ layer can be reduced to 10^5 cm^{-2}, which is sufficient for the operation of Si MOSFETs [15]. Without the buffer layer, the relaxed $Si1_{0.8}Ge_{0.2}$ layer would have a very high threading dislocation density, on the order of 10^9~10^{10} cm^{-2}.

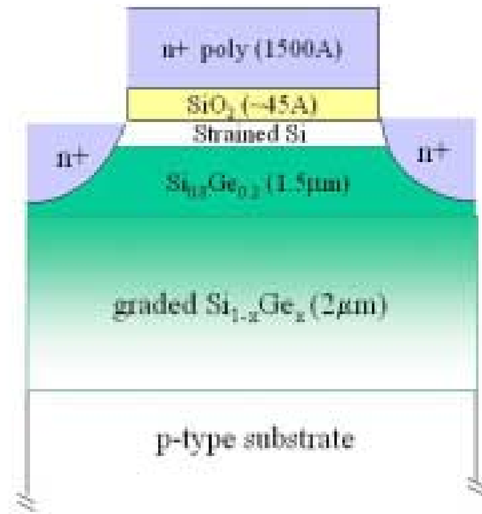

Figure 1-4 The structure of a long channel surface strained Si *n*-MOSFET.

In the past few years, in order to obtain higher hole mobility enhancement and scalability, more structures have been proposed using compressive, Ge-rich SiGe and/or on-insulator structures. Heterostructure on insulator (HOI) structures have been proposed

by Aberg et al. HOI uses strained Si layer as the electron channel and compressively stained SiGe as the hole channel (see Figure 1-5 (a)). The entire heterostructure is about 100 A thick and is on insulator for scalability. The structure that holds the record high hole mobility enhancement is a bulk dual-channel MOSFET with Ge fraction y = 1.0 and $x_0 = 0.5$ [10] as shown in Figure 1-5 (b).

One major process integration issue for these high Ge structures is that Si-Ge interdiffusion at Si/SiGe or Si/Ge interfaces causes mobility degradation due to loss of bandgap confinement, higher alloy scattering and poor interface quality due to interdiffusion. The interdiffusion can also be a problem for next generations of nanometer scale MOSFETs using embedded S/D (shown in Figure 1-2), where higher Ge fraction SiGe is used in the S/D regions at shorter channel length. Si-Ge interdiffusion behavior and modeling is the major focus of this thesis, which is addressed in Chapter 3 and 4.

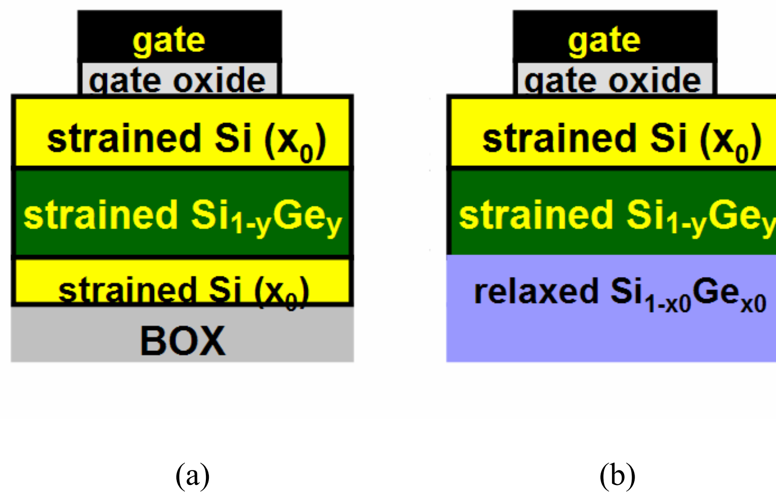

(a) (b)

Figure 1-5 Structures of (a) heterostructure on insulator (HOI) and (b) heterostructure on bulk (also called “dual-channel”) MOSFETs.

1.1.3 Mobility Enhancement

The main advantage of strained Si and SiGe MOSFETs is the enhancement in the carrier mobility and thus the current drive over unstrained Si MOSFETs. J. Welser first reported 1.8X electron mobility enhancement in strained Si *n*-MOSFETs [16, 17]. K. Rim *et al.* reported a 1.8X enhancement in hole mobility in strained Si *p*-MOSFETs on $Si_{0.71}Ge_{0.29}$ substrates over those on $Si_{0.90}Ge_{0.10}$ substrates [18]. A 75% enhancement in electron mobility over the universal mobility of unstrained Si *n*-MOSFETs and an increased transconductance were seen in deep submicron in strained Si *n*-MOSFETs [7]. Several research groups have obtained similar enhancement factors for electron mobility. Figure 1-6 shows the electron mobility of a strained Si MOSFET fabricated by K. Rim *et al* and the universal mobility of an unstrained Si MOSFET by Takagi *et al.* at room temperature and 77 K [7,19]. Electron mobility is enhanced over the temperature range from 77 to 300 K.

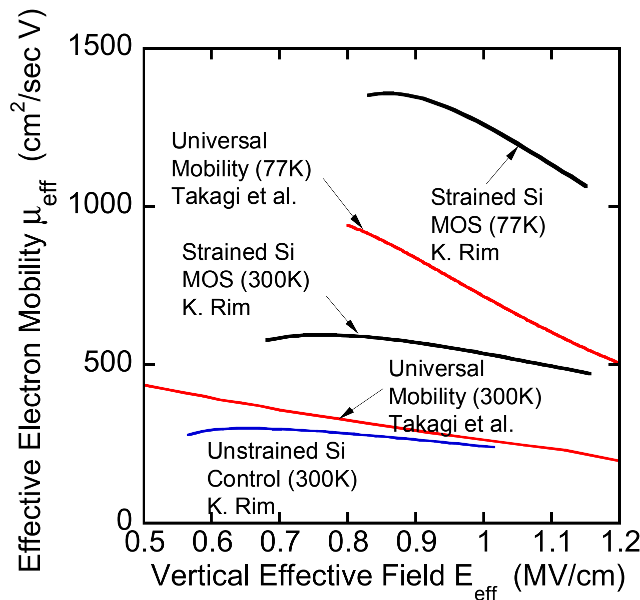

Figure 1-6 Effective electron mobility of unstrained Si MOSFETs in ref [19] (red lines) and strained Si MOSFETs in ref [7] (black lines) at 300 K and 77 K.

Figure 1-7 shows the electron mobility enhancement factors vs. Ge fraction in biaxial strained Si MOSFETs measured by different research groups [20,21,22,23]. At room temperature and in the normal MOSFET operating E_{eff} range, electron mobility is dominated by phonon scattering. Peak electron mobility enhancements measured in uniformly doped devices saturate near a mobility enhancement factor of 1.8 for strained Si with substrate Ge content above 20%. This agrees with calculations of the impact of strain on the phonon-limited MOS electron mobility [24].

While biaxial strained Si *n*-MOSFETs display electron mobility enhancements over a wide E_{eff} range, the hole mobility in biaxial strained Si *p*-MOSFETs is improved primarily at low E_{eff} (< 1 MV/cm). The enhancement ratio r approaches 1 at $E_{eff} \sim 1$ MV/cm for *p*-MOSFETs with substrate Ge fractions below 30%, as shown by Rim's data [25] in Figure 1-8. A better approach to achieve higher hole mobility is to use uniaxial strain (as shown in Figure 1-2), or higher Ge fraction under compressive strain in dual-channel structures (as shown by the data of Lee [10], Leitz [8], and Jung [9] in Figure 1-8). The record high hole enhancement factor was obtained by M. L. Lee, et al. from 4 nm strained Si/ 12 nm compressive Ge on relaxed $Si_{0.5}Ge_{0.5}$ [10], as seen in Figure 1-8.

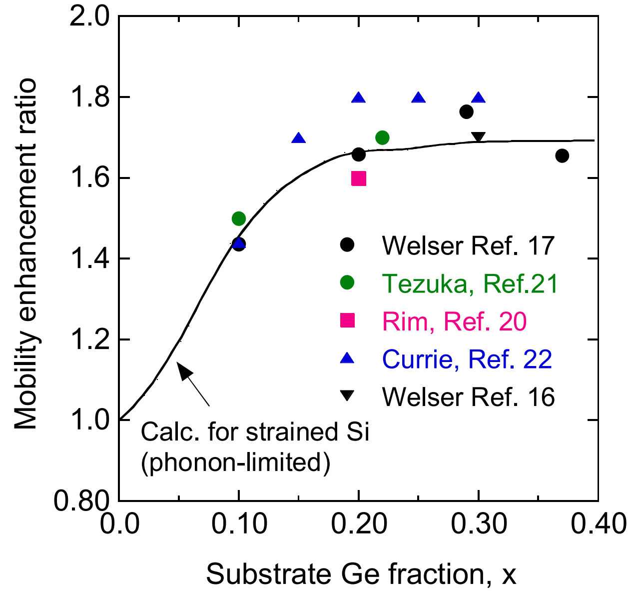

Figure 1-7 Measured (symbols) effective mobility enhancement ratios compared to calculations for the phonon-limited MOS mobility (solid line) for strained Si *n*-MOSFETs. From [23].

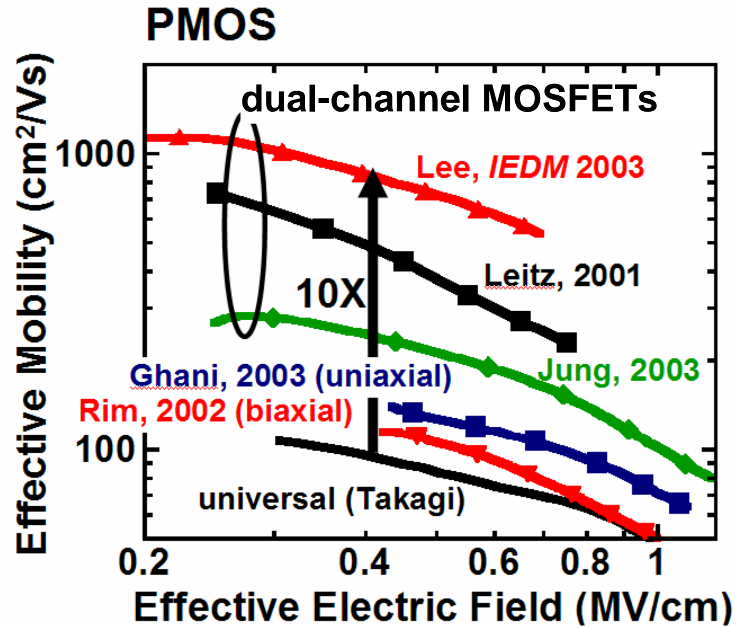

Figure 1-8 Comparison of hole mobility ratios in strained Si and dual-channel *p*-MOSFETs as a function of vertical effective field, E_{eff}. Figure courtesy of I. Aberg. The citations for Lee, Leitz, Jung, Ghani, Rim and Takagi are references 10, 8, 9, 3, 25 and 19 respectively.

Theoretical study shows that biaxial tensile strain in the Si layers grown on relaxed $Si_{1-x}Ge_x$ splits the 6-fold degeneracy in the Si conduction band [26, 27] as shown

in Figure 1-9. The 2-fold degenerate valleys with smaller in-plane mass Δ_2 are preferentially populated. Intervalley phonon scattering and the effective mass of electrons for in-plane transport are reduced, which improves the electron mobility at low and intermediate E_{eff}. At high E_{eff}, however, there are controversies about why the electron mobility is enhanced by strain, since the electron confinement by the inversion-potential at the SiO_2-Si interface lifts the 6-fold degeneracy by an amount similar in magnitude to the strain effect [28].

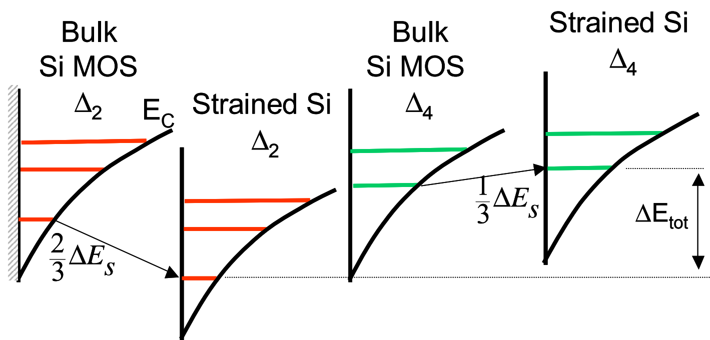

Figure 1-9 Conduction band energy splitting in strained Si.

1.2 Direction and Organization of Thesis

As enhancing the mobility has become an important technology booster for 90 nm node and beyond, it is important to understand the impact of processing factors such as ion implantation and thermal annealing on the mobility enhancement. Si-Ge interdiffusion during thermal processing is one of the major integration issues for SiGe high mobility devices, which is still not well understood. The motivation of this thesis is

to address these issues by investigating the process integration and process physics of ion implantation and Si-Ge interdiffusion in enhanced mobility MOSFETs.

The first part of this work demonstrated that Si-Ge interdiffusion and ion implantation damage during the fabrication of strained Si n-MOSFETs have significant impact on electron mobility and thus device performance, which is discussed in Chapter 2. The second part of this work, which is also the major part, was a systematic investigation of the Si-Ge interdiffusion behavior in epitaxial strained Si/$Si_{1-y}Ge_y$/strained Si/relaxed $Si_{1-x}Ge_x$ and strained Si/relaxed $Si_{1-x}Ge_x$ heterostructures for Ge fractions between 0 and 0.56 over the temperature range of 770 – 920 ºC. An analytical model for interdiffusion simulation is established based on experiments. The interdiffusion study is discussed in Chapter 3 and Chapter 4 in detail. Chapter 5 provides a summary and suggestions for future work.

1.3 Chapter Summary

In this chapter, strained Si, SiGe and Ge enhanced mobility MOSFETs were introduced. Process-introduced strain and global strain by epitaxy were discussed, followed by the description of various heterostructures for enhanced mobility MOSFETs and the Si-Ge interdiffusion issue in the fabrication of these devices. Mobility enhancement from these structures was then discussed. Finally, the motivation and organization of this thesis was presented.

CHAPTER 2 Impact of Thermal Processing and Ion Implantation on the Mobility Enhancement in Strained Si *n*-MOSFETs

In strained Si MOSFETs, strained Si layers are epitaxially grown on relaxed SiGe virtual substrates. In terms of material properties such as defect density and thermal and mechanical compatibility, relaxed SiGe virtual substrates are not as good as bulk Si substrates. The heterostructures are generally more susceptible to thermal processing because the strained Si layer may begin to relax to its equilibrium state during thermal processing, if the thickness is above the critical thickness [29]. Some processing steps such as thermal processing, ion implantation and reactive ion etching (RIE) play important roles in strain relaxation. The latter two steps can introduce defects into the substrates which can degrade the carrier mobility [30]. Ion implantation may also assist strain relaxation by introducing ion implantation damage into the lattice. These effects will result in the loss of mobility enhancement. Therefore, understanding the influence of processing steps on the mobility is important for SiGe technology.

In this chapter, a study of the impact of thermal processing and ion implantation on mobility enhancement in strained Si n-MOSFETs is presented. Section 2.1 contains an introduction to Si/SiGe processing. Section 2.2 describes the experimental design and device fabrication performed in this work. Section 2.3 discusses the electrical characteristics and Medici simulations. Section 2.4 describes the mobility characterization and mobility dependence on processing conditions. Section 2.5 discusses the materials analysis and the mechanisms of mobility degradation during

processing. Section 2.6 presents the impact on technology and Section 2.7 summarizes this chapter.

2.1 Introduction to the Processing of Si/SiGe

2.1.1 Critical Thickness and Strain Relaxation in Strained Si/$Si_{1-x}Ge_x$

When a thin crystalline film is grown on a crystalline substrate with a different equilibrium lattice constant, strain is introduced into the thin film. As long as the film is thin enough, it will adopt the in-plane lattice constant of the substrate. The strain can be released by breaking some of the deformed bonds, creating dislocations in the crystal structure of the film. For this to happen, the film needs to be thicker than the critical thickness t_{crit}, above which it is energetically favorable for dislocations to be present in the film [29]. In theory, a film with thickness less than t_{crit} can be subjected to unlimited thermal exposure without any relaxation of the strain by misfit dislocation formation. The interdiffusion of the components of the alloy (Si and Ge) can also lead to strain relaxation by a change in composition of the structure, which will be addressed in Chapters 3 and 4. The concept of the critical thickness is important for device fabrication, in which devices are exposed to thermal processing often at high temperatures. Maintaining the strain is the key to obtaining the performance improvement in strained Si MOSFETs.

Houghton studied the critical thickness of strained $Si_{1-x}Ge_x$ on unstrained Si, which is a good starting point for estimating the critical thickness of strained Si on unstrained $Si_{1-x}Ge_x$ [31]. Figure 2-1 shows the calculated kinetically limited critical thickness for

strained $Si_{1-x}Ge_x/Si$ at various temperatures and Ge fractions. For example, the equilibrium critical thickness for strained $Si_{0.8}Ge_{0.2}/Si$ is about 120 Å.

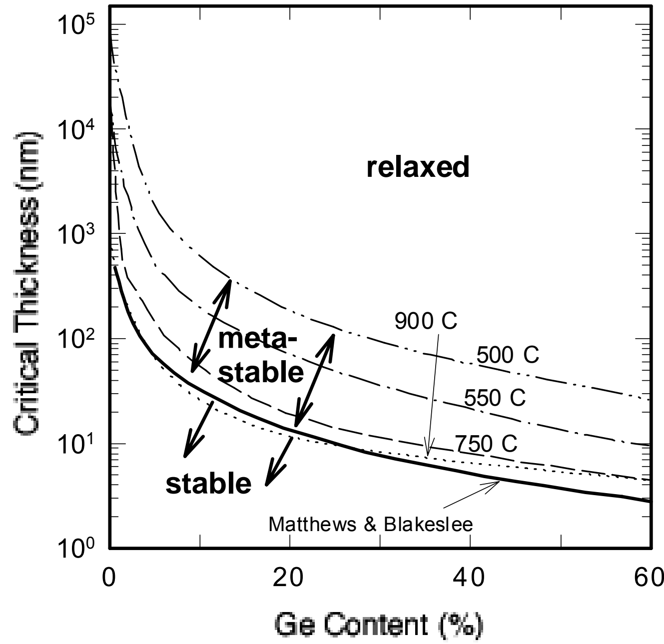

Figure 2-1 Calculated kinetically limited critical thickness for strained $Si_{1-x}Ge_x/Si$ at various growth temperatures from D. Houghton [31]. Metastable strained layers that are thicker than the critical thickness predicted by the Matthews and Blakeslee theory [29] can be achieved by low temperature epitaxial growth.

Samavedam *et al.* used the Matthews-Blakeslee (MB) energy minimization criterion [29] to calculate the strained Si critical thickness as a function of Ge fraction in the underlying uniform relaxed SiGe layer [32]. The calculated t_{crit} was found to be about 205 Å for a strained Si layer on $Si_{0.8}Ge_{0.2}$. In the experiments performed in that work, etch pit density (EPD) measurements were used to characterize the misfit dislocation density. Misfit dislocations were present for Si cap thicknesses above 110 Å which were grown at 700 °C on a $Si_{0.8}Ge_{0.2}$ substrate with a threading dislocation density of 10^5~10^6/cm^2. The $Si_{0.8}Ge_{0.2}$ substrates used in this work have comparable dislocation density. Currie *et al.* studied the channel thickness dependence of electron mobility in

strained Si MOSFETs on $Si_{0.8}Ge_{0.2}$ virtual substrate with a threading dislocation density of ~10^5/cm^2, and found that strained Si layers thinner than 120 Å are fully strained [22]. Therefore, the critical thickness of the strained Si/$Si_{0.8}Ge_{0.2}$ in this work is estimated to be about 110~120 Å.

When the thickness of a strained Si layer is above t_{crit}, the effective stress makes it favorable for misfit dislocations to be present in the crystal structure. It is necessary to overcome an initial energy to nucleate a dislocation. Thermal processing can provide energy for dislocations to nucleate and later propagate. Particles and defects at a heterointerface can act as dislocation nucleation centers. Each dislocation line relieves a certain amount of strain proportional to the length of the misfit dislocation segment. The density of misfit dislocations can be measured by selective etching of the strained Si surface. The presence of misfit dislocations indicates the strained Si is not fully strained.

2.1.2 Strain Relaxation and Thermal Stability of Strained $Si_{1-x}Ge_x$/Si

Strained $Si_{1-x}Ge_x$ on relaxed Si substrates has been extensively studied due to its importance in many device structures such as the heterojunction bipolar transistor. The strained $Si_{1-x}Ge_x$/Si system is discussed here as it is a good analogy to the strained Si/$Si_{1-x}Ge_x$ system. It provides a useful reference since the latter system is not as fully studied. Thermal stability and strain relaxation in the strained Si layer are problems in the processing of strained Si, since the mobility enhancement depends on the strain in the Si layer and its stability. Two problems in the strained $Si_{1-x}Ge_x$ /Si system are discussed first.

The thermal stability of $Si_{1-x}Ge_x$ films has been studied by Houghton *et al.* [31] and Matthews and Blakeslee [29] as previously mentioned (see Figure 2-1). There has been some study of ion implantation effects and relaxation in the strained $Si_{1-x}Ge_x$/Si system. Hull *et al.* found significantly enhanced strain relaxation during annealing of Si/strained $Si_{1-x}Ge_x$/Si heterostructures via point-defects introduced by ion implantation of boron and arsenic [33]. This enhanced strain relaxation is the result of the increased nucleation sites introduced by ion implantation. Misar *et al.* studied the annealing of Si/strained $Si_{1-x}Ge_x$/Si after phosphorus implantation and suggested that the permanent dislocation loops resulting from the implantation cause strain relaxation [30]. Hollander *et al.*, using H+ and He+ implants into $Si_{1-x}Ge_x$/Si(100) heterostructures, showed implanted samples to have much denser, irregular misfit dislocations than unimplanted samples, causing the $Si_{1-x}Ge_x$ to relax [34].

2.1.3 Background on Processing Influence on Mobility Enhancement in Strained Si

Currie *et al.* have studied the effects of strain, well implantation, thermal budget and channel thickness on the mobility of strained Si MOSFETs [22]. In that work, 13 keV boron and 45 keV phosphorous were implanted into the Strained $Si/Si_{0.7}Ge_{0.3}$ heterostructure to a dose of $1x10^{12}$ cm^{-2} prior to MOSFET processing. It should be noted that this is a relatively low implant dose. After a 1000 °C 1 sec rapid thermal anneal (RTA), the measured mobility enhancement was the same for implanted and unimplanted devices. These results are consistent with the results of this work, in which an implantation dose as low as $1x10^{12}$ cm^{-2} has no effect on the mobility enhancement (see details in section 2.4).

Currie's study on the thermal budget effect was conducted on NMOS and PMOS on strained Si/$Si_{0.7}Ge_{0.3}$ heterostructures without ion implantation. The RTAs were performed at 1000 °C and 950 °C for times ranging from 1 to 30 sec. The results indicate that the mobility enhancement factor for strained Si n-MOSFETs is reduced from 1.7 to 1.2X for an RTA of 1000 °C for 30 sec.

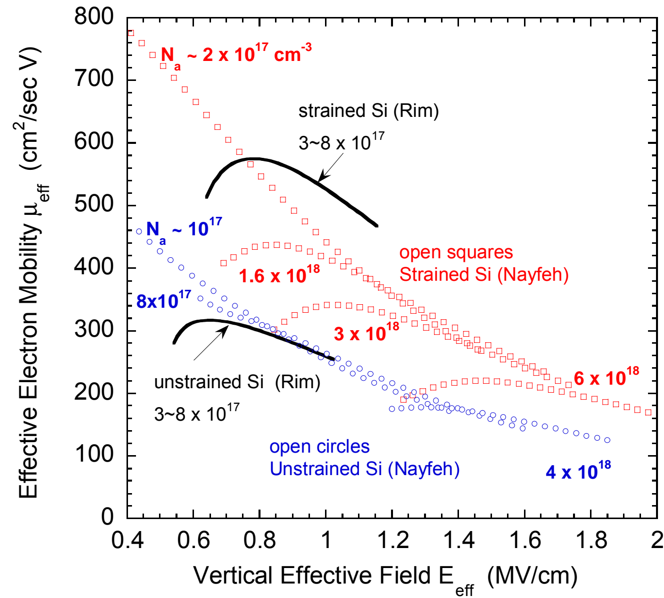

Figure 2-2 Comparison between the effective mobility data of Rim and Nayfeh for strained Si *n*-MOSFETs on $Si_{0.8}Ge_{0.2}$ substrate and unstrained control devices [7], [35].

Experimental work published so far has given some evidence of the potential influence of processing on the mobility in the strained Si MOSFETs using conventional fabrication processes. Different enhancement factors have been reported by Rim *et al.* and Nayfeh *et al.* for strained *n*-MOSFETs on $Si_{0.8}Ge_{0.2}$ substrate [7,35]. Figure 2-2 shows that at E_{eff} =1 MV/cm, the mobility of Rim's strained Si devices is higher than Nayfeh's by 20%. There are some differences between these two process flows. One is the thermal budget. In Rim's study, the gate oxide was grown at 800 °C and source/drain implant annealing was 2 min at 650 °C and 15 sec at 850 °C. In Nayfeh's process flow,

gate oxide was grown at 800 °C and RTA was performed at 1000 °C for 1 sec. Another difference is that Rim's devices were *in-situ* doped while Nayfeh's were doped by ion implantation. It is possible that the higher thermal budget and ion implantation damage introduced some mobility degradation in Nayfeh's devices.

Even in the same process, Nayfeh *et al.* showed that the strained Si *n*-MOSFETs with highest boron implantation dose 7 x 10^{13} cm^{-2} (equivalent doping 6 x 10^{18} cm^{-3}) have lower electron mobility enhancement than devices with low doses [37]. There are two possible reasons for this mobility degradation. One is related to defect formation and strain relaxation due to implantation-induced lattice damage; the other is higher Coulomb scattering due to higher dopant concentration. To investigate the impact of implantation-induced damage on mobility, a long channel strained/bulk Si *n*-MOSFET process was designed in this work. Neutral Si and Ge were implanted into the channel to introduce damage. The channel doping was kept unchanged assuming channel dopant diffusion is not significantly changed by the ion implantation. Therefore, the mobility degradation due to ion implant damage is separated from the degradation due to ionized impurity Coulomb scattering effects. UT-MARLOWE simulation was used to model the damage profiles of Si, B and Ge in order to choose the implantation energies and doses to closely match the damage profiles.

2.2 Experiment Design and Fabrication

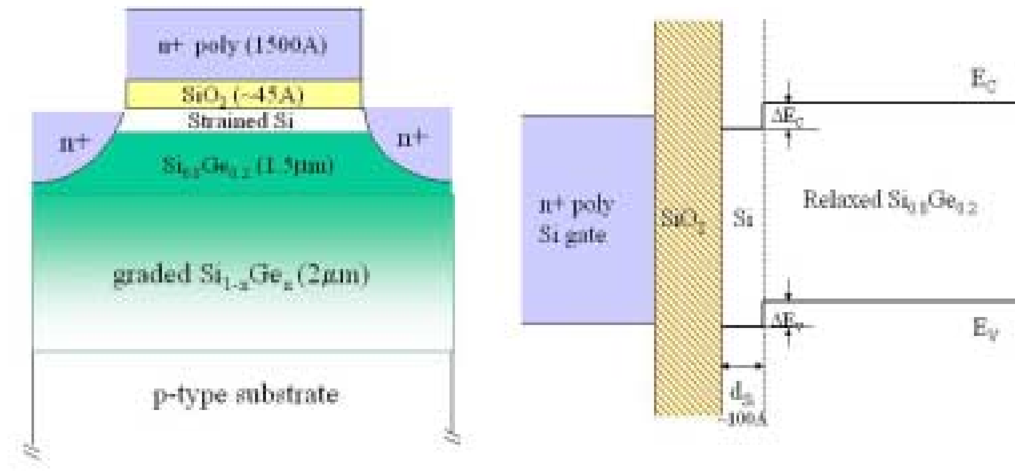

Figure 2-3 (a) Structure of strained Si *n*-MOSFETs after processing. (b) Energy band alignment for a surface strained Si *n*-MOSFET.

The structure of the strained-Si *n*-MOSFETs after fabrication is illustrated in Figure 2-3 (a). Relaxed $Si_{0.8}Ge_{0.2}$ layers were epitaxially grown by Lee on a graded relaxed $Si_{1-x}Ge_x$ buffer layer in a UHVCVD reactor. The graded $Si_{1-x}Ge_x$ buffer layer was formed by increasing the Ge content from 0 to 20% over a thickness of 2 μm. The strained Si layer was epitaxially grown on the relaxed $Si_{0.8}Ge_{0.2}$ layer. The as-grown thickness of the strained Si layer was 18 nm. Some strained Si was consumed during the gate oxidation and surface cleaning processes. From the CV measurement and simulation, the remaining strained Si layer thickness is estimated to be 100 Å. Figure 2-3 (b) shows the energy band alignment of the strained Si MOSFET structure. The conduction band and valence band in strained Si are both lower than that of relaxed $Si_{1-x}Ge_x$. The offsets ΔE_C and ΔE_V depend on the Ge fraction. In the case of $Si_{0.8}Ge_{0.2}$, both offsets are about 125 meV.

The strained Si layer and the $Si_{0.8}Ge_{0.2}$ layer were *in-situ* doped with boron in the UHVCVD reactor. The doping level is 2.5~3 x 10^{17} cm^{-3}. The CZ control wafers were boron doped 1 x $10^{17}cm^{-3}$ p-type wafers. This doping difference between strained Si and CZ control devices offsets the threshold voltage (V_{th}) difference introduced by the energy band splitting of strained Si. Therefore, the measured V_{th} of the strained Si devices matches that of the CZ control devices.

Implant Conditions	Implant Species	Dose (cm^{-2})	Energy (keV)	Simulated Percentage Amorphization	Simulated R_P (Å)	Comments
ϕ1	Si	4 x 10^{12}	39	2.5%	160	Match the Damage of B 7 x 10^{13} cm^{-2} 10keV
ϕ2	Si	2.7 x 10^{13}	39	16%	240	Match the Damage of B 5 x 10^{14} cm^{-2} 10keV
ϕ3	Si	1 x 10^{14}	35	54%	170~280	Sub Amorphous B 2 x 10^{15} cm^{-2} 10keV
ϕ4	Si	5 x 10^{14}	30	100%	200	Amorphous B 5 x 10^{15} cm^{-2} 10keV
ϕ5	Ge	3 x 10^{13}	30	60%	100	Match the Damage of Si ϕ3
ϕ6	Ge	1 x 10^{15}	30	100%	200	Typical Dose for Deep Source/Drain As Implant

Table 2-1 The ion implantation conditions used in this work. The percentage amorphization and the average project range (R_p) are from UT-MARLOWE simulation. The implantation conditions of Si ϕ1 and ϕ2 are chosen to match the damage profile of boron with doses 7 x 10^{13} cm^{-2} and 5 x 10^{14} cm^{-2} at 10keV.

Si and Ge were implanted into the channel before the gate stack formation. The implant condition matrix is shown in Table 2-1. The damage profiles of the implant conditions ϕ1~ϕ6 are shown in Figure 2-4 and 2-5 as simulated by UT-MARLOWE. In the UT-MARLOWE simulation, normalized interstitial concentration profiles are

generated to represent the degree of amorphization caused by ion implantation damage. In the simulation, a Si substrate was used to approximate the actual multilayer SiGe substrate. It is well known that there is very little difference in the ion implant profiles into Si vs. SiGe at the Ge contents used in this work.

First, the damage profiles were simulated for commonly used boron (7 x 10^{13} and 5 x 10^{14} cm^{-2} both at 10keV) and arsenic ion implantation conditions (1 x 10^{15} at 30 keV) for MOSFET deep source/drain or extension implantation. Then the implantation conditions ϕ1, ϕ2 of Si were designed to match the damage of the boron (B) profiles, as shown in Figure 2-4. To match the average project range (R_p) of the light boron atoms implanted at 10 keV, the implant energy of Si needs to be larger, around 30 keV. Since Ge and As have very close atomic mass, 72.59 and 74.92 respectively, the damage profile of the Ge implant was assumed to be a good match to that of As under the same implant conditions. The same is true for Si and P, which have atomic masses of 28.09 and 30.97 respectively. Other doses for Si and Ge were chosen to represent the cases in the sub-amorphous and amorphous regime where the Si channel was highly damaged, such as ϕ3 and ϕ4 of Si. Condition ϕ5 for Ge implantation had a similar damage profile as that of ϕ3 for Si implantation. This was used to check whether the damage effects depend on the implant species. In summary, the implant doses for Si range from 4 x 10^{12} cm^{-2} to 5 x 10^{14}, and 3 x 10^{13} to 1 x 10^{15} cm^{-2} for the Ge implants.

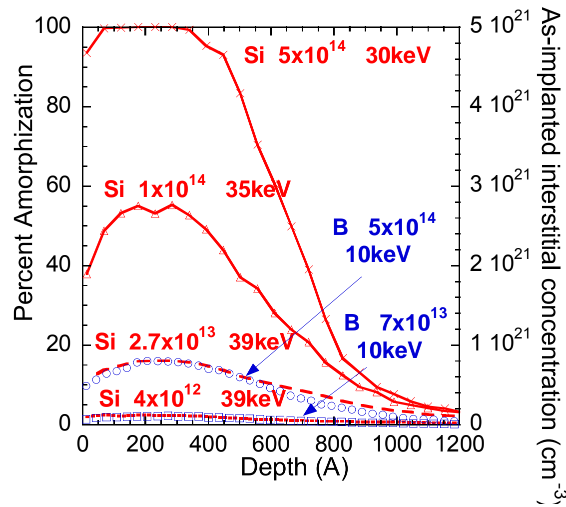

Figure 2-4 Damage profiles for Si implant doses φ1 to φ4, compared to those of boron implants (doses 7 x 10^{13} cm^{-2} and 5 x 10^{14} cm^{-2}, both implanted at 10 keV). The profiles were simulated by UT-MARLOWE. 100% percent amorphization is defined to correspond to an as-implanted interstitial concentration of 5 x 10^{21} cm^{-3}. The right axis shows the as-implanted interstitial concentration profile for these implant conditions.

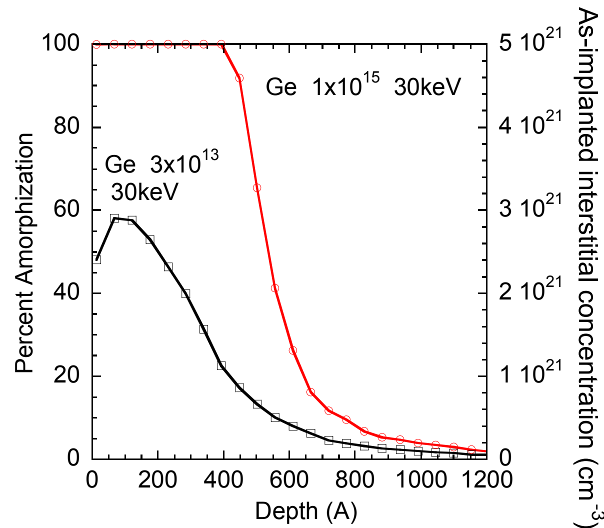

Figure 2-5 Damage profiles of the Ge implant conditions φ5 and φ6, simulated by UT-MARLOWE. The right axis shows the as-implanted interstitial concentration profile for these implant conditions.

Wafers with Strained Si	CZ Control Wafers	RTA Splits	Implant Species	Implant Conditions
E1	CZ1	RTA1	Si	N | ϕ2
E2	CZ2	RTA1	Si	N | ϕ3
E3	CZ3	RTA1	Si	ϕ1 | ϕ4
E4	---	RTA1 (no reoxidation)	Si	ϕ1 | ϕ4
E5	CZ5	RTA2	Si	N | ϕ2
E6	CZ6	RTA2	Si	N | ϕ3
E7	CZ7	RTA2	Si	ϕ1 | ϕ4
E8	CZ8	RTA3	Si	ϕ1 | ϕ4
E9	CZ9	RTA1	Ge	ϕ5
E10	CZ10	RTA1	Ge	ϕ6

Table 2-2 The experimental matrix used in this work. For wafers with Si implants, there is one implant condition on each half of the wafer, i. e., N | ϕ2 means the left half of wafer has no implant, while the right half of the wafer is implanted with condition ϕ2. RTA1, 2, 3 are the annealing conditions: 1000°C for 1 sec, 1000°C for 10 sec and 950°C for 10 sec respectively.

Table 2-2 shows the wafer matrix used in this work. The wafers with epitaxial strained Si/relaxed $Si_{0.8}Ge_{0.2}$ layers are denoted as E1 to E10. The Czochralski control wafers are denoted as CZ1 to CZ10. There are two implant conditions on each wafer for wafers with a Si implant: one implant condition on the left half of the wafer and the other on the right half. For example, N | ϕ2 indicates that the left half of wafer has no implant, while the right half of the wafer is implanted with condition ϕ2. Photoresist was used to protect one half of the wafer while the other half was implanted.

After the implantation, gate oxide layers were grown at 800 °C for 30 minutes in dry oxygen ambient (the total time in furnace was approximately one hour including the temperature ramp up and down). The gate oxide thickness was measured from 43.6 to 47 Å across the boat. 1500 Å polycrystalline silicon was deposited at 625°C on top of the

gate oxide. After gate etch, reoxidation was performed at 800°C on all the wafers for 11 minutes (about 50 minutes in furnace) except wafer E4 (see Table 2-2.), which was used to compare with wafer E3 to check the effects of reoxidation. Phosphorus of dose 5 x 10^{15} cm^{-2} with energy 10keV was implanted as a deep source/drain and gate implant.

In order to investigate the effects of thermal processes on damage annealing and mobility behavior, three different rapid thermal anneals (RTAs) were used: RTA1 at 1000°C for 1 sec, RTA2 at 1000°C for 10 sec and RTA3 at 950°C for 10 sec respectively. In total, 19 wafers were processed successfully. Table 2-2 shows the wafer matrix with the corresponding RTA and implant conditions. After RTAs, contact cuts were patterned. 1000 Å Ti and 1 um Al were sputtered. The metal level was patterned using wet etch. The metal was sintered at 400°C for 40 minutes in forming gas.

2.3 Electrical Characteristics and Medici Simulations

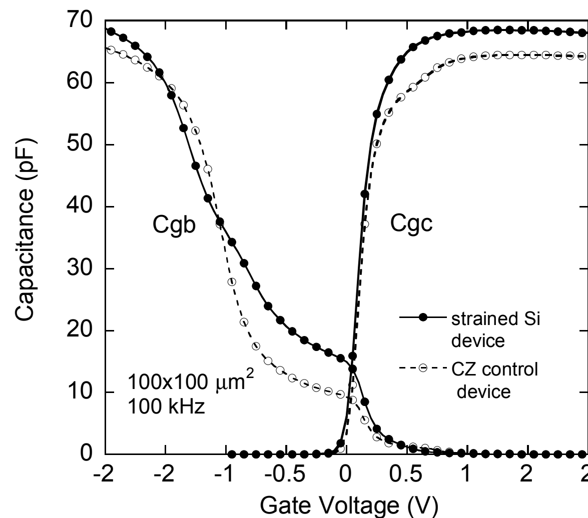

Figure 2-6 Split C-V measurements for a strained Si and a bulk *n*-MOSFET.

The electron mobility was extracted from I_d-V_g and split C-V measurements. Figure 2-6 shows the split C-V measurement of wafer E1 and wafer CZ1 on devices of size 100 x 100 μm^2. The gate to body capacitance (C_{gb}) and gate to channel capacitance (C_{gc}) were measured. From the C_{gc} curve, it is clear that there is some poly-depletion for the devices with RTA1, which indicates that the dopants are not fully activated. The threshold voltages (V_{th}) of both devices are very close. The reason is that the doping levels of epi wafers are higher than those of CZ wafers, which cancels out the V_{th} drop for strained Si devices due to energy band differences.

The mobility was calculated using Equation 2-1 and 2-2 below. The mobility of the devices on the same wafer with the same implant condition can be different by 10% mainly due to processing non-uniformity. In the figures below, a comparison is made between the different mobility curves. However, it should be noted that any difference less than 15% is within the error of this experiment.

$$E_{eff} = \left(\frac{1}{\varepsilon_{Si}}\right)\left(aQ_{depl} + bQ_{inv}\right)$$

Equation 2-2-1

$$\mu_{eff} = \left(\frac{L}{W}\right)\frac{g_d}{Q_{inv}}$$

Equation 2-2-2

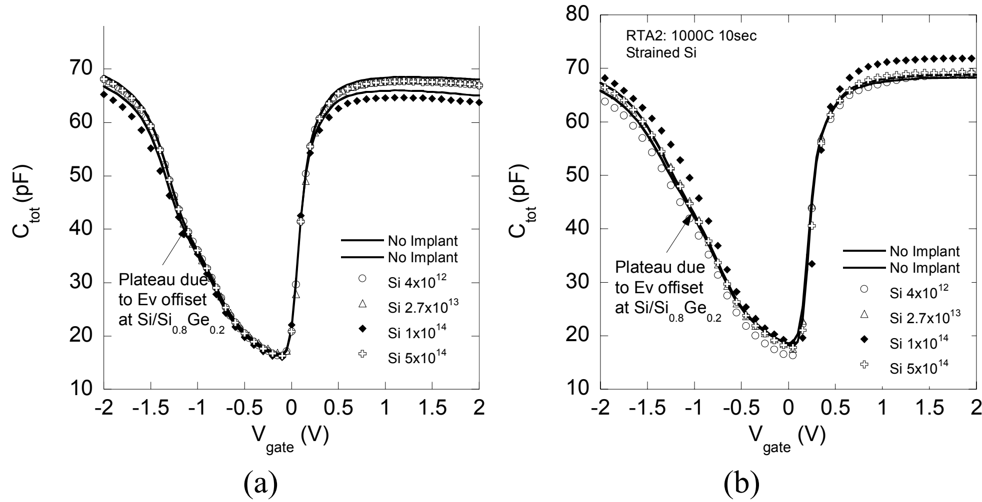

Figure 2-7 Total capacitances C_{tot} vs. V_{gate} for strained Si with (a) RTA1, 1000 °C for 1 sec, and (b) RTA2, 1000 °C for 10 sec.

The total capacitance C_{tot} was calculated as the sum of C_{gb} and C_{gc}. Figure 2-7 shows the C_{tot} vs. V_{gate} curves of the strained Si devices with different implantation conditions. The C_{tot} curves overlap very well, which indicates that the devices have similar channel doping, band structures and thickness of strained Si layers. In Figure 2-7 (a), the small plateau in the left half of C_{tot} is caused by the discontinuity of the valence band at the strained $Si/Si_{0.8}Ge_{0.2}$ interface as shown in Figure 2-8 (b). The vertical position of the plateau is determined by the thickness of the strained Si layer: the thicker the layer is, the lower the plateau is. The plateau in Figure 2-7 (b) is more subtle than that in Figure 2-7 (a), which indicates a smeared out interface by Ge out diffusion into the strained Si layer during RTA2 (1000 °C for 10 sec). The C-V curves can be simulated by Medici as a means to determine the thickness of the strained Si layer.

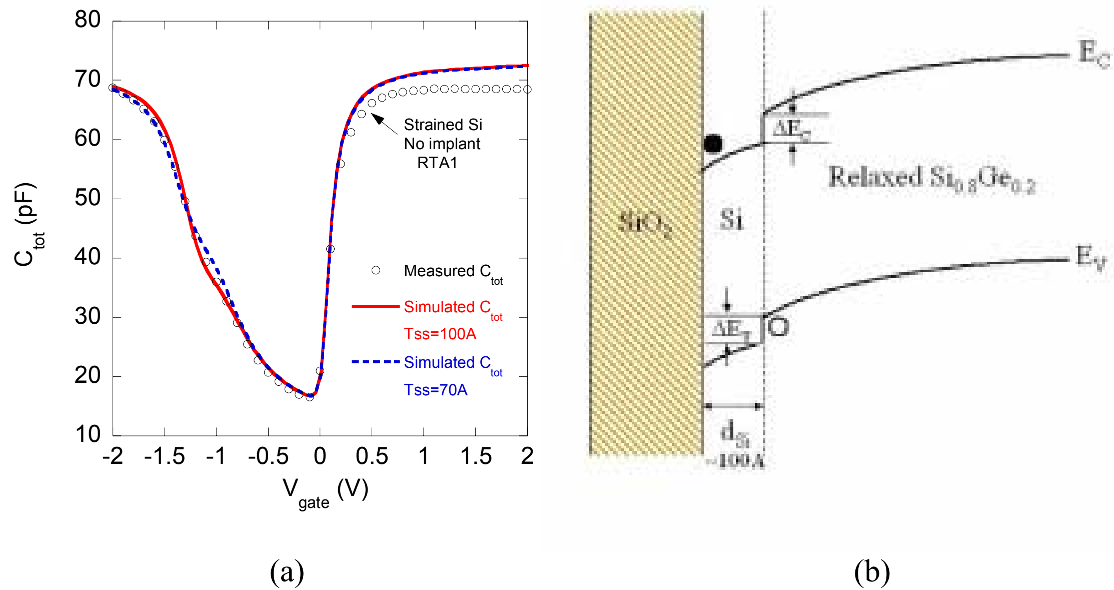

(a) (b)

Figure 2-8 (a) C_{tot} curves simulated by Medici with different thicknesses of the strained Si layer compared with the measured Ctot. The simulation with 100 Å strained Si layer matches the measured data better than that of 70 Å. (b) band diagram of a strained Si MOSFET in the depletion regime. Holes are accumulated at the strained Si/ relaxed $Si_{0.8}Ge_{0.2}$ interface due to the band discontinuity.

Figure 2-8 (a) shows the C_{tot} curves simulated by Medici for different thicknesses of the strained Si layers. The dotted curve is the simulated C_{tot} for devices with 100 Å thick strained Si; while the solid curve represents C_{tot} for devices with 70 Å strained Si. The position of the small plateau is higher for the device with thinner strained Si layer. The C_{tot} curve with 100 Å strained Si layer matches the measured data better than that of 70 Å. Figure 2-8 (b) illustrates the band discontinuity at the interface of the strained Si and the relaxed $Si_{0.8}Ge_{0.2}$ virtual substrate of the strained Si MOSFETs. The plateau of the C_{tot} curve is the result of this band discontinuity.

As explained in Section 2.1.1 above, it is reasonable to assume the critical thickness of the strained Si layer on $Si_{0.8}Ge_{0.2}$ of this process is about 120 Å. It should be noted that it is the thickness of the strained Si layer during thermal processing which determines the strain relaxation behavior, not the final thickness after processing. In this process, the

starting thickness of the strained Si layer was about 180 Å. During processing, the strained Si was partially consumed by surface cleaning and oxidation. Just before the first thermal process, gate oxidation, the strained Si layer has gone through two post-implantation cleans and two RCA cleans. The thickness of the strained Si layer at this point was about 130 Å, close to the estimated critical thickness for strained Si on relaxed $Si_{0.8}Ge_{0.2}$. It is possible that misfit dislocations nucleate and propagate during the gate oxidation, reoxidation and RTAs. As discussed in subsequent sections, materials analysis is required to give a detailed picture of the damage profile and the thermal processes.

2.4 Mobility Dependence on Processing Factors

Figure 2-9 shows the effective mobility curves for the strained Si devices with different implant conditions. All the devices measured here have the same reoxidation step. Figure 2-9 (a) shows the mobility curves for devices with RTA1 (1000 °C for 1 sec). In Figure 2-9 (a), the electron mobility for devices with no implant shows an enhancement factor of 1.7X over the universal electron mobility by Takagi *et al.* at E_{eff} = 0.7 MV/cm. It is seen that the effective mobility degrades monotonically with increasing implant dose. No mobility degradation is observed for Si implant doses of 4 x 10^{12} cm^{-2} and 2.7 x 10^{13} cm^{-2}. For doses 1 x 10^{14} and 5 x 10^{14} cm^{-2}, at E_{eff} = 0.7 MV/cm, the enhancement factor degrades from 1.7X to 1.3X and 1.2X~1.0X (mobility range from measurement) respectively, which implies the mobility enhancement from strain induced energy band splitting is reduced.

Looking back at Figure 2-2, which shows 20% higher mobility from Rim's process than from H. Nayfeh's process, 7 x 10^{13} cm^{-2} B channel implant is used in the latter process, which is equivalent to a Si implant doses of 4 x 10^{12} cm^{-2} in terms of implant

damage. From the mobility curves in Figure 2-9 (a), devices with a Si implant dose of 4 x 10^{12} cm^{-2} and a 1000 ºC 1 sec RTA have the same mobility as those without a channel implant. Therefore, the use of a B channel implant in Nayfeh's process does not seem to explain the 20% difference between the electron mobilities in Figure 2-2. Another possibility is thermal budget difference between these two processes, which is addressed in Section 2.5 by SIMS measurements.

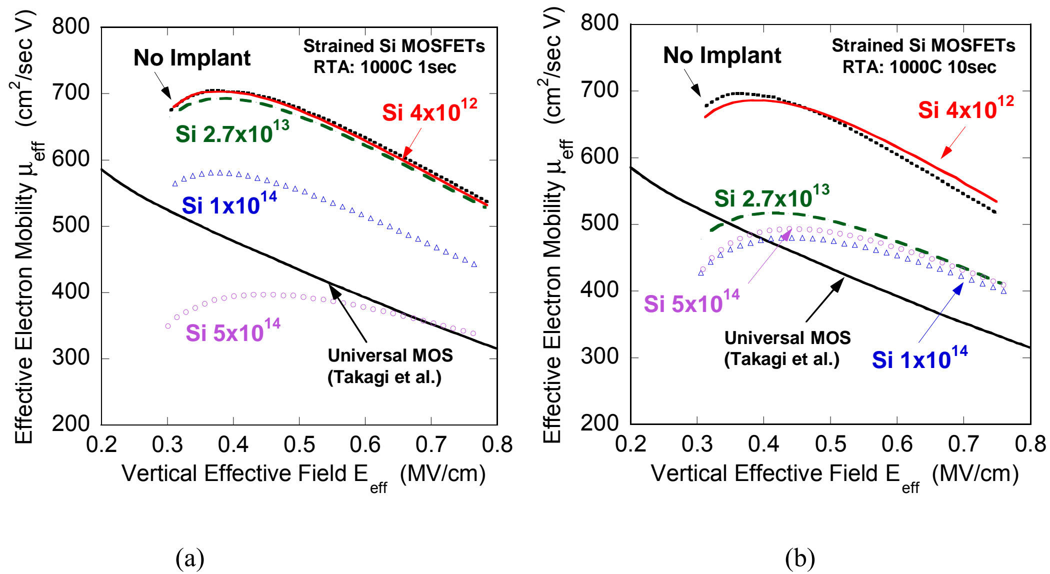

(a) (b)

Figure 2-9 The effective mobility vs. E_{eff} for strained Si n-MOSFETs with different implantation conditions in the channel, for (a) devices with RTA1, 1000 °C for 1 sec, and (b) devices with RTA2, 1000 °C for 1 sec. The measurements were made on 100 x 100 μm^2 devices.

Figure 2-9 (b) shows the mobility curves for strained Si devices with RTA2 (1000 °C for 10 sec). The mobility for devices with no implant in (b) is very close to that in (a), which means that RTA2 without implantation doesn't cause strain relaxation or mobility degradation. This agrees with the observation of S. B. Samavedam *et al.* [33]. Based on their work, strained Si layers are significantly resistant to plastic strain relief by misfit dislocations during high temperature anneal. What causes the degradation is the combination of implantation damage and higher thermal budget. For the higher thermal

budget process shown in Figure 2-9 (b), the mobility starts to show degradation with a dose of 2.7 x 10^{13} cm^{-2}. The devices with implant doses 2.7 x 10^{13}, 1 x 10^{14} and 5 x 10^{14} cm^{-2} have the same mobility to within experimental error. Neutral Si atoms scattering may also play a role in the mobility degradation [36], which can be viewed as essentially scattering from residual defects due to the implant damage.

Comparison between Figure 2-9 (a) and (b) shows that RTA makes a significant difference for devices with intermediate doses, e.g. 2.7 x 10^{13} cm^{-2} and 1 x 10^{14} cm^{-2}. For higher thermal budget processing, mobility starts to degrade for devices with lower doses. We can define a ***critical implant dose*** $\boldsymbol{\phi_{cr}}$ for a certain thermal budget, above which the mobility degrades significantly, but the mobility enhancement still exists. From Figure 2-9, it is seen that ϕ_{cr} for RTA1 is in the range from 2.7 x 10^{13} cm^{-2} to 1 x 10^{14}, while the ϕ_{cr} for RTA2 is in the range from 4 x 10^{12} cm^{-2} and 2.7 x 10^{13} cm^{-2}. As the thermal budget increases, ϕ_{cr} decreases. The interaction of thermal processing and implant damage is responsible for this trend.

After amorphization and during annealing, solid-phase epitaxy of Si starts at a relatively low temperature of 500 °C [37]. The regrowth rate has an exponential relationship with temperature. Since our first thermal step is gate oxidation at 800 °C for an hour, solid-phase epitaxy of the amorphized layer (in the case of high implant doses) should be completed during this step. However, the end-of-range dislocation loops will be present after the regrowth of the amorphized Si layer. These dislocation loops can act as scattering centers and the nucleus for the misfit dislocations to grow, which result in strain relaxation and mobility degradation.

Figure 2-10 shows the effect of reoxidation on mobility for strained Si wafers with the lowest Si implant dose 4 x 10^{12} cm^{-2} and the highest Si dose 5 x 10^{14}. The reoxidation was performed at 800°C for about 50 minutes in furnace. The solid lines are the mobility curves for devices without reoxidation, and the dotted lines for those with reoxidation. Within the error bar, there is no difference between the devices with and without reoxidation for either dose.

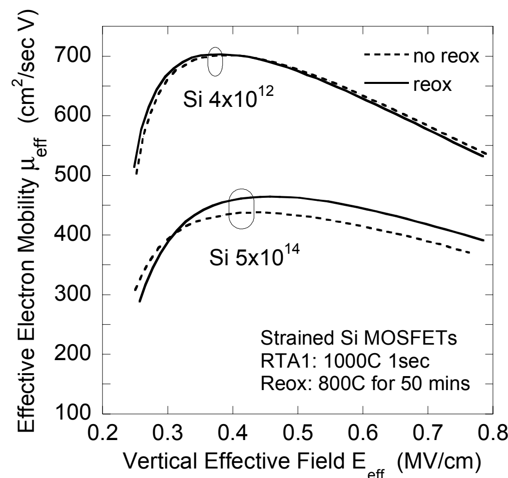

Figure 2-10 Comparison of the effective mobility curves for strained Si MOSFETs with or without reoxidation. The implant conditions are ϕ1 and ϕ4, with same annealing step RTA1.

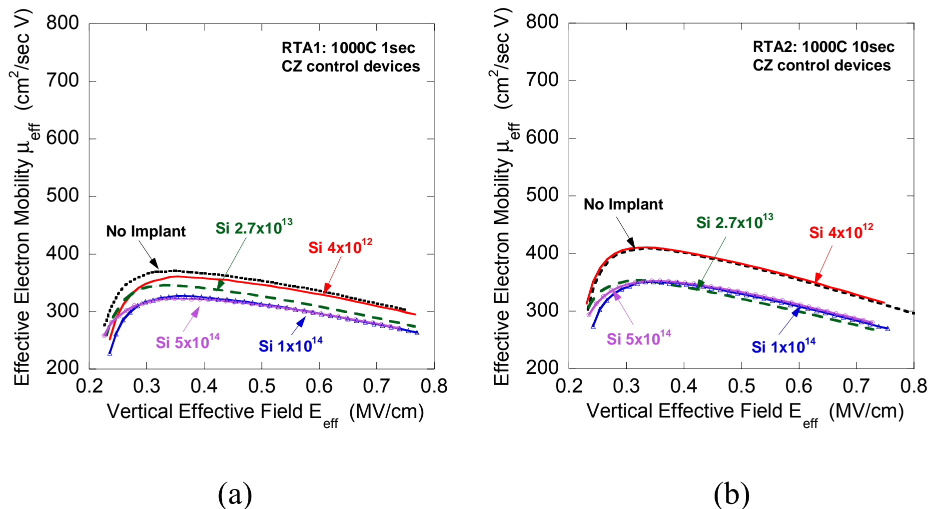

(a) (b)

Figure 2-11 The effective mobility vs. E_{eff} for the CZ control devices with different implantation conditions for (a) devices with RTA1, and (b) devices with RTA2. The measurements were made on 100 x 100 μm^2 devices.

Figure 2-11 shows the dependence of mobility on implant dose and RTA for CZ control devices. In the CZ control wafers, there are no issues with strain relaxation and Ge diffusion due to thermal processing, therefore the mobility degradation is mainly due to ion implantation damage. Compared with the strained Si devices, the CZ control devices have much less dependence on implantation dose and thermal budget.

Figure 2-12 compares the mobility curves of devices with the 3 RTA splits. The comparison is made on devices with the lowest (4×10^{12} cm^{-2}) and the highest (5×10^{14} cm^{-2}) Si implant doses. Compared with the strong RTA dependence seen at intermediate doses, for doses of 4×10^{12} and 5×10^{14} cm^{-2}, the RTAs used in this work do not have a strong effect on the mobility. This is true for both strained Si and CZ MOSFETs. In Figure 2-12 (a), the devices with 4×10^{12} cm^{-2} dose implant have the same mobility as those without implant. This indicates that the critical doses ϕ_{cr} for these three thermal budgets are higher than 4×10^{12} cm^{-2}.

Figure 2-13 shows the mobility at $E_{eff} = 0.7$ MV/cm for strained Si and CZ control devices vs. implant doses for different RTAs. The comparison is performed at this particular field to ensure that the Coulomb-scattering-limited mobility has little influence on the total mobility, and thus the measured mobility is closer to the universal mobility for strained Si (see Figure 2-14).

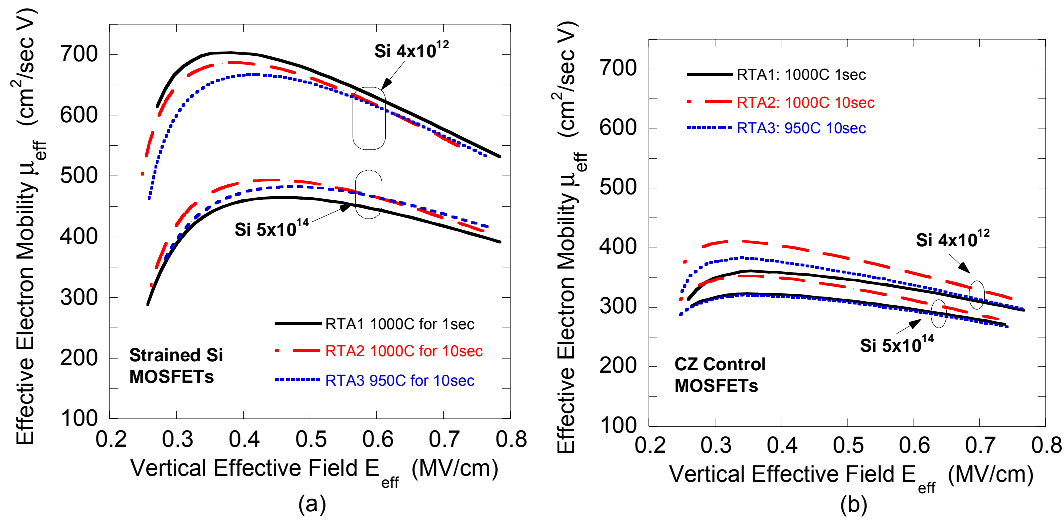

Figure 2-12 Effective mobility vs. vertical effective field E_{eff} for strained Si and CZ control devices with different RTAs. The doses are the lowest, 4 x 10^{12} cm^{-2} and the highest 5 x 10^{14} cm^{-2}. RTA1, 2, 3 are 1000°C for 1 sec, 1000°C for 10 sec and 950°C for 10 sec respectively.

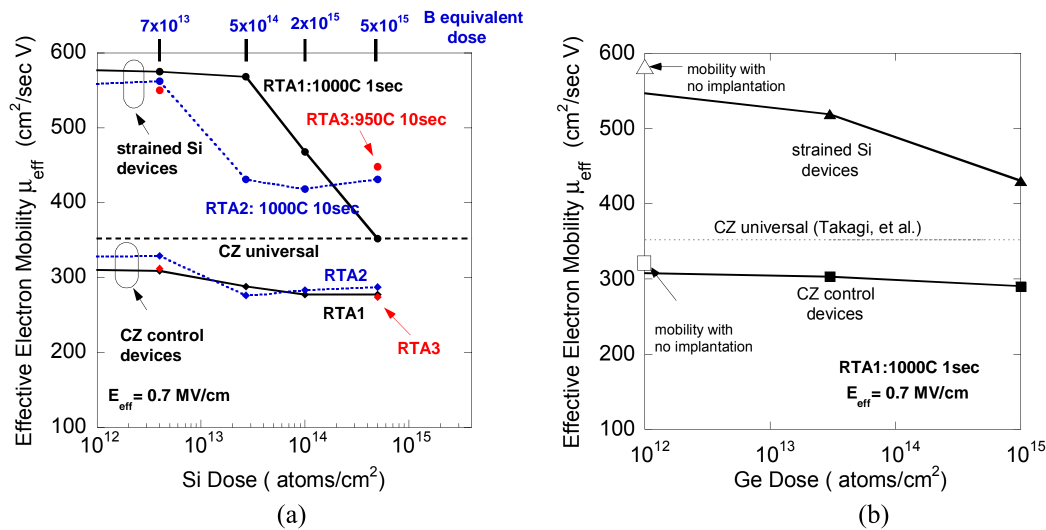

Figure 2-13 Effective mobility at E_{eff}=0.7 MV/cm for strained Si and CZ control devices of different species, doses and RTA, for (a) devices with Si implant, (the equivalent boron dose is shown on the upper x axis), and (b) devices with Ge implants.

It is seen in Figure 2-13 (a) that the mobility for strained Si MOSFETs starts to degrade at a certain critical dose Φ_{cr}. This critical dose Φ_{cr} depends on the thermal budget. For example, mobility starts to degrade at Si dose of 3 x 10^{13} cm^{-2} for RTA1

(1000 °C 1 sec), while the critical dose for Si with RTA2 (1000 °C 10 sec) is about 4 x 10^{12} cm^{-2}. Below this critical dose, mobility degradation is negligible. As mentioned above, the damage profiles for Si are very close to those of P. Therefore, the critical doses for Si should be good approximations to those for P for similar thermal budgets. The B equivalent doses in term of damage profiles are shown in Figure 2-13 (a). From (a), the critical dose for B implanted devices with RTA1 (1000 °C 1 sec) is estimated to be about 5 x 10^{14}, while for those with RTA2 (1000 °C 10 sec) is about 7 x 10^{13} cm^{-2}.

It should be noticed that the critical doses Φ_{cr} obtained in this work are based on the study of neutral implant Si and Ge without considering Coulomb scattering effects by ionized dopants. The term "equivalent dose" refers to the ion implant damage profiles. If Coulomb effects are included, the critical dose for dopant species B, P, and As is expected to be lower than observed here. Since the implant dose and energy determine the as-implant damage profile as seen in Figure 2-4 and Figure 2-5, a critical dose corresponds to a critical as-implanted damage level in the channel. Therefore the critical doses 4 x 10^{12} cm^{-2} and 3 x 10^{13} cm^{-2} for Si implant under RTA1 and RTA2 correspond to an as-implanted interstitial concentration of 1 to 8 x 10^{20} cm^{-3} according to UT-MARLOWE simulations, as shown in Figure 2-4.

Figure 2-13 (b) shows the mobility at E_{eff} = 0.7 MV/cm for Ge implanted devices with RTA1 (1000 °C 1 sec). The critical dose for Ge and thus As with RTA1 is about 1 x 10^{12} cm^{-2}. The highest damage in this process is from Ge with a dose of 10^{15}. From the UT-MARLOWE simulation, the channel is completely amorphized. The mobility extracted from Ge-damaged devices shows less degradation than that of Si implanted

devices with lower damage levels. The mobility is higher than the universal mobility of CZ devices, which indicates that there is still some strain left in the Si layer.

2.5 Mobility Degradation Mechanisms

Ion implantation and thermal processes are shown to degrade the mobility in strained Si MOSFETs. Three mechanisms might be responsible for the degradation: strain relaxation due to misfit dislocation nucleation and propagation, residual ion implantation damage, and Ge out-diffusion into the Si cap layer. To verify the potential explanations, materials analysis was performed. Cross section TEM was used to study the implant damage and misfit dislocations in the layers. Secondary ion mass spectrometry (SIMS) was used to obtain Ge diffusion profiles.

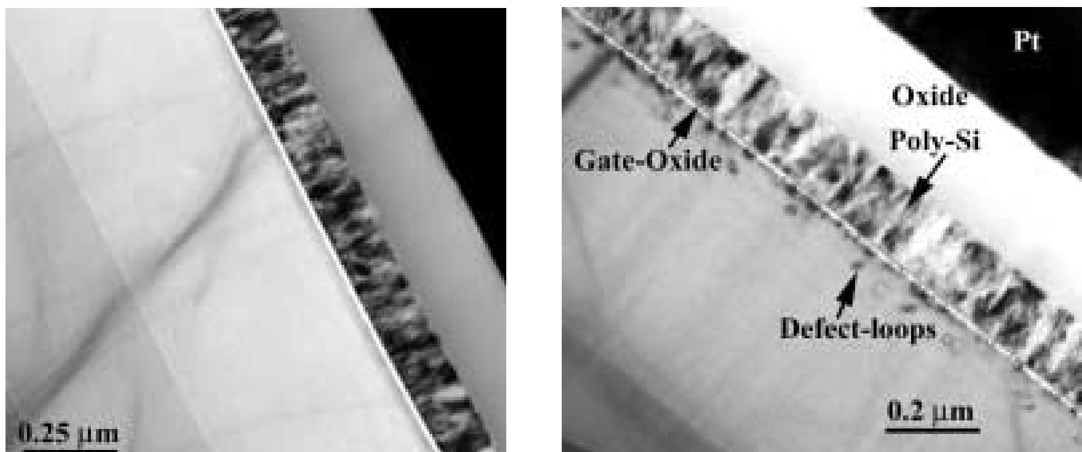

Figure 2-14 Cross section TEM micrographs for strained Si devices with RTA1 (1000 °C for 1 sec) and Si implants, for (a) devices with no implant, and (b) devices with Si implant ϕ 4 (dose 5 x 10^{14} cm^{-2}). TEM courtesy of D. H. Anjum at the University of Virginia.

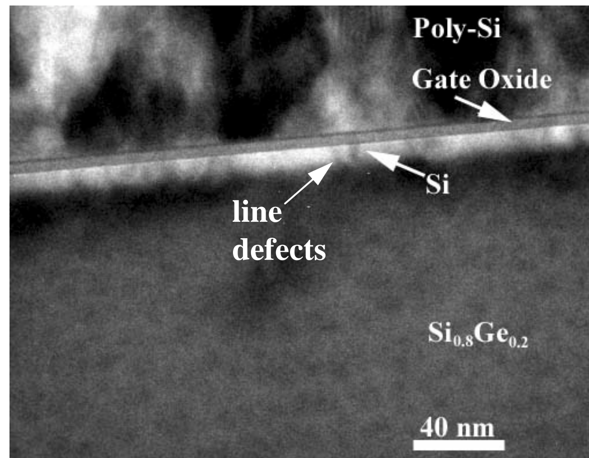

Figure 2-15 Cross-section TEM micrographs for a strained Si device with RTA1 (1000 °C for 1 sec) and Si implant Φ4 (dose 5 x 10^{14}). This is an image of higher magnification taken on the same sample as shown in Figure 2-14 (b). TEM courtesy of D. H. Anjum at University of Virginia.

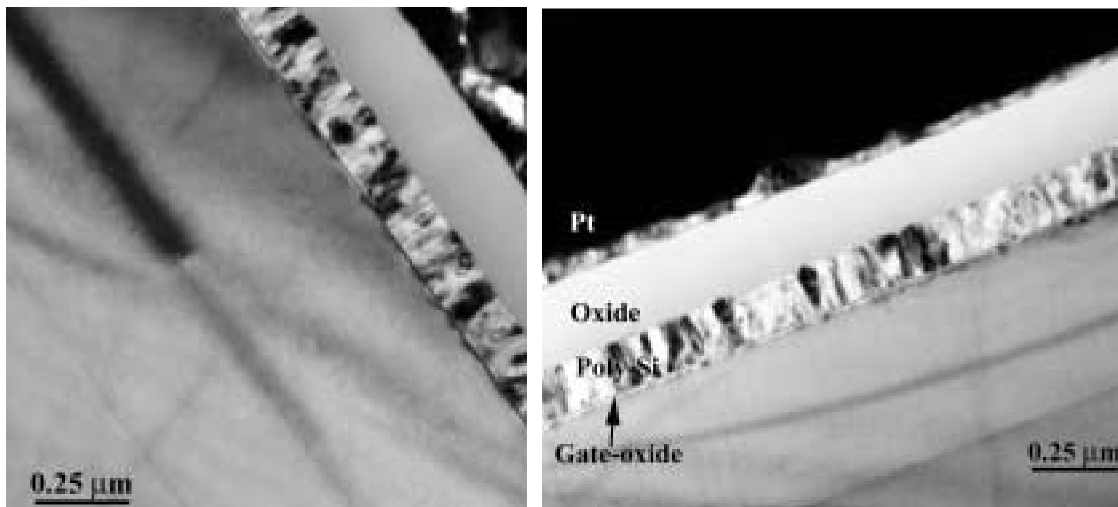

Figure 2-16 Cross-section TEM micrographs for strained Si devices with RTA2 (1000 °C for 10 sec) and Si implants for (a) devices with Si implant Φ2 (dose 2.7 x 10^{13} cm^{-2}), and (b) devices with Si implant Φ4 (dose 5 x 10^{14}). TEM courtesy of D. H. Anjum at University of Virginia.

For devices without implantation, no damage is observed in the channel as in Figure 2-14 (a). For devices with the highest Si implant dose Φ4 (5 x 10^{14}) and RTA1 (1000 °C 1 sec), implantation damage such as defect loops and dislocations are clearly seen in Figure 2-14 (b) and 2-15. The amount of residual damage depends on the thermal

budget. The residual damage is less for devices with RTA2 (1000 °C 10 sec) than those with RTA1 (1000 °C 1 sec), which means that longer RTA time anneals out implantation damage, as seen in Figure 2-14 (b) and 2-16 (b). For devices with RTA2 (1000 °C 10 sec), the residual damage with implant dose 2.7 x 10^{13} cm^{-2} and 5 x 10^{14} cm^{-2} is very similar (Figure 2-16). Figure 2-17 shows the cross-section TEM images of the devices that have been Ge implanted. The residual damage is consistent with the mobility data. The more residual damage present in the Si channel, the lower the mobility. Therefore, residual implantation damage is one of the mechanisms for mobility degradation seen in this work.

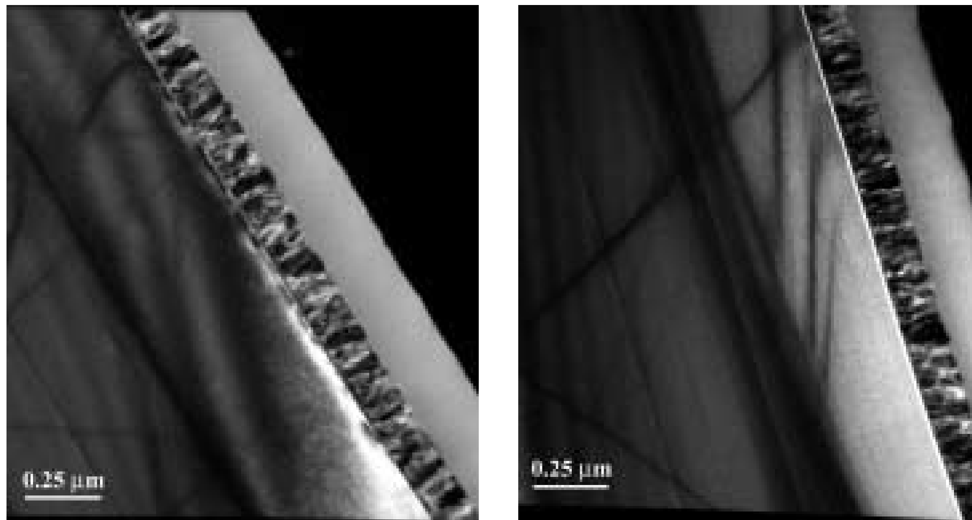

Figure 2-17 Cross-section TEM pictures for strained Si devices with RTA1 (1000 °C for 1 sec) and Ge implants for (a) devices with Ge implant Φ5 (dose 3 x 10^{13} cm^{-2}), and (b) devices with Ge implant Φ6 (dose 1 x 10^{15}). TEM courtesy of D. H. Anjum at University of Virginia.

It is also seen in this work that a higher thermal budget itself, without implantation, does not degrade the mobility. This agrees with the experimental work by Currie *et al.* [22], where strained Si MOSFETs were fabricated on $Si_{0.7}Ge_{0.3}$ virtual substrates and annealed at 1000 °C for 1-30 sec. In the present work, with no implantation damage in

the channel, the mobility enhancement factor is seen to degrade from 1.7X for devices with 1000 °C 1 sec RTA to 1.6X for those with 1000 °C 10 sec anneal. In section 2.4, the mobility of devices with RTA2 (1000 °C 10 sec) seems to reach a plateau with the increasing dose (Figure 2-13 (a)), which indicates that the mobility is independent of implant dose. One possible explanation is that for RTA2 Ge diffusion becomes the dominant mechanism for mobility degradation.

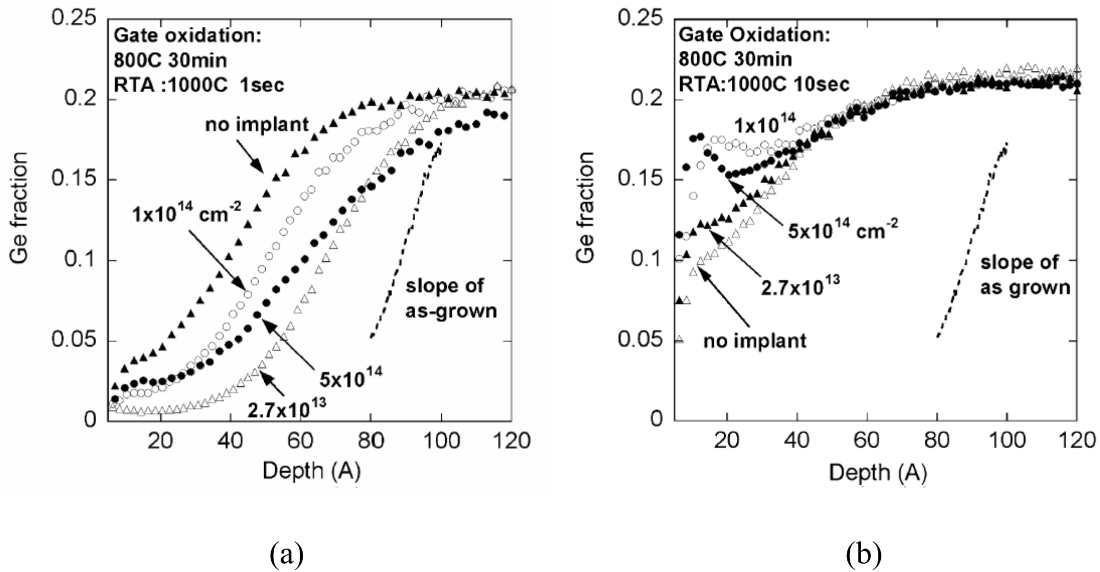

Figure 2-18 SIMS profiles for Ge in strained Si MOSFETs for (a) RTA1 (1000 °C 1 sec), and (b) RTA2 (1000 °C 10 sec).

To verify this hypothesis, SIMS was used to obtain Ge profiles as shown in Figure 2-18. In this experiment, the as-grown thicknesses of the strained-Si epitaxial layer varied by as much as 30 Å from wafer-to-wafer, which causes the Ge profiles to shift laterally by up to 30 Å in Figure 2-18. Therefore, the Ge profile slopes rather than their positions are evidence of Ge diffusion in this plot. In Figure 2-18 (a) and (b), the as-grown sample has a steeper Ge profile than any of the processed samples, indicating that some Ge diffusion took place during MOSFET processing. For samples annealed at 1000 °C for 1 sec, the surface Ge fractions are very close for samples both with and without mobility

degradation (e.g., the transistors without ion implantation and with a Si dose of 5 x 10^{14} cm^{-2} have similar Ge surface concentrations, but very different mobility values). Therefore, Ge up-diffusion is not the primary cause for the mobility degradation for the samples that received the 1000 °C 1 sec RTA. Figure 2-18 (b) shows the Ge profiles for 1000 °C 10 sec RTA. Compared to Figure 2-18 (a), Ge diffuses much more during the longer RTA. Ge diffuses most in the samples with the two highest implant doses, 1 x 10^{14} and 5 x 10^{14} cm^{-2}, most likely due to implant damage enhanced Ge diffusion. The near-surface Ge fraction in Figure 2-18 (b) increases with increasing implant dose. Therefore, Ge up-diffusion is likely to be the key mechanism for the mobility degradation seen in the samples annealed at 1000 °C for 10 sec.

Looking again at Figure 2-2, 20% higher mobility is shown for Rim's process than for H. Nayfeh's process. The SIMS data in Figure 2-18 provide a possible explanation. In Rim's study, the gate oxide was grown at 800 °C and source/drain implant annealing was 2 min at 650 °C and 15 sec at 850 °C [7]. In Nayfeh's process flow, gate oxide was grown at 800 °C and RTA was performed at 1000 °C for 1 sec [35]. Si-Ge interdiffusion is exponential with temperature as discovered in Chapter 4. Therefore, in Rim's process, the Ge profile motion should not be observable. In comparison, Nayfeh's thermal budget is the same as this work (1000 °C 1 sec), and should have similar diffused Ge profile as shown in Figure 2-18 (a), which is significant compared to the as-grown Ge profile. Therefore, it is possible that the lower mobility in Nayfeh's process is due to more Si-Ge interdiffusion.

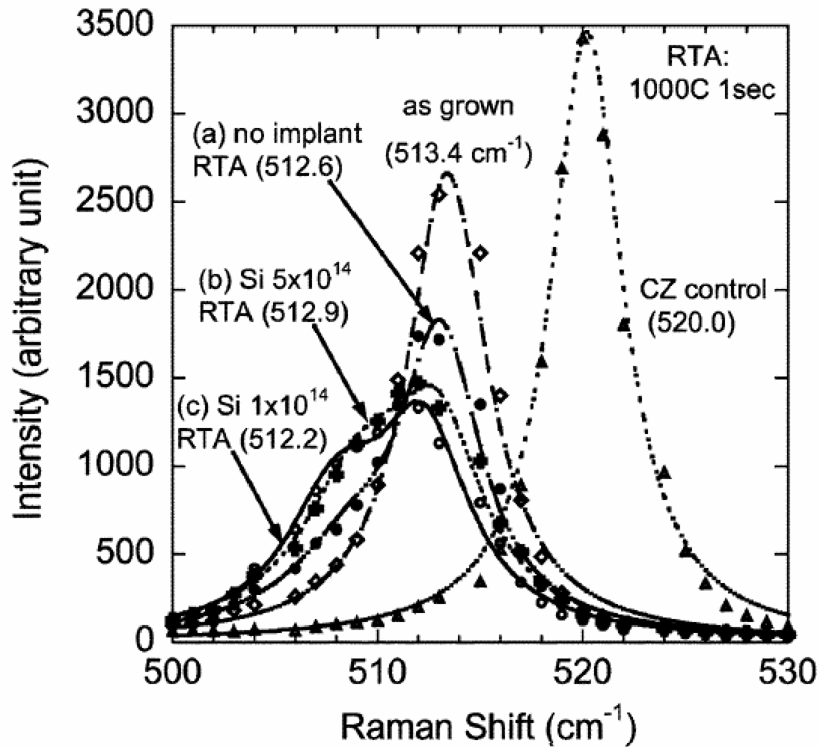

Figure 2-19 Raman scattering spectra (325-nm excitation) for unstrained-Si, as-grown fully strained-Si on $Si_{0.8}Ge_{0.2}$, and strained-Si on $Si_{0.8}Ge_{0.2}$ samples after processing, including 1000 °C 1 sec RTA. The symbols are Raman data and the lines are Lorentz fits to the data. Raman spectra (a)–(c) are fitted by two Lorentzian functions to account for the signal from the underlying $Si_{1-x}Ge_x$ ($x < 0.2$) layer formed by Ge up-diffusion. The numbers in parentheses are the Si-Si phonon peak positions from the Si layer (as opposed to the $Si_{1-x}Ge_x$ layer). Raman data courtesy of N. Klymko at IBM.

Another hypothesis to explain the observed mobility degradation in this work (Figure 2-9 and Figure 2-13) is strain relaxation due to ion implantation damage and thermal processing. In the PVTEM images, no misfit dislocations are observed. Raman spectroscopy was performed to check for strain relaxation in the Si, perhaps by defects other than misfit dislocations. Raman analysis was performed using 325-nm excitation, which samples approximately the top 10 nm. Figure 2-19 shows the Raman spectra of the unstrained-Si, as-grown fully strained-Si on relaxed SiGe, and strained-Si with and without implantation after 1000 °C 1 sec RTA. In Figure 2-19, the large peak at 520.0 cm^{-1} is due to the Si phonon mode of unstrained-Si, and the peak at 513.4 cm^{-1} is due to

the Si-Si mode in the as-grown fully strained-Si layer on relaxed Si Ge . Tensile strain in Si layer shifts the Raman peak to the left in proportion to the biaxial stress, and the relaxation of tensile strain shifts the peak toward the unstrained-Si peak at 520.0 cm^{-1} [38]. In Figure 2-19, the samples with 1000 °C 1 sec RTA and different implant doses show no shift to the right. Therefore, strain relaxation is not observed in these samples and is not considered to be a major mechanism for mobility degradation for the 1000 °C 1 sec RTA. Broadening and asymmetry of the spectra in samples (a), (b), and (c) are observed in Figure 2-19. These effects are likely due to the residual disorder and the diffusion of Ge into the strained-Si layer [39]. It should be noted that this Raman analysis samples the top 10 nm of the semiconductor. On wafers with Ge diffusion into the strained-Si layer, a thin buried, strained-SiGe layer will be formed. The signal from this layer could be responsible for the shoulder observed near 509 cm^{-1}.

In summary, materials analysis indicates that residual ion implantation damage is the key mobility degradation mechanism for devices annealed at 1000 °C for 1 sec, while implant damage enhanced Ge up-diffusion is the key mobility degradation mechanism for the MOSFETs annealed at 1000 °C for 10 sec.

2.6 Impact on Technology

Phosphorus, boron and arsenic are widely used in current CMOS technology. Among the various implants, source and drain (S/D) extension, halo and channel implants are located closest to the channel, which can introduce implant damage near the channel region and affect the mobility behavior. In 50-nm node technology, typical doses for As and B S/D extension implants are in the range of 10^{14} and 10^{15} cm^{-2} respectively. For halo implants, the typical dose for As and B is 10^{14} cm^{-2}. The critical doses for uniformly implanted As and B were estimated to be to 10^{12} to 10^{13} cm^{-2} and 7 x 10^{13} to 5 x 10^{14} cm^{-2} respectively, depending on the thermal budget. Arsenic implants are thus expected to be more problematic than boron implants.

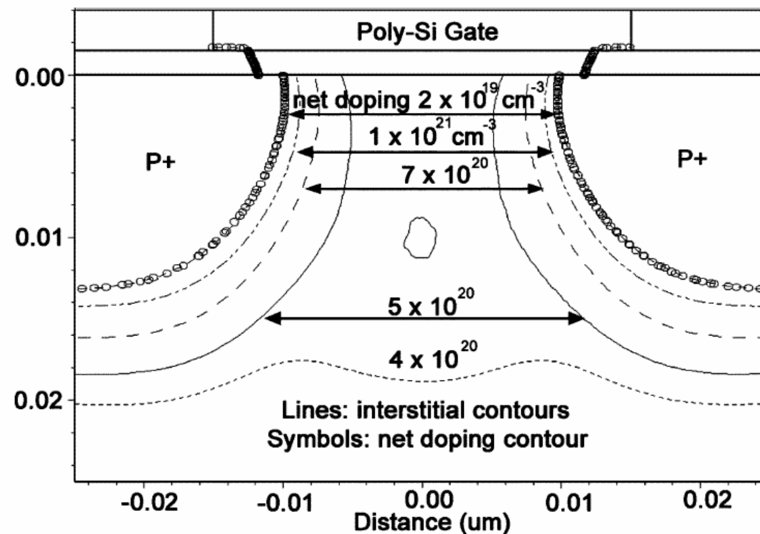

Figure 2-20 As-implanted interstitial contours (lines) for a 30-nm gate length p-MOSFET simulated by TSUPREM-4 using analytic ion implant models. The simulation employed As halo implants at 30 keV with 38 tilt to a dose of 3 x 10^{13} cm^{-2} , and B S/D extensions implanted at 0.7 keV with 0 tilt to a dose of 3 x 10^{14} cm^{-2} B. The implant moment tables used are "ARSENIC" for As and "TR.BORON" for B. The symbols show the contour corresponding to a net doping concentration of 2 x 10^{19} cm^{-3}.

In order to estimate two-dimensional (2-D) implant damage in more realistic device structures, a process simulation tool, TSUPREM-4 [40], was used to simulate as-implanted interstitial profiles in MOSFETs with halo implants. In the UT–MARLOWE simulations (Figure 2-4), interstitial concentration is a measure of implant damage. The parameters in the TSUPREM-4 simulations were calibrated in order to match the simulated as-implanted interstitial profiles generated by one-dimensional UT–MARLOWE simulations. Figure 2-20 shows 2-D as-implanted interstitial contours of a 30-nm gate length p-MOSFET simulated using TSUPREM-4. The as-implanted interstitial concentration in the channel region is approximately 5 x 10^{20} cm^{-3}, which is roughly equivalent to that produced by uniform Si implants with a dose of 2.7 x 10^{13} cm^{-2} (see Figure 2-4 (a)). In the uniformly implanted, long-channel n-MOSFETs fabricated in this work, that dose resulted in a significant electron mobility degradation for 1000 ºC, 10 sec annealing in Figure 2-9 (b), but no significant mobility degradation was observed for 1000 ºC, 1 sec annealing in Figure 2-9 (a). Thus, it is expected that there should be an annealing condition window in which the damage from the As halo implants can be annealed without significant hole mobility degradation in 30-nm scale strained-Si p-MOSFETs, when optimized ion implant energy and angle are used. Two-dimensional simulations were also carried out for 30-nm n-MOSFETs (not shown). In that case, the channel-region as-implanted interstitial concentration is on the order of 10^{20} cm^{-3}, which is approximately the peak interstitial concentration associated with a Si dose of 4 x 10^{12} cm^{-2}, see Figure 2-4 (a). This low dose implant did not induce significant electron mobility degradation in our experiments for 1000 ºC, 1 or 10 sec annealing. Thus, implant damage will be less of an issue for scaled strained-Si n-MOSFETs than for p-MOSFETs.

In summary, the impact of ion implantation and rapid thermal annealing on electron mobility enhancement in strained-Si/relaxed SiGe n-MOSFETs has been investigated. Electron mobility enhancement is shown to degrade considerably when the implant dose is above a certain critical dose for a given annealing condition. The critical doses of Si and Ge and the inferred equivalent P, B and As critical doses were obtained quantitatively. Implant damage enhanced Ge up-diffusion was observed. Residual implant damage and Ge up-diffusion were shown to be the major mechanisms for mobility degradation for 1000 ºC 1 sec and 1000 ºC 10 sec RTA respectively. In designing the annealing conditions for high dose implants, there is a strong trade-off between damage annealing (which requires longer times) and Ge up-diffusion. Further investigation, particularly at lower temperatures, needs to be done to locate an annealing regime where effective defect annealing takes place while Ge diffusion is minimized. The simulated damage range for n-MOSFETs in the 30-nm-scale regime is lower than would be expected to cause mobility degradation based upon the analysis of the uniform channel implants studied in this paper. For 30-nm-scale strained-Si p-MOSFETs, however, the annealing conditions will need to be more carefully optimized to avoid mobility degradation associated with As (halo) and B (source/drain) implants.

2.7 Chapter Summary

In chapter 2, the study of thermal processing and ion implantation impact on mobility enhancement in strained Si n-MOSFETs was presented. This chapter began with the introduction to the background of Si/SiGe processing including the critical thickness of strained Si on relaxed SiGe. Available literature showed that mobility degrades under high thermal budget and high dopant ion implantation. Section 2.2 described the

experimental matrix, which included four different Si implant doses (from 4 x 10^{12} to 5 x 10^{14} cm^{-2}), two Ge implant doses, and two RTA conditions: 1000 ºC for 1 sec and 10 sec. UT-MARLOWE simulations of as-implanted damage profile related the implant conditions to the as-implanted interstitial profiles and percentage amorphization. Split C-V method for mobility extraction was discussed in Section 2.3, and Medici simulations were used to estimate the strained Si layer thickness. In Section 2.4, the electron mobility was shown to degrade significantly under high implant dose and/or high thermal budget. The critical Si implant doses for mobility degradation were estimated to be in the range of 4 x 10^{12} to 3 x 10^{13} cm^{-2} for 1000 ºC 1 sec and 1000 ºC 10 sec RTA respectively. Section 2.5 discussed the materials analysis and the mechanisms of mobility degradation during processing. Based upon TEM images, Raman measurement and SIMS analysis, residual ion implantation damage was shown to be associated with the mobility degradation for devices annealed at 1000 °C for 1 sec, while implant damage enhanced Ge up-diffusion was shown to be the key mobility degradation mechanism for the MOSFETs annealed at 1000 °C for 10 sec. 2D as-implanted interstitial concentration for dopant implants in 30-nm node devices was simulated by TSuprem-4 and compared with the critical as-implanted Si interstitial concentration. 30-nm-scale strained-Si p-MOSFETs were shown to be more likely to suffer from mobility degradation than p-MOSFETs, due to halo and source/drain implants.

CHAPTER 3 Si-Ge Interdiffusivity Extraction from Experiment: Boltzmann-Matano Analysis

SiGe and Ge are widely used in today's semiconductor devices such as MOSFETs, bipolar transistors, photodetectors, and solar cells. The advantages of using SiGe and Ge in electronic devices include increased carrier mobility compared to Si, the ability to tune the bandgap for a particular application, and compatibility with Si technology. One of the biggest challenges, however, for SiGe and Ge devices is the interdiffusion that occurs at Si/SiGe interfaces, i.e. Si-Ge interdiffusion, during thermal processing. This chapter begins with background information on Si-Ge interdiffusion in Section 3.1, followed by an introduction to Boltzmann-Matano analysis for interdiffusivity extraction in Section 3.2. In Section 3.3, epitaxial structure design and growth is discussed, and in Section 3.4, the practical application of Boltzmann-Matano analysis is covered. In Section 3.5, the design of the experimental matrix is discussed. Section 3.6 shows the extracted interdiffusivity results for strained Si/relaxed SiGe structures, and Section 3.7 is the chapter summary. Although the main focus of this work is on Si-Ge interdiffusion for CMOS applications, the results are applicable to other SiGe devices as well.

3.1 Introduction to Si-Ge Interdiffusion

3.1.1 SiGe Devices and Motivation for this Work

With CMOS technology entering the nanometer regime, extensive research on SiGe-based strain and band gap engineering is being conducted for enhanced carrier transport

in strained Si, SiGe and Ge. SiGe is employed in dual-channel [8,41,42,43] and heterostructure-on-insulator (HOI) MOSFETs [44] for higher hole mobility. As the thickness of the SiGe layer decreases, interdiffusion at the Si/SiGe interface is becoming more problematic. Si-Ge interdiffusion degrades device performance by reducing strain and carrier confinement and increasing alloy scattering [45], as illustrated for strained Si n-MOSFETs in the previous chapter and for HOI devices in Figure 3-1 below.

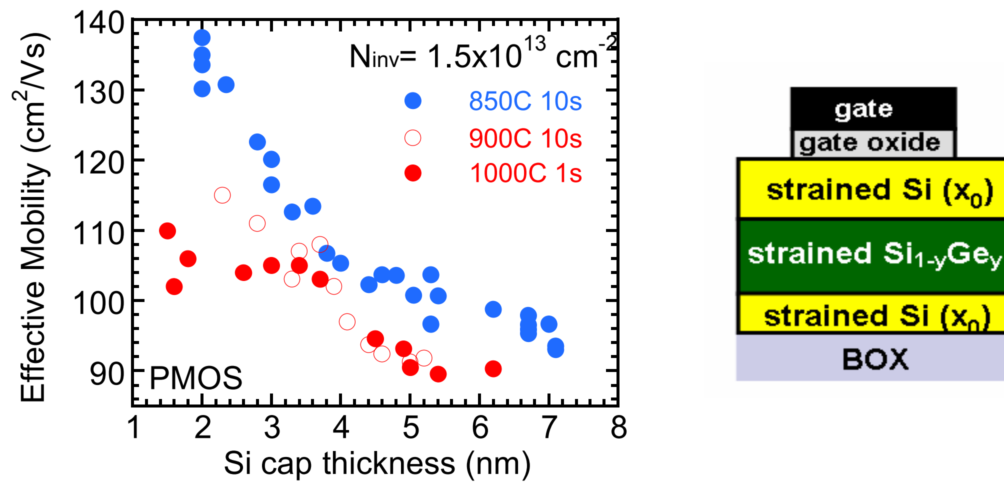

Figure 3-1 Hole mobility for different Si cap thickness for a Heterostructure in Insulator (HOI) MOSFET structure shown on the right (x0=0.24, y=0.46) for different rapid thermal annealing conditions. Figure courtesy of I. Aberg.

In Ge p-i-n photodetectors integrated on Si substrates, Si-Ge interdiffusion increases the noise level and slows down the response time significantly. Figure 3-2 shows cross-section transmission electron microscopy (XTEM) images after annealing a polysilicon-on-Ge structure. Intermixing is observed at the polysilicon/Ge interface. Another example of the influence of Si-Ge interdiffusion occurs in Ge-on-insulator fabrication. SiGe layers are normally used as etch-stop layers which are sandwiched between two Ge layers. After densification anneal, this layer can be smeared out due to interdiffusion,

causing the Ge-on-insulator fabrication to fail [46]. Therefore, it is very important to understand the Si-Ge interdiffusion behavior and its impact on SiGe and Ge device design and fabrication.

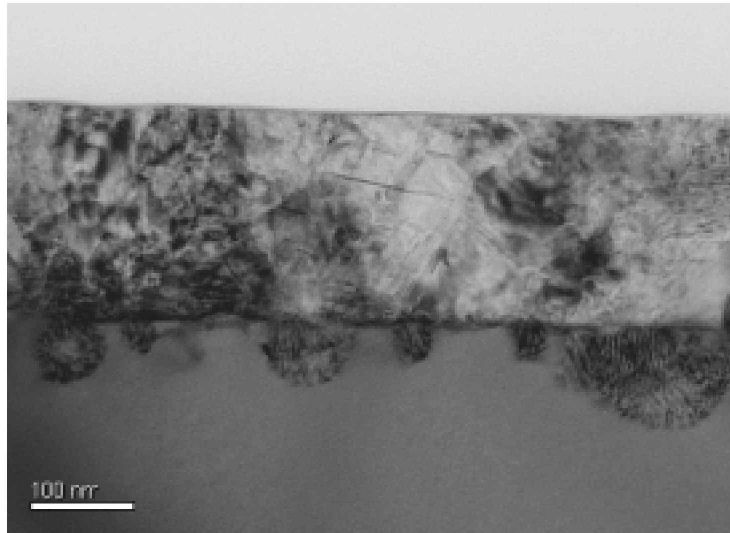

Figure 3-2 A TEM image illustrating inhomogeneous Si-Ge intermixing and interdiffusion at the polysilicon/Ge interface in the contact region of a Ge photodiode. TEM image courtesy of O. O. Olubuyide (MIT) and John Yasaitis (Analog Devices, Inc.).

3.1.2 Literature Overview

To date, Si-Ge interdiffusion has mostly been studied in special test structures which are not necessarily relevant to device structures, such as SiGe superlattices with low Ge fractions ($x_{\mathrm{Ge}} < 0.19$) grown on Si substrates [47,48], and relatively thick SiGe (x_{Ge}=0.1-0.3) grown on Si substrates [49]. There is also a significant amount of research performed on Si and Ge self-diffusion in Si and SiGe alloys [50,51]. Systematic quantification of the Si-Ge interdiffusivity in device related structures has not been conducted. Basic understanding of interdiffusion such as the dependence on Ge fraction, strain, and temperature is inadequate, and models applicable to process simulation tools are lacking.

These areas are the focus of this work.

Before further discussion on the method of interdiffusion extraction and modeling, it is important to clarify the concepts of interdiffusion, self-diffusion and dopant diffusion, as there is often confusion about these concepts. Si-Ge interdiffusion is significantly different from Si or Ge isotope self-diffusion. In self-diffusion experiments, Si or Ge isotopes (Si* or Ge*) are either implanted with a low dose into background SiGe alloys [52] or Ge*-enriched SiGe layers are epitaxially grown with surrounding layers having the same concentration of natural Ge [53]. These dilute isotopes diffuse in homogenous SiGe alloys under no Ge concentration gradient. During self-diffusion experiments, although the concentration profiles of dilute radioactive isotopes change, the host lattices stay unchanged. Self-diffusivity characterizes the diffusion of a single element in a homogenous material under no chemical potential gradient. On the other hand, Si-Ge interdiffusion at interfaces is driven by a chemical potential gradient. Both elements transport through the interface and the lattice composition changes by intermixing. In a Si/SiGe heterostructure, Si and Ge concentrations are both on the order of 1×10^{22} cm^{-3}. Therefore, Si-Ge interdiffusion should not be treated as Ge dopant diffusion in a Si lattice. Dopant diffusion is similar to self-diffusion in the sense that the host lattice doesn't change, and dopant concentration is dilute. However, dopant diffusion is driven by chemical potential gradient, which is similar to the case of interdiffusion.

Aubertine et al. used x-ray diffraction (XRD) techniques to probe interdiffusivity and the time dependence of intermixing in SiGe/Si superlattices grown on Si, and was able to measure Si-Ge interdiffusivity for Ge fractions up to 0.19 [49,50]. The use of XRD as the feedback technique limits this method to superlattice structures. It is thus not suitable for

higher Ge fractions and for application to the specific heterostructures of interest for CMOS technology. To overcome these limitations, in this work, secondary ion mass spectrometry (SIMS) is used to obtain Ge and Si profiles, and Boltzmann-Matano analysis is used to obtain the Ge fraction dependence of the Si-Ge interdiffusivity at strained Si/SiGe interfaces.

3.2 Interdiffusivity Extraction Method: Boltzmann-Matano Analysis

When interdiffusivity is concentration dependent, the shape of the diffused profile contains information about the local diffusivity. Boltzman-Matano analysis is a graphical method to extract concentration dependent interdiffusivity *D(c)* from the shape of the diffused profile in binary alloys [52,53]. It has been used widely to extract interdiffusivity in binary metal alloys and in concentration dependent dopant diffusion in Si [54, 55, 56, 57]. Figure 3-3 shows the initial condition and the diffused profile of a diffusion couple, to which Boltzmann-Matano analysis can be applied.

For this analysis to be valid, it is required that the interdiffusivity *D* can be expressed as a function of local Ge fraction x_{Ge} only. In addition the following boundary and initial conditions should be satisfied:

$$c(\eta = \infty) = C_R \qquad \text{Equation 3-1}$$

$$c(\eta = -\infty) = C_L \qquad \text{Equation 3-2}$$

where C_R and C_L are two constant concentrations on the right and left side respectively, and η is defined as:

$$\eta = \frac{z}{\sqrt{t}} \qquad \text{Equation 3-3}$$

where z is the distance from the interface, and t is the annealing time.

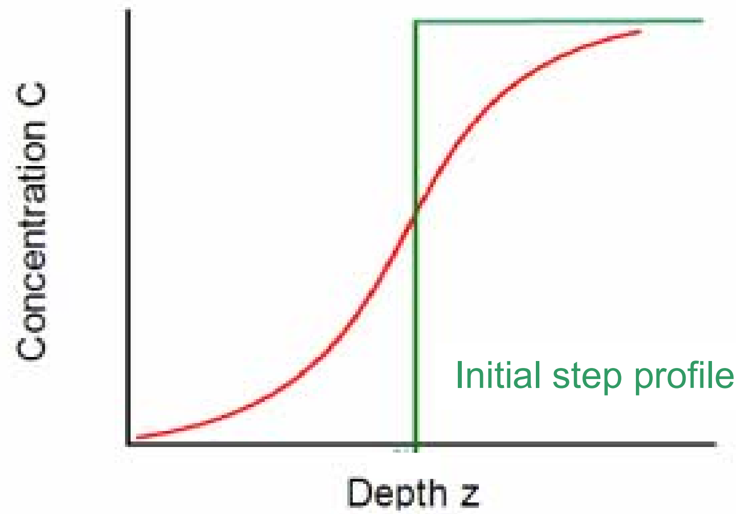

Figure 3-3 A diffusion couple with an initial step profile for Boltzmann-Matano analysis. The red curve is the diffused profile.

Translating the above boundary and initial conditions into a physical structure, Boltzman-Matano analysis requires an abrupt step concentration profile at $t = 0$, where the concentration on the left and right side of the interface are C_L and C_R respectively, and ideally both sides should be infinitely long. In this work, the Boltzman-Matano structures were designed to be epitaxial strained Si on relaxed $Si_{1-x0}Ge_{x0}$ heterostructures with $C_L = 0$ and $C_R = x_0$. The $Si/Si_{1-x0}Ge_{x0}$ interfaces are grown to be very abrupt. According to XTEM analysis (as shown in the image of an as-grown strained Si/SiGe structure in Figure 2-15) the transition region is on the order of a few monolayers. The ion beam mixing associated with SIMS broadens the measured profile, depending upon the details of the SIMS analysis conditions, so that the transition region as measured by SIMS may appear to be on the order of 30 to 50 A. The SIMS broadening must be kept in mind in performing the diffusion analysis. The thickness of the strained Si layer is 100-160 A depending on the Ge fraction x_0, and the thickness of the relaxed $Si_{1-x0}Ge_{x0}$ layer is

typically 0.75 um (with a relaxed, graded-composition SiGe layer underneath this $Si_{1-x0}Ge_{x0}$ layer). Annealing conditions were carefully designed such that the diffusion fronts would not reach the Si surface. As a result, under these conditions the diffusion couple can be treated as if each side is infinitely long. Therefore, the initial and boundary conditions are satisfied.

It is expected that at a certain temperature, interdiffusivity is a function of local Ge fraction x_{Ge}, local strain σ, and material quality. Based on Mooney *et al.*, a high density of threading defects (10^8 cm^{-2}) has a negligible impact on the interdiffusion at Si/SiGe interfaces [58]. The dislocation densities of our as-grown epitaxial heterostructures are on the order of 10^5 cm^{-2}. Therefore, in this initial study, it is reasonable to neglect the effect of threading dislocations. The interdiffusivity can then be expressed as a function of only the local Ge fraction, x_{Ge} and local strain, ε:

$$D = func \quad (x_{Ge}, \varepsilon) \qquad \text{Equation 3-4}$$

It should be noted that the effect of dislocation density was also investigated in this study (see Section 4.4.2 in Chapter 4), which shows that a threading dislocation density of about 1 x 10^7 cm^{-2} has little impact on the interdiffusion at the $Si/Si_{0.7}Ge_{0.3}$ interface.

Theoretically, as long as the local strain can be expressed as a function of x_{Ge} or is constant, such as the case where strain is fully relaxed, the Boltzmann-Matano analysis assumption is satisfied. Since the broadening of the Ge profile is limited in these experiments, it is reasonable to assume that the local strain, ε is proportional to the difference between the local Ge fraction, x_{Ge} and the substrate Ge fraction, x_0:

$$\varepsilon = 0.042 * (x_0 - x_{Ge}) \qquad \text{Equation 3-5}$$

It should be noted that this is an assumption that is difficult to verify directly in the case of the Boltzmann-Matano structures, since probing the strain in the interdiffused region is difficult. However, this assumption is supported by experiments discussed in Chapter 4, in which it was verified that for thin $Si_{1-y}Ge_y$ layers for which the Ge fraction drops due to outdiffusion into surrounding Si layers, the resulting $Si_{1-y}Ge_y$ layer appears to remain strained to the relaxed $Si_{1-x0}Ge_{x0}$ substrate. These results were obtained by Raman analysis (see for example Figure 4-7). Thus, it seems reasonable to assume that in the thin intermixed regions of the Boltzmann-Matano structures, the local strain is given by Equation 3-5 above.

Based on the above analysis, at a given temperature the interdiffusivity, D can be expressed as a function of x_{Ge} only, which is the first assumption of the Boltzman-Matano analysis. From the above analysis, the application of Boltzman-Matano analysis to these structures appears to be justified.

The analytical expression for the diffusivity extracted from Boltzmann-Matano analysis is given by:

$$D(C') = -\frac{1}{2t}\left(\frac{dz}{dC}\right)\bigg|_{C'} \bullet \int_{C_L}^{C'} (z - z_M)\, dC \qquad \text{Equation 3-6}$$

where $D(C)$ is the interdiffusivity at Ge concentration C, t is the annealing time, z is the depth, $C(z)$ is the concentration vs. depth profile, and z_M is the position of the Matano plane.

The definition for Matano plane, z_M is the position that satisfies the following condition:

$$\int_{C_L}^{C_R} (z - z_M)\, \mathrm{d}C = 0 \qquad \text{Equation 3-7}$$

Graphically, in a plot of depth versus concentration, shown in Figure 3-4, z_M is the

reference point, where the integral of depth over concentration for the whole concentration range is zero. Note that the position z_M is normally not the initial interface at z=0 due to the different vacancy flux from both sides. The details of the Boltzmann-Matano analysis can be found handbooks on diffusion, such as Ref [59].

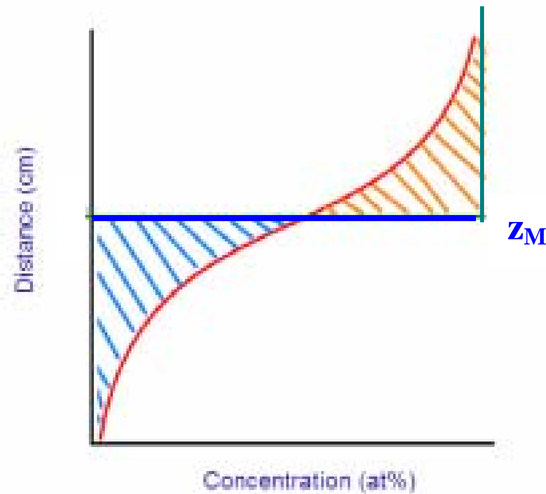

Figure 3-4 Graphical illustration of the Matano plane z_M. The areas under the concentration curve on either side of z_M are equal. Figure from Ron Harrington's online course notes at Rensselaer Polytechnic Institute, Troy, NY.

3.3 Epitaxial Structure Design and Growth

In this work, two types of structures are epitaxially grown, annealed and analyzed. The first type of sample is referred to as a "step" structure for Boltzman-Matano analysis as shown in Figure 3-5, where a strained Si layer is epitaxially grown on top of relaxed $Si_{1-x0}Ge_{x0}$ layer. The notation for these structures includes the Ge percentage of the relaxed $Si_{1-x0}Ge_{x0}$ layer. For example, "BM20" refers to a strained Si/relaxed $Si_{0.80}Ge_{0.20}$ structure. Three "step" structures were grown for this study, referred to as BM20, BM40, and BM60.

Figure 3-5 A generic "step" structure

The second type of structure is referred to as a "peak and step" structure, which is illustrated in Figure 3-6, and consists of strained Si/$Si_{1-y}Ge_y$/strained Si on a relaxed $Si_{1-x0}Ge_{x0}$ virtual substrate. The term "peak" refers to the $Si_{1-y}Ge_y$ layer sandwiched between two strained Si layers. The purpose of using these structures is three-fold. First, the top three layers of these structures and their strain status are the same as in HOI structures, which makes them suitable to emulate Si-Ge interdiffusion in HOI devices. Secondly, the diffusion of the peaks can be used to evaluate and refine the interdiffusivity extracted from the diffused steps. Thirdly, the "peak and step" structures enable decoupling of the strain and Ge concentration dependence of Si-Ge interdiffusion, by varying the strain in the peaks by using different combinations of x_0 and y.

The notation for the "peak and step" structures (strained Si/$Si_{1-y}Ge_y$/strained Si on relaxed $Si_{1-x0}Ge_{x0}$ structures) is "100*y/100*x_0", where y and x_0 refer to the Ge fractions of the peak and step respectively. For example, structure 56/31 refers to a strained Si/$Si_{0.44}Ge_{0.56}$/strained Si on relaxed $Si_{0.69}Ge_{0.31}$ structure. Figure 3-6 shows the generic structure of y/x_0 and a 45/45 epitaxial structure. The "peak and step" structures in this

study include three groups: 56/56, 45/45 and 30/30, where the peak layers are nominally unstrained; 56/31, 45/15 and 30/00, where the peak layers are under compressive strain of about -1%; and 30/56, where the peak layer is under tensile strain of about 1%.

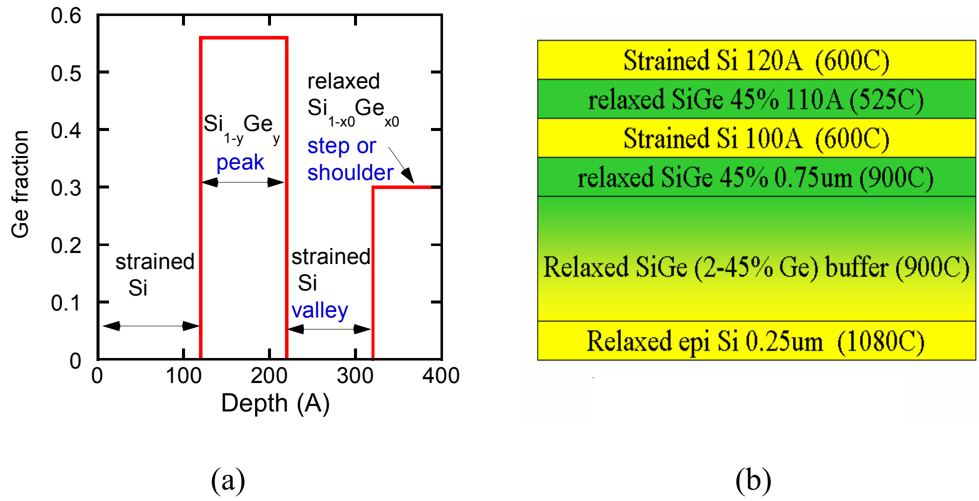

(a) (b)

Figure 3-6 (a) The Ge profile of a generic "peak and step" structure y/x_0. (b) A 45/45 "peak and step" epitaxial structure. The growth temperatures are in the parentheses. The term "valley" refers to the strained Si layer directly on top of the relaxed $Si_{1-x0}Ge_{x0}$ layer since it is surrounded by two SiGe layers. The term "shoulder" refers to the diffused "step".

All the structures in this study were epitaxially grown on <100> Czochralzki p-type Si wafers in an Applied Materials "Epi Centura" system. The relaxed $Si_{1-x0}Ge_{x0}$ layers were grown at 900 ºC, and the strained Si layers at 600 ºC. The $Si_{1-y}Ge_y$ layers were grown at 525º C for y = 0.56 and 0.45, and 600ºC for y = 0.3. Figure 3-6 (b) shows the epitaxial structure and growth temperatures for a 45/45 "peak and step" structure. The thicknesses of the strained Si and $Si_{1-y}Ge_y$ layers are in the range of 100 to 140 A. The epitaxial layers are undoped.

Annealing was performed in a furnace (tube-B3 in TRL) in N_2 ambient. The annealing times range from 30 min to 80 hours depending on the annealing temperature. The use of furnace annealing instead of rapid thermal annealing (RTA) is motivated by

the need for very accurate temperature control and calibration, which is afforded by a furnace but not by RTA apparatus, particularly when annealing wafers with SiGe heterostructures. Such layers may impact light absorption in the RTA and lead to uncontrolled temperature variations. Temperature errors of 50 to 100ºC are not uncommon during RTA, making controlled diffusion experiments very difficult. An example furnace annealing temperature profile is shown in Appendix D for reference.

3.4 Practical Application of Boltzmann-Matano analysis

3.4.1 Initial Verification and Example of Boltzmann-Matano Analysis

Boltzmann-Matano analysis was performed on the SIMS profiles for the annealed samples. An example of the Matlab code used for the analysis is given in Appendix E. The initial tests of the Boltzmann-Matano analysis were performed using BM20 and BM40 structures annealed at 920º C for an hour. The as-grown and annealed Ge profiles were measured by SIMS (Figure 3-7). Both as-grown structures have abrupt interfaces strained Si/$Si_{1-x0}Ge_{x0}$ interfaces, which is a good approximation of the ideal step profile in Boltzmann-Matano analysis. The effect of the initial profiles is addressed in Appendix F. The annealing conditions were designed so that the diffusion fronts remain within the strained Si layers, and therefore, the strained Si/relaxed $Si_{1-x0}Ge_{x0}$ structures can be treated as infinitely long diffusion couples.

Figure 3-8 shows the interdiffusivity extracted from SIMS profiles of BM20 and BM40 structures (Figure 3-7) using Boltzmann-Matano analysis. It can be seen that the interdiffusivity depends exponentially on Ge fraction. Therefore, the interdiffusion at higher Ge fractions dominates the interdiffusion process. The two sets of data overlap except for Ge fractions, x_{Ge} below 0.1, where the interdiffusivity extracted from BM40 is

larger than that extracted from BM20. This effect together with z_M position effect on extracted interdiffusivity is addressed in Appendix G.

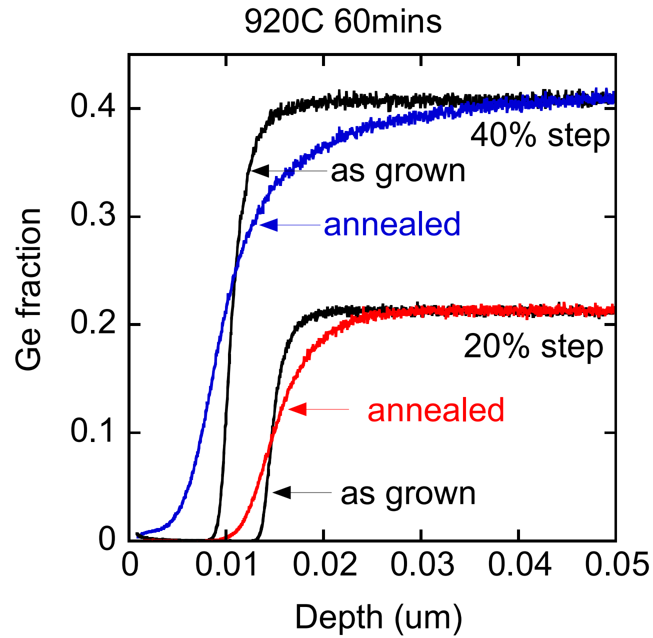

Figure 3-7 Ge SIMS profiles of BM20 and BM40 structures before and after 920º C 60 min inert annealing.

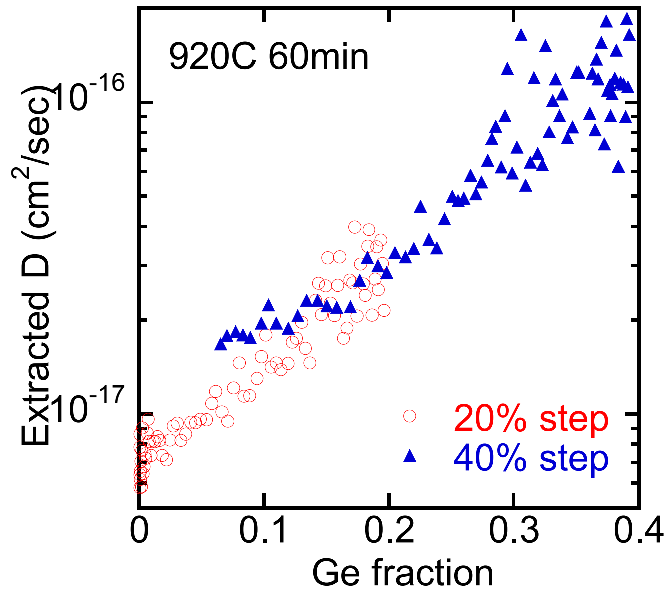

Figure 3-8 Extracted interdiffusivity from the application of Boltzmann-Matano analysis to SIMS profiles for BM20 and BM40 structures.

3.4.2 Pseudo-Boltzmann-Matano analysis

A modified Boltzmann-Matano analysis was performed on the diffused steps in "peak and step" structures. The analysis was modified to account for the fact that in "peak and step" structures, the valley (the strained Si layer directly on top of the relaxed $Si_{1-x0}Ge_{x0}$ layer) sees interdiffusion from both sides. Therefore, the Ge diffusion fronts from both sides tend to merge in the valley, invalidating the infinite length condition. The annealing conditions were designed such that the only a few atomic percent Ge diffused into the valleys after annealing, and thus a modified Boltzmann-Matano method was applied, as described in this section.

Figure 3-9 shows typical as-grown and diffused Ge profiles for a "peak and step" structure measured by SIMS. The structure is 56/56 and the annealing condition is 800 °C for 13 hours. It can be seen that the valley has filled to 4 atomic % Ge, by interdiffusion from both sides. However, the interdiffusivity is a strong function of Ge fraction and most interdiffusion happens in the high Ge fraction region. Therefore, although the diffusion front from the step merged with that from the peak by a small amount, the interdiffusion at higher Ge fractions should not be affected significantly, and interdiffusivity information from the diffused profiles at high Ge fractions can be obtained within acceptable error. The pseudo-Boltzmann-Matano analysis works as follows: a Ge profile that emulates the diffusion front from the relaxed $Si_{1-x0}Ge_{x0}$ step is generated (crosses in Figure 3-9), and Boltzmann-Matano analysis is performed on the shoulder profile with the generated diffusion front. This pseudo-Boltzmann-Matano analysis was applied to structures 45/45 and 56/56.

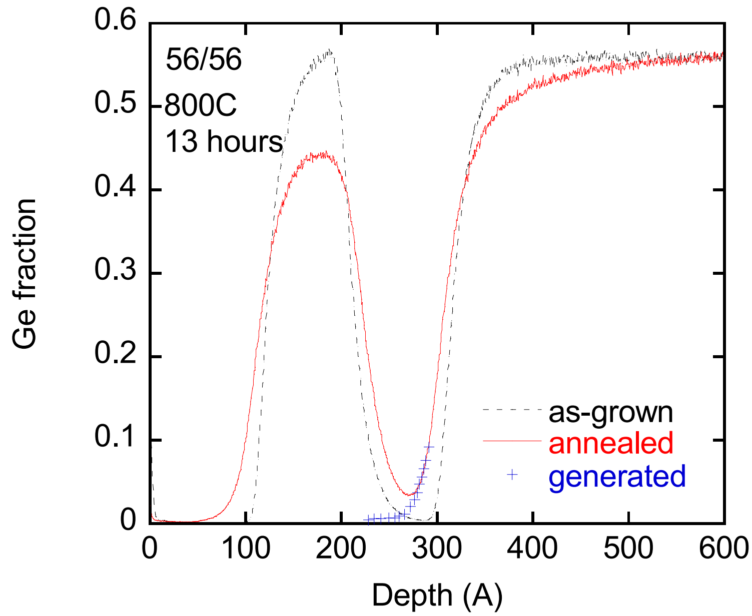

Figure 3-9 Ge SIMS profiles and the generated foot part of the profile for 56/56 structure that illustrates the profile used in the pseudo-Boltzmann-Matano analysis.

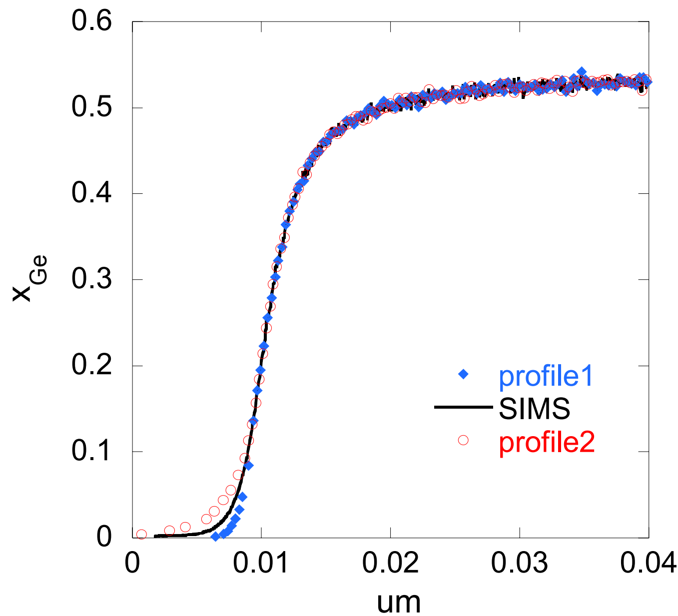

Figure 3-10 SIMS profile with two generated profiles in the low-Ge-fraction region, for a sample annealed at 880° C for 30 min.

Errors that were introduced by the manually generating diffusion fronts (the foot part of a diffused Ge profile) in the pseudo-Boltzmann-Matano analysis were checked by

comparing the extracted interdiffusivity from a "step" structure with different generated fronts. Figure 3-10 shows the annealed SIMS profile of sample BM53 along with two curves with generated profiles that differ somewhat in the low-Ge-fraction region (x<0.15), but are identical for Ge fractions above 0.15. The corresponding interdiffusivity curves extracted from Boltzmann-Matano analysis are shown in Figure 3-11. It can be seen that the generated profile does introduce errors for low Ge fractions, but that the errors are negligible for $x_{Ge} > 0.20$. Therefore, the pseudo-Boltzmann-Matano method can be applied to "peak and step" structures to extract interdiffusivity for $x_{Ge} > 0.2$.

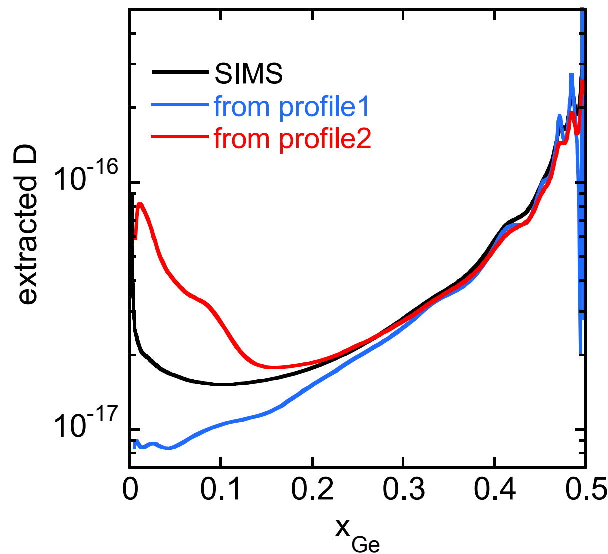

Figure 3-11 Interdiffusivity extracted from the three profiles shown in Figure 3-10.

3.4.3 Error from SIMS Broadening Effect

SIMS tends to broaden steep interfaces as seen in Figure 3-12 for several as-grown Ge profiles. The measured SIMS profile is actually a convolution of the true concentration profile and the SIMS response function. However, it is difficult to decouple these two factors, since the SIMS response function depends on the SIMS profiling ion

beam energy and the material composition. The true profile is expected to be steeper than the SIMS data. In “peak and step” structures, there are strained Si layers sandwiched in between two SiGe layers, forming “valley” regions. SIMS broadening effects tend to artificially fill-up the valley. As seen in Figure 3-9, even the as-grown 56/56 structure has a partly-filled valley.

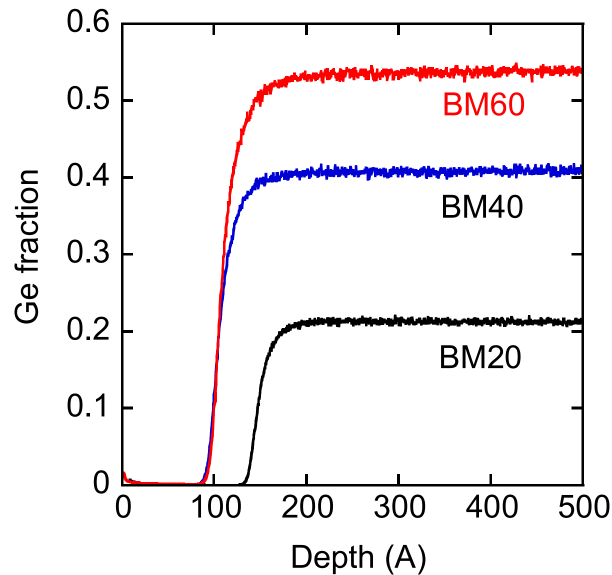

Figure 3-12 SIMS profiles for as-grown BM20, BM40 and BM60 structures. The leading edges and rounded shoulders are due to SIMS broadening effects.

There are ways to minimize the effects of SIMS broadening on the extracted diffusivity. The annealing time can be chosen to be as long as possible, so that the measured annealed profile is not significantly impacted by SIMS broadening. However, in order to satisfy the infinite medium condition, the overall amount of diffusion broadening is limited by the thickness of the strained Si layer. The thickness of the strained Si layer is limited by the critical thickness for dislocation formation during strained layer growth, as discussed in Chapter 2. In practice, it was found that a strained Si layer thickness of about twice the equilibrium critical thickness is appropriate.

Since SIMS broadening is expected to have the largest impact on the profile slope near the foot of the profile, one may surmise that the diffusivity extracted by Boltzmann-Matano analysis from that region is subject to the greatest error. Thus, given several samples with different step heights, with diffusivity extracted from Boltzmann-Matano analysis, one expects greater accuracy in the diffusivity extracted from a BM20 sample than from BM40 or BM60 structures, in the low-Ge-fraction range, x_{Ge} < 20%. Figure 3-13 illustrates this effect, with the diffusivity extracted from BM40 apparently overestimated compared to that extracted from BM20, in the low-Ge-fraction regime. Another possible reason for this discrepancy is that the real interdiffusivity in the low Ge-fraction-regime is indeed different for these two structures. While this remains a possible interpretation, restricting the region of validity of the extracted diffusivity data as illustrated in Figure 4-1 yields a universal model that fits the major features of Si-Ge interdiffusion over a wide range of sample compositions and conditions, as discussed in Chapter 4. Nevertheless, it is important to keep in mind the possibility that more subtle effects than can be captured by the present model may be taking place.

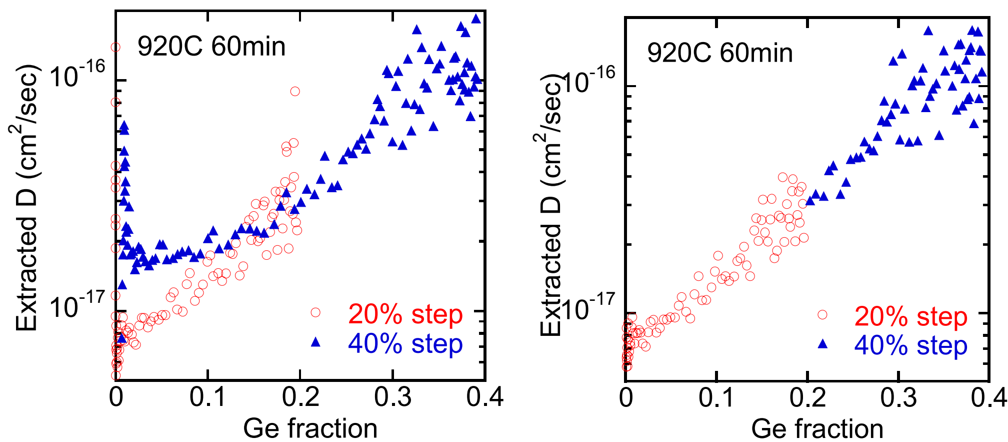

Figure 3-13 (a) unprocessed extracted interdiffusivity from SIMS profiles of BM20 and BM40 structures in Figure 3-7, and (b) processed interdiffusivity with the low x_{Ge} data blocked for the BM40 structure.

3.5 Experiment Matrix Design

In order to investigate the interdiffusivity as a function of Ge fraction, temperature and strain status, an experiment matrix was designed as shown in Table 3-1. The experimental design process started with the knowledge gained from the initial data extracted from BM20 and BM40. In order to extract diffusivity from SIMS, the Ge peak drop for samples in Table 3-2 was designed to be 7 to 12 atomic %, which is large enough to be immune to SIMS measurement error of about 2 atomic %. For structures 30/56, 30/30 and 30/00 in Table 3-3, the peak drop of the $Si_{0.70}Ge_{0.30}$ layer was designed to be lower, 4 to 7 atomic %. This is to prevent too much diffusion in structure 30/56 from the relaxed $Si_{0.44}Ge_{0.56}$ shoulder into the adjacent strained Si layer, which can affect the diffusion of the $Si_{0.70}Ge_{0.30}$ peak. Table 3-1 shows all the samples and anneals performed for "step" structures, and Table 3-2 shows samples for "peak and step" structures. Table 3-3 shows samples with 30% peak (30/60, 30/30 and 30/00) under as-grown tensile, relaxed and compressive strain. Since a large number of samples in this group were sent for both SIMS and Raman measurement, that information is included in the table.

Structure/ anneals	BM20	BM30	BM40	BM60
As-grown	**BM202**		**BM402**	**BM602** **BM60F**
Spare unannealed samples	BM20J, BM20M, BM20N, BM20P, BM20Q, BM202 2118BM20	BM300 2120BM30	BM40F, BM40H, BM40I , BM40J, BM40K, BM40L BM402 2124BM40	BM60F, BM60K, BM600, BM602
800C	**BM20K-- 80hr**		BM40G – 13hr	BM60L – 13hr
840C	**BM20L—23hr**			**BM60H – 4hr 34min,** BM60P, 60Q, 60R –30min
850C 5hr	BM20E		BM40E	
880C 30min				**BM60B** (aka:BM53), BM60M, 60N
880C 90min				**BM60E** BM60G **BM60I**
880C 2hr	BM20C		BM40C	BM60D
880C, other	**BM20F--4hr 11mins**			BM60J –60min
920C 30min	BM20D		BM40D	
920C 60min	**BM20A**	BM30A	**BM40A** (aka BMA4)	

Table 3-1 Sample matrix for "step" structures annealed at different temperatures and times. Sample in bold letters are those with SIMS profiles available.

Structure/anneals	60/60	60/30	45/45	45/15
As-grown	**71, 71E**	**72, 72E**	**75, 75E**	**76, 76E**
770C, 7hrs		**72e, 8% peak drop**		**76e2, 7% peak drop**
800C, 40mins	**71B, little diffusion**	**72B,** **6% peak drop** 72a for Raman	75B, too little diffusion	76B, estimate 2.5% drop, no SIMS
800C, 120mins	**71C,** **2-3% peak drop**	**72C,** **10% peak drop** 72b for Raman	**75C,** **1% peak drop**	**76C,** **7% peak drop**
800C, 13hrs	**71e, 12% peak drop**		**75e, 7% peak drop**	
840C, 30mins	**71F,** **8% peak drop** **71f, 6% drop**	**72F, 10.2% peak drop** 72dd for Raman	**75e2, 3.5% peak drop**	**76F and 76G, about 9% peak drop**
840C, 3hrs			**75F, 8.5% drop**	
880C, 30mins	**71A, 13% drop** 71b for Raman	72D annealed much diffusion, no SIMS 72d for Raman	**75D, 9% drop**	76D, much diffusion, no SIMS

Table 3-2 Sample matrix for "peak and step" structures annealed at different temperatures and times. Sample in bold letters are those with SIMS profiles available.

Structure/anneals	30/60	30/30	30/00	BM60
Spare unannealed samples	94H, 94N			
As-grown for SIMS	**94C -- SIMS**	**95B—SIMS**	**96B—SIMS**	BM60F—SIMS
As-grown for Raman	94E -- Raman	95D--Raman	96D--Raman	
880C, 90min for SIMS	**94B--SIMS**	**95A—SIMS**	**96A—SIMS**	**BM60E—SIMS back**
880C, 90min for Raman	94D--Raman	95C--Raman	96C--Raman	BM60G
880C, 2hrs	**94A--SIMS**			BM60D
840C 30mins	94R, 94S, 94T, 94U, 94cc			BM60P, BM60Q, BM60R
880C 30mins	94M, 94N, 94P, 94Q			BM60M, BM60N
880C, 90min	94F, 94G, 94I, 94J, 94K1,94K2,94L1, 94L2 --- etch top Si layer of 94K1 and 94L2, 94K2; 94L1 for XTEM			BM60I

Table 3-3 Sample matrix for "peak and step" structures with 30% peak annealed at different temperatures and times. Sample in bold letters are those with SIMS profiles available.

3.6 Summary of Extracted Interdiffusivity

After Boltzman-Matano analysis of "step" structures (BM20, BM40, BM60) and pseudo-Boltzman-Matano analysis of "peak and step" structures (56/56 and 45/45), all extracted Si-Ge interdiffusivity data (in temperature range 800-920 ºC and Ge fraction

range 0-0.5) are summarized in Figure 3-14. The interdiffusivity data was extracted from samples with different step heights, which are indicated by different symbols. Figure 3-14 confirms our observation in Figure 3-8 that the Si-Ge interdiffusivity depends exponentially on local Ge fraction for all the temperatures in this work. Another important observation from Figure 3-14 is that Si-Ge interdiffusivity curves at different temperatures are evenly spaced throughout the Ge fraction range investigated, which indicates that the activation energy in this temperature range is relatively independent of Ge fraction.

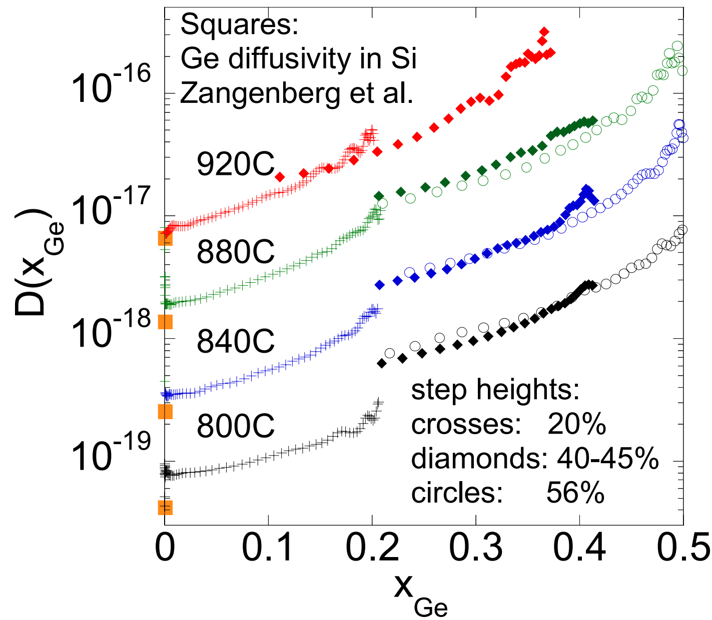

Figure 3-14 Interdiffusivity for strained Si/relaxed SiGe structures extracted by Boltzmann-Matano analysis and pseudo-Boltzmann-Matano analysis. These data were extracted from samples with different step heights. Crosses are interdiffusivity data extracted from BM20 structures; diamonds are data extracted from 40-45% steps in BM40 and 45/45 structures; and circles are from 56% steps in BM56 and 56/56 structures.

The Ge tracer diffusivity in Si should agree with the limiting case of Si-Ge interdiffusivity when $x_{Ge} = 0$. Therefore, Ge diffusivity in Si calculated based on Ref. [51] is also shown in Figure 3-14 (squares) for comparison. The interdiffusivity results at $x_{Ge} =$

0 extracted by Boltzman-Matano analysis from BM20 structures agree well with the Ge diffusion measurements in [51].

3.7 Chapter Summary

In this chapter, an introduction to Si-Ge interdiffusion was discussed. The Boltzmann-Matano interdiffusivity extraction technique and the experimental design were introduced. It was shown that there is a region of validity for the application of Boltzmann-Matano analysis to strained Si/SiGe structures, which takes into account critical thickness constraints and the limitations associated with SIMS broadening. In order to obtain accurate diffusivity values, these constraints were considered when designing the sample epitaxial layer structures and the diffusion conditions (i.e. the amount of profile motion). The results for the Si-Ge interdiffusivity extracted from this Boltzmann-Matano analysis indicate an exponential dependence of the interdiffusivity on Ge fraction. In the next chapter, additional experiments, material analysis, and modeling and simulation of these profiles in a process simulator will be discussed.

CHAPTER 4 Si-Ge Interdiffusion and Its Impact on Heterostructure MOSFET Design and Process Integration

After the introduction to the Boltzmann-Matano method and the initial interdiffusivity results presented in Chapter 3, the use of the extracted interdiffusivity model in the process simulator, TSUPREM-4™ [40], and applications of the model will be discussed in this chapter. This chapter begins with a brief review of the SiGe interdiffusivity results from the Boltzmann-Matano analysis in Section 4.1, followed by the interdiffusivity results and modeling for strained Si/compressive SiGe/strained Si structures in Section 4.2. In Section 4.3, SiGe interdiffusion mechanisms are discussed and in the Section 4.4, surrounding layer and threading dislocation effects are covered. The "surrounding layer" effect refers to the impact of changing the composition of the strained Si layers on either side of the SiGe layer, by using a SiGe alloy layer in place of the strained Si layers. Section 4.5 gives a few examples of the application of this work and its impact on technology.

4.1 Interdiffusion for strained Si/relaxed SiGe structures

4.1.1 Summary of Extracted Interdiffusivity

The results of the Boltzmann-Matano analysis discussed in Chapter 3 (e.g. Figure 3-14) are repeated here for reference in Figure 4-1 (a). The interdiffusivity data was extracted from samples with different step heights (x_0), which are indicated by different symbols. The interdiffusivity in low Ge fraction ($x_{Ge} < 0.2$) region extracted from samples with high step heights (x_0 = 40, 45 and 56%) are not shown in Figure 4-1 (a) for clarity.

Figure 3-14 (a) confirms our observation in Figure 3-8 that the Si-Ge interdiffusivity depends exponentially on local Ge fraction for all the temperatures in this work. Another important observation from Figure 3-14(a) is that Si-Ge interdiffusivity curves at different temperatures are evenly spaced throughout the Ge fraction range investigated, which indicates that the activation energy in this temperature range is relatively independent of Ge fraction. Figure 4-1 (b) shows the data for samples with high step heights (x_0 = 40, 45 and 56%). In Figure 4-1 (b) and (c), some interdiffusivity curves are obtained by pseudo-Boltzmann-Matano analysis. Therefore, the interdiffusivity data in the generated foot regions are not shown, as they are by-products of the pseudo-Boltzmann-Matano analysis, and have no physical meaning (see Figure 3-9, 3-10 and 3-11 for details). As seen in Figure 4-1 (b), in the higher x_{Ge} range ($x_{Ge} > x_0 /2$), interdiffusivity is relatively independent of the substrate Ge fraction x_0, while in the lower x_{Ge} range ($x_{Ge} < x_0 /2$), the interdiffusivity extracted from different step heights tends to be more scattered.

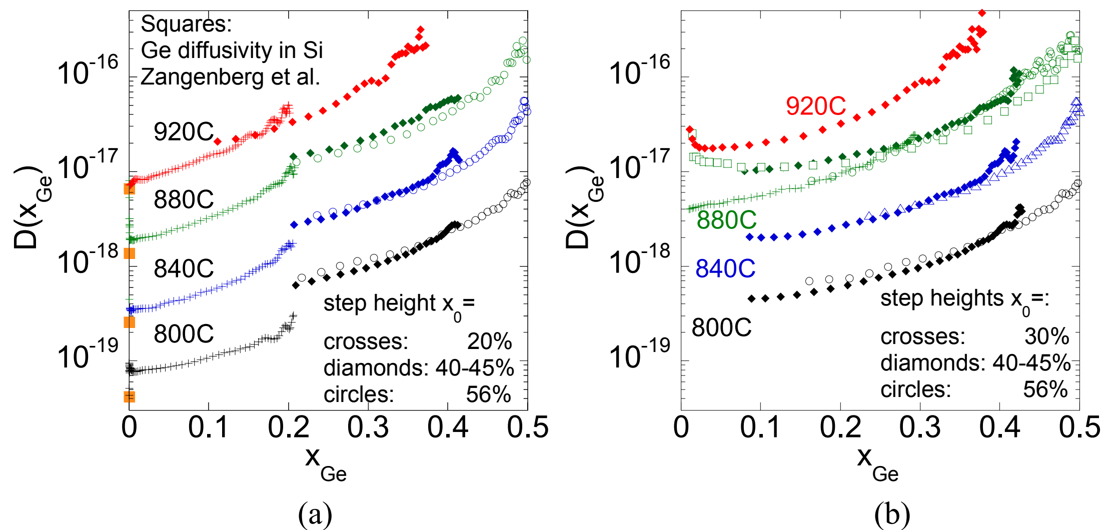

(a) (b)

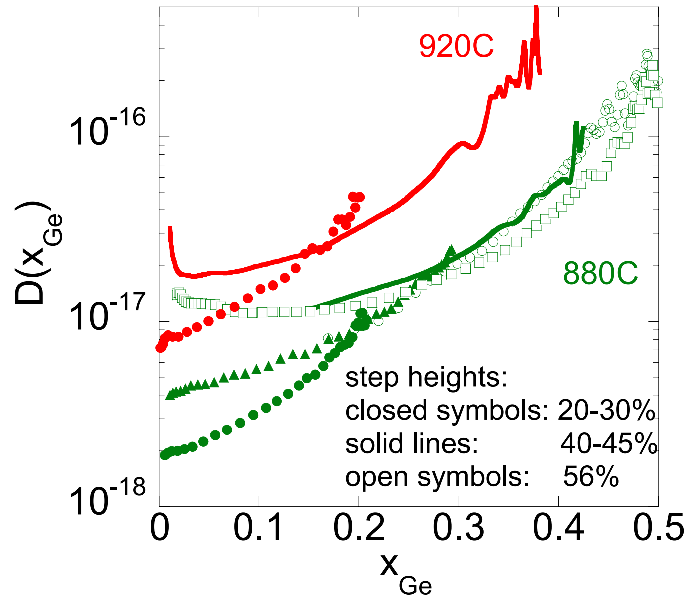

(c)

Figure 4-1 Interdiffusivity for strained Si/relaxed SiGe structures extracted by Boltzmann-Matano analysis and pseudo-Boltzmann-Matano analysis. These data were extracted from samples with different x_0. (a) The interdiffusivity data for all samples. Data in low Ge fraction ($x_{Ge} < 0.2$) region for samples with $x_0 > 0.4$ not shown for clarity. (b) The interdiffusivity data for samples with $x_0 > 0.4$. (c) Interdiffusivity curves extracted from samples with different x_0 for 880 and 920 ºC. In the lower x_{Ge} range ($x_{Ge} < x_0 /2$), interdiffusivity shows dependence on x_0. In (b) and (c), the interdiffusivity extracted from the generated foot part of the profiles using pseudo-Boltzmann-Matano analysis is not shown.

Figure 4-1(c) compares the interdiffusivity curves for samples with different step heights annealed at 880 and 920 ºC. Data for 800 and 840 ºC are not shown for clarity. The interdiffusivity in low x_{Ge} range ($x_{Ge} < x_0 /2$) is referred to as the tail region of the interdiffusivity curve. The interdiffusivities in high x_{Ge} range are in good agreement, while data in the tail region show a dependence upon the substrate Ge fraction, x_0. Samples on higher x_0 tend to have higher diffusivity in the tail region. This dependence of the tail diffusivity on x_0 is very similar to SIMS broadening as discussed in Section 3.4.3. Another possible explanation for this effect is related to enhanced diffusion through misfit dislocations. Higher x_0 implies higher tensile stress at low x_{Ge}, and a higher probability of relaxation by misfit dislocations. A third possibility is strain status change

during annealing. If the high tensile strain at low x_{Ge} relaxes but the lower tensile strain in high x_{Ge} range doesn't relax at the same time, then the coherent assumption in Equation 3-5 no longer holds. This would introduce errors in Boltzmann-Matano analysis if the interdiffusivity under tensile strain is different from that under relaxed strain. In Section 4.1.4 and 4.1.5, tensile strain impact is discussed, and the effect from tensile strain is considered to be minor.

Since the interdiffusion is strongly dependent on x_{Ge}, the diffusivity in the tail of the Ge profiles has little impact on diffusion near the peak and shoulder of the profiles. As seen in Figure 3-9, 3-10 and 3-11 in Section 3.4.2 on pseudo-Boltzmann-Matano analysis, the diffusivity extracted from the foot regions of Ge profiles can be quite different, and yet the diffused profiles agree well except for the foot regions, the as long as the diffusivity in high x_{Ge} is the same. In other words, interdiffusivity in high x_{Ge} range captures the main profile motion, and interdiffusivity in the low x_{Ge} range can be treated as a second order effect in interdiffusivity modeling. Taking that into account, it is reasonable to remove the tail diffusivity for samples with high x_0 and keep the data at high x_{Ge} as shown in Figure 4-1 (a), which captures the major Ge profile motion in the high x_{Ge} regime.

4.1.2 Refining the Interdiffusivity Results

The above interdiffusivity curves were extracted from diffused steps by Boltzmann-Matano and pseudo-Boltzmann-Matano analysis. As mentioned before, one of the purposes of the "peak and step" structures was to provide an experimental method to evaluate and refine the interdiffusivity results. The samples used for refinement are structure 56/56 and 45/45, as the as-grown peaks in 56/56 and 45/45 are designed to have

the same Ge fraction as the steps. Therefore, the diffusion of the peaks and shoulders are both taking place at strained Si/relaxed SiGe interfaces, enabling the peak diffusion to serve as an on-chip calibration of the interdiffusivity extracted from the shoulder diffusion. For other structures such as 56/31 and 30/56, the SiGe peak layers are designed to be under biaxial compressive or tensile stress. Therefore, the peak diffusion in these structures may be different from the shoulder diffusion, and thus not suitable for diffusivity calibration.

The refinement process is described as follows. First, interdiffusivity results from Boltzmann-Matano analysis are approximated analytically using the “polyfit” function in Matlab. This analytical expression is used as the diffusivity to simulate the Ge diffusion in the TSUPREM-4™ [40] user-specified equation interface. Finally, the input interdiffusivity expression is modeled based on the data in Figure 4-1 (a) and fine-tuned such that it generates a good fit to the diffused Ge profiles measured by SIMS. The details of the refinement are explained below.

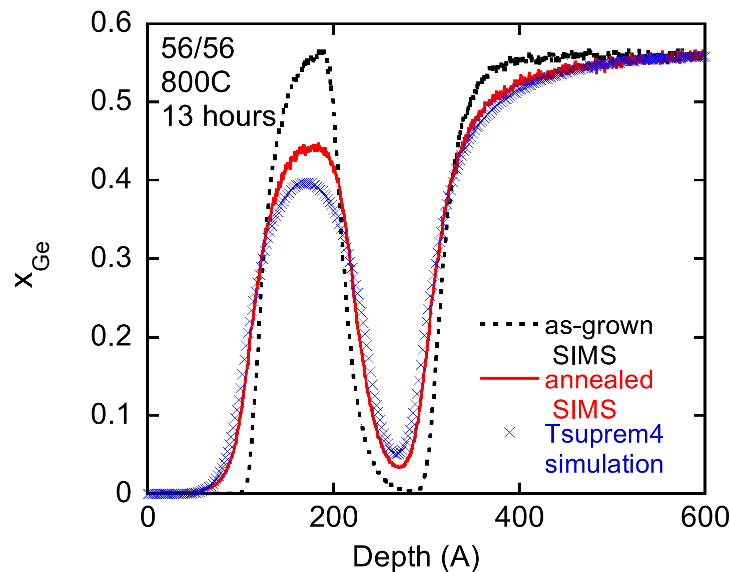

Figure 4-2 As-grown and annealed SIMS profiles for structure 56/56 and the TSUPREM-4 simulation using the interdiffusivity data in Figure 3-14 (b).

Figure 4-2 shows the as-grown and annealed SIMS profiles for structure 56/56. The crosses show the diffused profile simulated by TSUPREM-4 using the extracted interdiffusivity results in Figure 4-1 (b). The starting profile for this simulation is the as-grown SIMS profile. The TSUPREM-4 simulated profile is in reasonable agreement with the annealed shoulder profile, which shows self-consistency of Boltzmann-Matano analysis. Since the ideal initial condition for Boltzmann-Matano analysis is a perfect step, using the SIMS profile of the as-grown sample as the initial profile slightly overestimates the diffusion in the simulated post-annealed shoulder profile.

Focusing now on the interdiffusion of the 56% SiGe peak, the total peak drop is 12 atomic %, and the simulation overestimates the peak drop by 4.5 atomic %. This suggests that the interdiffusivity extracted from the shoulder, which is the interdiffusivity input to the TSUPREM-4 simulator, is faster than the interdiffusivity of the peak. This overestimation may be a result of the SIMS broadening effects at the strained Si/relaxed SiGe interface (i.e. the shoulder). Since Boltzmann-Matano analysis is sensitive to the local slope of the SIMS profile, any SIMS broadening will result in an overestimation of the interdiffusivity extracted from the shoulder profile. At the same time, the thickness of the peak layer is about 100 A or more, thick enough to be measured accurately by SIMS. In that sense, the Ge peak drop may be a more accurate measure of interdiffusion than the diffused shoulder profile. In terms of technology significance, the peak concentration determines the strain, chemical concentration, mobility and major band structure of a SiGe heterostructure, which is the focus of the modeling effort. Based on that consideration, interdiffusivity is modeled and fine-tuned using the TSUPREM-4 user-specified equation to fit the Ge peak drops. A Fickian diffusion equation with Ge

concentration gradient as the only driving force is used in the TSUPREM-4 simulator.

The interdiffusivity used in TSUPREM-4 in this work is modeled such that D depends exponentially on x_{Ge}, which is in good agreement with the extracted interdiffusivity in Figure 3-14 (a). The starting points of the exponential curves at $x_{Ge} = 0$ are calculated based on Zangenberg's Ge tracer diffusivity results in Si (squares in Figure 3-14 based on [51]). Figure 4-3 (a) shows the Ge profile simulated by TSUPREM-4 that best fits the SIMS peak profile of structure 56/56. The corresponding interdiffusivity expression used in TSUPREM-4 is $D = 4.2x10^{-20}\exp(8.1 * x_{Ge})$. The fit to the peak profile is reasonably good. Figure 4-3 (b) shows the fit of structure 45/45 annealed under the same condition. Using the same analytical expression as the diffusivity input, TSUPREM-4 generates a reasonable fit for the post-annealed SIMS profile of 45/45. However, the fit to the SIMS profile in the low x_{Ge} range is not as good as the fit to the peak drop. One possible explanation is the SIMS broadening effect as discussed earlier. This explanation does not appear to be complete, however, because SIMS can clearly resolve the sharper as-grown profiles shown in Figure 4-3. Another possible reason for the discrepancy at low Ge fractions is pipe diffusion along threading dislocations, which influences diffusion primarily in the low x_{Ge} range (dislocation effects are discussed in more detail in Section 4.4.2). A final possibility is that there remains a non-local nature to the interdiffusion, which impacts interdiffusion particularly at low Ge fractions. This phenomenon, if it exists, is not captured by the present model, and appears to be more prevalent in samples with high Ge fractions in the substrate (e.g. the profile discrepancy at low Ge fractions in Figure 4-3 (a) 56/56, is larger than that in Figure. 4-3 (b) 45/45, and larger than that in Figure 4-5 (a) BM20, which has only at 20% Ge relaxed SiGe substrate). The profile

discrepancy at low Ge contents thus may be related to some non-ideality in the alloy material in the interdiffused region, particularly where the strain is large and the critical thickness is small. It should be noted that in terms of overall profile motion, the interdiffusivity in the low Ge fraction range has little influence on the diffused profile and the peak drop, since most of the diffusion happens in the high Ge fraction range. Nevertheless, the limitations of the present model in predicting the Ge profile in the tail region, especially on high-Ge-content relaxed substrates, should be kept in mind when applying the model.

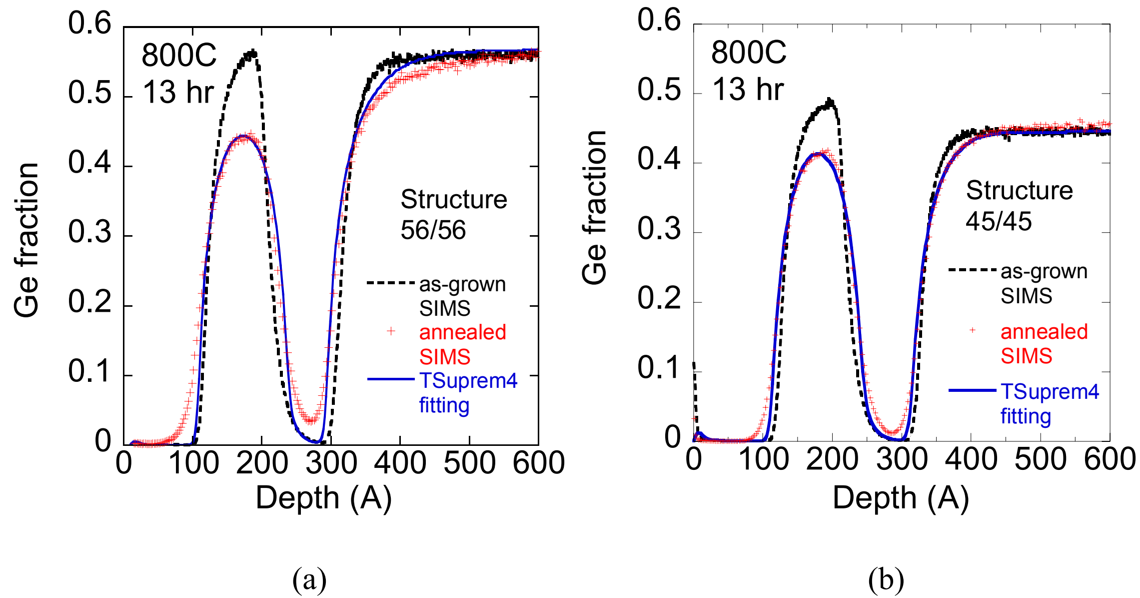

Figure 4-3 (a) As-grown and annealed SIMS profiles and the profile simulated by TSUPREM-4 that best fits the peak drop of structure 56/56 annealed at 800C for 13 hours. The corresponding interdiffusivity expression used in TSUPREM-4 is $D = 4.2x10^{-20}\exp(8.1 * x_{Ge})$. (b) Post-annealed Ge profile of structure 45/45 simulated by TSUPREM-4 using the same expression in (a), together with the as-grown and annealed SIMS profiles.

The expressions that best fit the SIMS peak drops for samples annealed at 800, 840 and 880 ºC are listed in Table 4-1. Other than sample 71F annealed at 840 ºC, which shows faster diffusion than the other two samples annealed at 840 ºC, all the samples

annealed at the same temperature show consistent diffusion behavior that can be described by one expression for a given temperature. Time dependence to the interdiffusivity was not observed under the annealing conditions in this study (e.g. 40 min. to 13 hrs. at 800ºC). It is not a surprise to see that the interdiffusivity expressions at different temperatures have the same x_{Ge} dependence, which agrees with results obtained from the Boltzmann-Matano study, in Figure 3-14. The only thing that is different for different temperatures is the prefactor in the diffusivity expressions, which shows temperature dependence.

Structure/anneals	60/60	45/45	D expressions and Comments
800C, 40mins	"71B", little diffusion	--	Consistent, not time-dependent, model **D=4.2e-20exp(8.1*x_{Ge})** fits all 5 samples
800C, 120mins	"71C", 2-3% peak drop	"75C", 1% peak drop	
800C, 13hrs	"71e", 12% peak drop,	"75e", 7% peak drop	
840C, 30mins	"71F", 8% peak drop	"75e2", 3.5% peak drop	75e2 and 75F consistent, **D=2.56e-19exp(8.1* x_{Ge})** 71F shows faster diffusion
840C, 3hrs	--	"75F", 8.5% peak drop	
880C, 30mins	"71A", 13% peak drop	"75D", 9% peak drop	71A and 71D consistent, **D=1.5e-18exp(8.1* x_{Ge})**

Table 4-1 Sample details and the interdiffusivity expressions that fit the SIMS peak drops at 800, 840 and 880 ºC.

4.1.3 Interdiffusivity Modeling

The interdiffusivity expressions in Table 4-1 enable us to find a single expression that

generates good fits to the SIMS peak diffusion profiles for the 14 samples in this work annealed under different conditions:

$$D_{R/T}(x_{Ge}) = 310\exp(-\frac{4.66\text{eV}}{\text{kT}})\exp(8.1 * x_{Ge}) \qquad \text{Equation 4-1}$$

In this equation, $D_{R/T}$ is the extracted and refined interdiffusivity for strained Si/relaxed SiGe structures. The subscript "R/T" refers to the strain status in the as-grown structures, which is either relaxed ($x_{Ge} = x_0$), or tensile strain ($x_{Ge} < x_0$). During annealing, the tensile strain may become relaxed, which is discussed further in Section 4.1.5. The $D_{R/T}$ model is based on Boltzmann-Matano analysis of diffused "step" samples, refined by SIMS peak fitting. In other words, $D_{R/T}$ provides a prediction of post-annealed SIMS peak profiles using TSUPREM-4.

Figure 4-4 shows $D_{R/T}$ results calculated from Equation 4-1 (solid lines) together with the extracted interdiffusivity from SIMS without refinement (in symbols). From Equation 4-1, we can see that at a given temperature, for every 10% increase in local Ge fraction x_{Ge}, there is a 2.2X increase in $D_{R/T}$. For every 40 ºC increase in temperature, there is about a 5X increase in $D_{R/T}$.

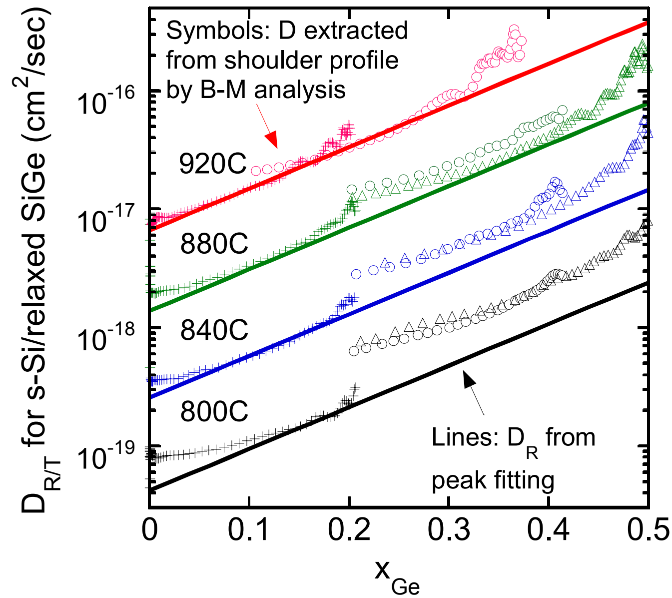

Figure 4-4 Interdiffusivity curves extracted from Boltzmann-Matano analysis of shoulder profiles (symbols) compared to $D_{R/T}$ refined using Tsuprem-4 to fit the SIMS peak profiles (solid lines).

Within experimental error, Equation 4-1 indicates that the diffusivity activation energy, *Ea*=4.66 eV is independent of Ge fraction and temperature, in the ranges studied in this work. Also the fact that the substrate Ge fraction x_0 has no impact on the interdiffusivity for the relaxed case is consistent with that observation from Figure 3-14. No anneal was performed on structures with Ge fractions higher than 0.4 at 920 ºC, and the uppermost line in Figure 4-4 shows the interdiffusivity at 920 ºC calculated from Equation 4-1, which is in good agreement with the extracted interdiffusivity from BM20 and BM40 at 920 ºC.

In order to test the $D_{R/T}$ model in Equation 4-1, TSUPREM-4 simulations using $D_{R/T}$ model were performed for a BM20 structure annealed at 800 ºC for 80 hours. Figure 4-5 shows the simulated profile and the SIMS measurement on both linear and semilog scales. Using an ideal step as the initial profile, the $D_{R/T}$ model generates a very good fit to the SIMS profile on both linear and semilog scales, which demonstrates the effectiveness of

the $D_{R/T}$ model, particularly in the low-Ge-content range.

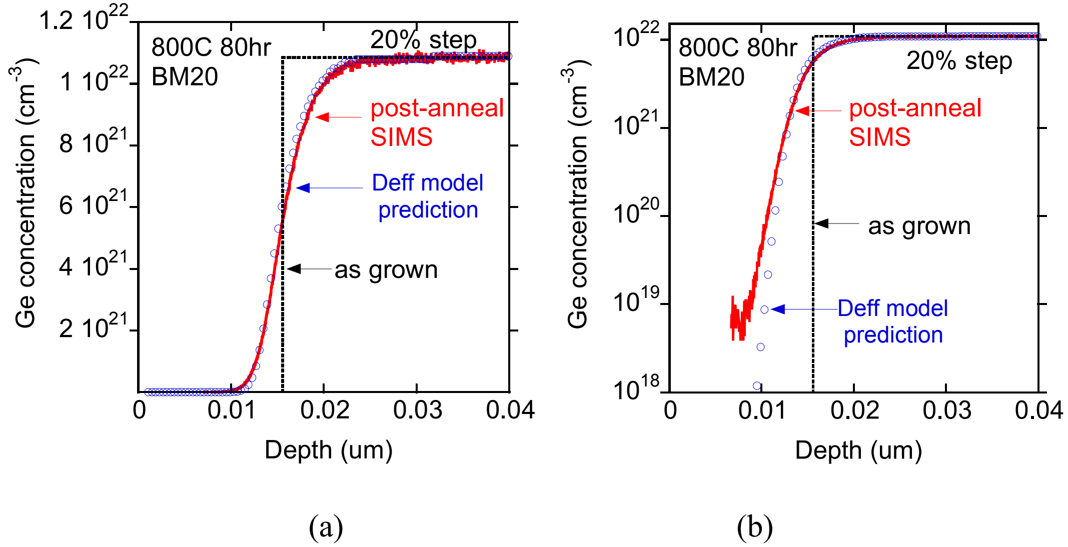

Figure 4-5 TSUPREM-4 simulations using $D_{R/T}$ model for BM20 structure annealed at 800C for 80 hours (symbols), on (a) linear, and (b) semilog, axes. The as-grown profile is an ideal step (dashed line), and the SIMS measurement is shown by the solid line.

4.1.4 Tensile Strain Characterization

After the interdiffusivity extraction and modeling, it is important to confirm the strain status to determine the accuracy of the strain assumptions made in the Boltzmann-Matano analysis, as in Equation 3-5. Collaboration was established with Dr. Michael Canonico of Freescale Semiconductor, Inc. (Physical Analysis Laboratory Arizona (PALAZ)), to obtain strain information using visible Raman and UV Raman measurements. All the Raman measurements for this study were performed by Dr. Michael Canonico.

Raman measurements of the “step” structures, which are the basis of this study, were examined first. To satisfy the Boltzmann-Matano assumptions, the “step” epitaxial structures should either be coherent to the virtual substrates or fully relaxed. In principle, either condition will satisfy the Boltzmann-Matano assumption, where the interdiffusivity

must be expressed as a function of x_{Ge} only (though clearly a fully coherent structure is much more appealing in terms of eliminating effects associated with strain relaxation and material non-idealities at the strained Si/SiGe interfaces). In this work, the structures were epitaxially grown, and the thickness of the strained layers is designed not to exceed twice the equilibrium critical thickness, as in practice, it has been found that a layer satisfying this condition will stay strained without suffering from large relaxation. It is assumed in this work that the intermixed region of SiGe (the sloped shoulder part) remains strained to the virtual substrate, and that the local strain can be expressed by Equation 3-5. Although it is difficult to probe strain in such narrow interdiffused regions, it is possible to probe the tensile strain in the strained Si capping layer (e.g. for sample BM60I, a step structure), which serves as indirect evidence that strain is maintained throughout the interdiffused region.

Sample BM60I has the highest step height and thus the smallest critical thickness, and was annealed at 880 ºC for 90 min, which is the longest anneal time at the highest annealing temperature among all "step" structure anneals. Therefore, this sample is most likely to suffer from strain relaxation. The Ge SIMS profile was measured on sample BM60E, which has the same structure and annealing condition as sample BM60I (see Figure 4-6). The Raman spectra were measured by 364 nm excitation laser, which has penetration depth of about 50 A. Figure 4-7 shows the Raman spectra of the Si-Si longitudinal optical (LO) phonon for the strained Si layer of sample BM60I, which is at 500.62 cm^{-1}.

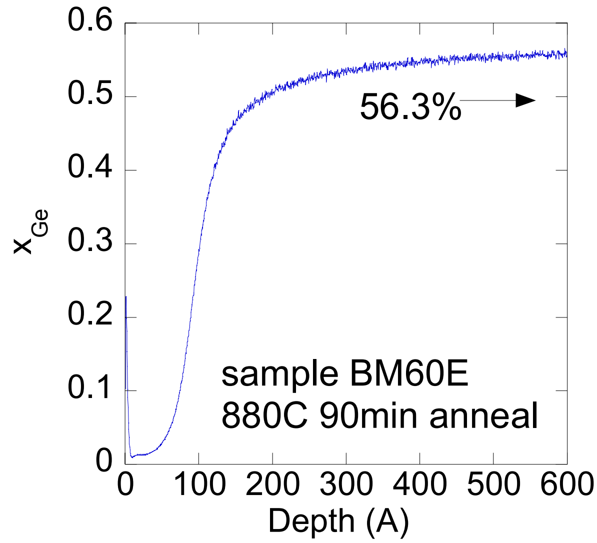

Figure 4-6 SIMS profile of sample BM60E annealed at 880C for 90 min.

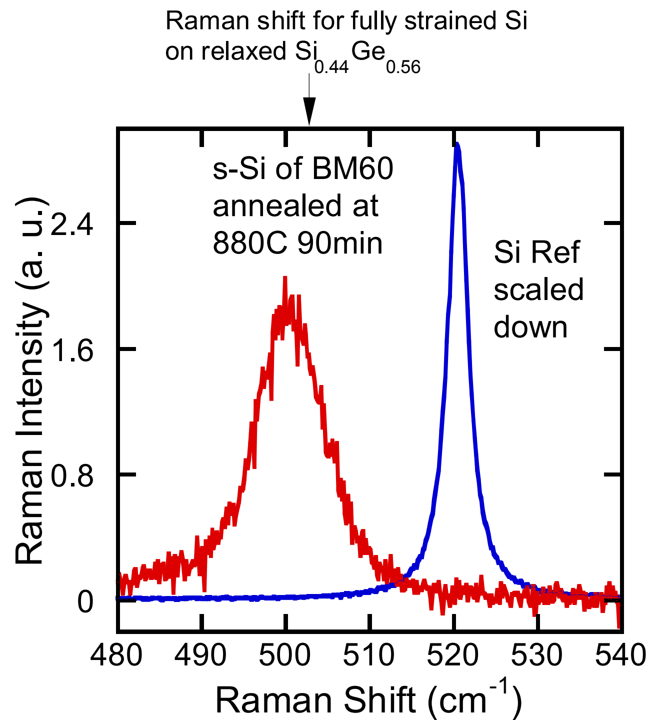

Figure 4-7 UV-Raman spectra (364 nm excitation) of the Si-Si longitudinal optical (LO) phonon for the strained Si layer in sample BM60I. Tensile strain is preserved after 880 ºC 90 min annealing. Raman data courtesy of Dr. Michael Canonico at Freescale Semiconductor, Inc.

Theoretically, the Raman peak position ω for a fully strained Si layer on top of

relaxed $Si_{1-x}Ge_x$ is:

$$\omega_{theory} - \omega_{Si,ref} = -x * 0.309 \qquad \text{Equation 4-2}$$

in which the Raman shift of a Si reference sample is 520.7 cm^{-1}. A fully strained Si layer on relaxed 56.3% SiGe should generate a Raman peak at 504.2 cm^{-1} based on the above equation [60]. Therefore, the measured Raman peak position, at 500.62 cm^{-1}, is 3.6 cm^{-1} less than the calculated Raman peak position.

One explanation for this discrepancy is the possibility of SIMS error in the Ge composition of relaxed SiGe. For example, if the relaxed SiGe is 60% instead of the 56% measured by SIMS, then the fully strained Si on 60% would move ω_{theory} to 502.2 cm^{-1}, which lowers the discrepancy to 1.6 cm^{-1}. Another possibility is that there are some Ge atoms diffused close to the surface, which could influence the Raman peak position by:

$$\Delta\omega = -x * 68cm^{-1} \qquad \text{Equation 4-3}$$

in which x is the Ge fraction. From the SIMS profile in Figure 4-6, in the top 50 A, the Ge percentage in the foot part is less than 1.5%, which can shift the Raman peak by 1.02 cm^{-1}. Another possibility is the thermal mismatch strain. This effect is shown in Appendix H to be insignificant. The above discrepancies are not large enough to change the fact that the strained Si layer remains strained to the virtual substrate after annealing, which suggests that the intermixed SiGe profile is also strained to the virtual substrate. This is consistent with the initial assumption of coherent as-grown and annealed structures. Therefore, the local strain can be expressed as a function of local Ge fraction x_{Ge} as in Equation 3-5, and the interdiffusivity can be written as a function of x_{Ge} only, which satisfies one of the Boltzmann-Matano analysis assumptions (see Equation 3-4 and 3-5).

Structure/anneals	56/56	60/30	30/60	30/30	30/00	BM60
As-grown	"71m"	"72cc"	"94E"	"95D"	"96D"	
800C, 40 min.		"72a"				
800C, 120 min.		"72b"				
840C, 30 min.		"72dd"				
880C, 30 min.	"71b"	"72d"				
880C, 90 min.			"94D"	"95C"	"96C"	BM60I

Table 4-2 Raman sample matrix in this work with sample structures and annealing conditions.

Table 4-2 summaries the structures and annealing conditions of all Raman samples. From the Raman measurements on "step" structures and "peak and step" structures (not shown in this thesis), tensile strain in strained Si layers is shown to be preserved for all the samples in Table 4-2. The Raman measurements for samples with compressive strain such as structures 60/30, 30/00 also show that compressive strain is preserved after annealing (the details of compressive strain characterization will be discussed in 4.2.2). Therefore, Raman measurements support the assumption of coherent structures before and after annealing, and thus the local strain dependence of the diffusivity, expressed in Equation 3-5. From Equation 3-5, any point with $x_{Ge} < x_0$ is under tensile strain. In "step" structures such as BM20, BM40, BM60 and in "peak and step" structures such as 56/56 and 45/45, tensile strain exists in the diffused shoulder and peak part of the profile, where $x_{Ge} < x_0$. In the next section, we will discuss the impact of tensile strain on interdiffusion.

4.1.5 Discussion on Tensile Strain Impact on Interdiffusion

So far, interdiffusivity data have been extracted by Boltzmann-Matano analysis and refined using TSUPREM-4. An analytical expression that fits SIMS peak diffusion profiles for the temperature range from 800 to 920 ºC was found. The interdiffusivity results for these different structures are close as shown in Figure 3-14 and Figure 4-4. However, it is clear that these structures have different as-grown strain in the strained Si layers, and different amounts of tensile strain in the interdiffused SiGe regions, during annealing. For example, in an as-grown BM20 structure, at $x_{Ge} = 0.1$, from the pseudomorphic growth condition and Equation 3-5, we can calculate the local strain as – (0.2-0.1)*0.042 = -0.42%, while in an as-grown BM40 structure, at $x_{Ge} = 0.1$, the local strain is – (0.4-0.1)*0.042 = -1.26%. Every point on the Ge profile in sample BM20 experiences a different local strain than its counterpart in BM40, since the Ge profiles are on two different relaxed virtual substrates. As long as the virtual substrate Ge content, *xo*, is different, the local strain for the same local x_{Ge} is different. Then, it becomes natural to ask why all the interdiffusivity values extracted in Figure 3-14 (a) appear to be so close for different step heights, and whether tensile strain has any effect at all.

The derivation below attempts to answer this question about the impact of tensile strain on the interdiffusivity. Assume that the total annealing time is t, the annealing time when the as-grown tensile strain is relaxed is t_R with the diffusivity for this period D_R, and the anneal period when tensile strain is not relaxed is t_T with the average diffusivity for this period D_T. Then we have:

$$D_{R/T}t = D_R t_R + D_T t_T \qquad \text{Equation 4-4}$$

$$t = t_R + t_T \qquad \text{Equation 4-5}$$

$$D_{R/T} = D_R \frac{t_R}{t} + D_T (1 - \frac{t_R}{t}) \quad \text{Equation 4-6}$$

From Figure 3-14, at the same temperature $D_{R/T}$ is relatively independent of structure. D_R is the interdiffusivity for diffusion under no strain, which should also be independent of structure. So in Equation 4-4, both $D_{R/T}$ and D_R are independent of structure, while $\frac{t_R}{t}$ should generally be dependent on structure and annealing time. The only two conditions that Equation 4-4 satisfies are: 1) $t_T << t$, which means tensile strain relaxes in the very early stages of annealing, or 2) $D_R \approx D_T$, which means the diffusivity under local tensile strain is close to that under relaxed strain. So far, there is one piece of indirect evidence in [51] that suggests $D_R \approx D_T$, where Ge self-diffusivity in $Si_{0.9}Ge_{0.1}$ under tensile strain is shown to be only slightly slower than that under relaxed strain. Whether one condition holds or both hold, this analysis implies that tensile strain does not have a significant effect on the interdiffusion processes in this study. Thus, in this work, $D_{R/T}$ for interdiffusion under initial tensile or relaxed strain is essentially close to D_R. Equation 4-1 can be rewritten as:

$$D_R(x_{Ge}) \approx D_{R/T} = 310 \exp(-\frac{4.66\text{eV}}{\text{kT}}) \exp(8.1 * x_{Ge}) \quad \text{Equation 4-7}$$

From now on, this equation will be referred as “the D_R model”.

4.2 Interdiffusion under Compressive Strain

4.2.1 Enhanced Interdiffusion under Compressive Strain

After obtaining the Si-Ge interdiffusivity for interdiffusion under initially relaxed

or tensile strain in the SiGe, the strain spectrum in the $Si_{1-y}Ge_y$ was extended to biaxial compressive strain by using "peak and step" structures with $y > x_0$. The epitaxial structures involved are 56/31, 45/15 and 30/00, in which the SiGe peak layers are under biaxial compressive strain of about -1%. The interdiffusion of a 56% Ge peak under compressive and relaxed strain under the same annealing condition is shown in Figure 4-8. It is clear that diffusion of the 56% SiGe peak is greatly enhanced in structure 56/31 compared to structure 56/56. Similarly, structure 56/31 and 45/15 annealed at other conditions (800 ºC for 40 and 120 min, and 840 ºC for 30 min), although not shown here, all exhibit much faster diffusion than their counterparts 56/56 and 45/45, where the SiGe peak layers are unstrained.

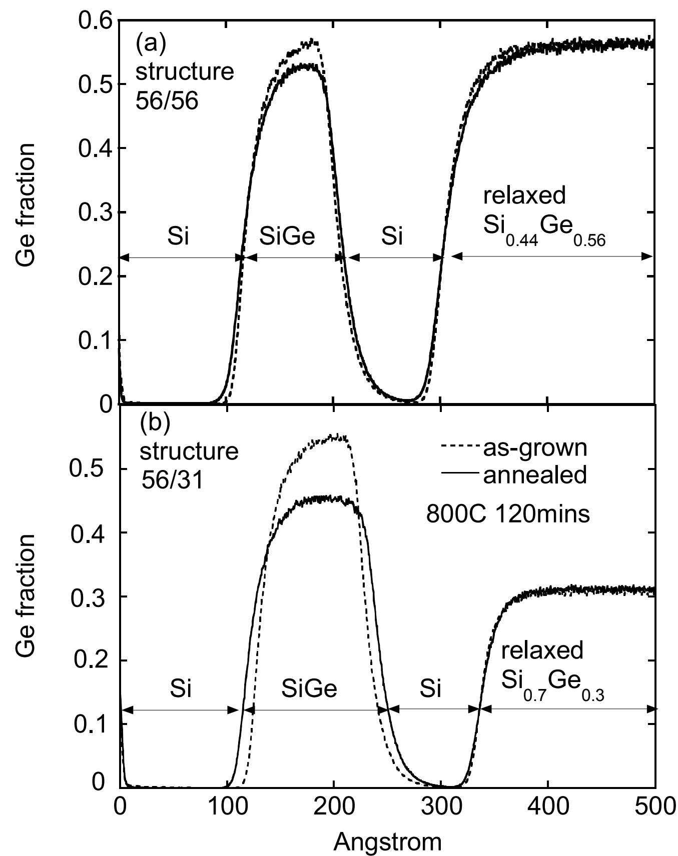

Figure 4-8 As-grown and annealed Ge SIMS profiles of (a) structure 56/56 and (b) structure 56/31, both annealed at 800° C for 120 min. Significantly faster diffusion is observed in (b) than (a).

4.2.2 Compressive Strain Characterization

In order to understand whether compressive strain plays a role in the observed diffusion enhancement, the strain status of strained Si and SiGe layers before and after diffusion was measured by visible Raman spectroscopy (442 nm excitation) at Freescale Semiconductor. Figure 4-9 shows the visible-Raman spectra of the Si-Si longitudinal optical (LO) phonon for structure 56/31 before and after diffusion at 800° C for 120 min., along with an unstrained Si reference sample. From the SIMS profiles in Figure 4-8(b), the peak Ge percentage dropped from 56% to 45% after annealing, but the SiGe layer remains strained to the relaxed $Si_{0.69}Ge_{0.31}$, based on Raman measurement and analysis [60]. After diffusion, the Raman shifts of the two strained Si layers and relaxed $Si_{0.69}Ge_{0.31}$ are unchanged. Similar Raman measurements were made for structure 56/31 annealed under two other annealing conditions: 800 °C for 40 min and 840 °C for 30 min, where enhanced diffusion is observed, and compressive stain is also showed to be preserved. Therefore, the enhanced interdiffusion is considered to be associated with the compressive strain in the SiGe layer.

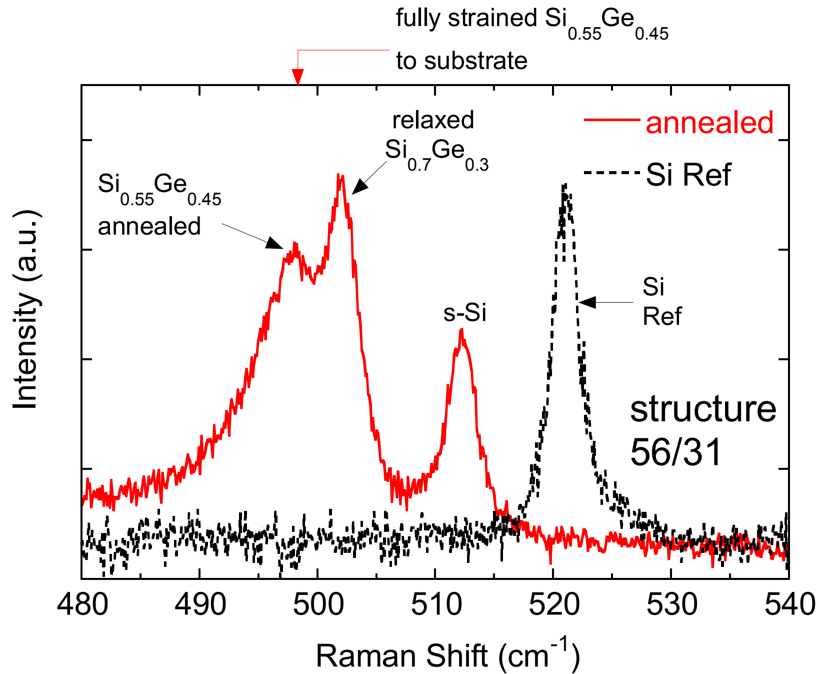

Figure 4-9 Raman spectra (442 nm excitation) of the Si-Si longitudinal optical (LO) phonon for structure 56/31 after 800°C 120 min (solid line) anneal along with an unstrained Si reference sample (dashed line). The arrows on top of this figure indicate the calculated Raman peak positions for SiGe layers fully strained to the relaxed $Si_{0.70}Ge_{0.30}$ substrates. Raman data courtesy of Dr. M. Canonico, Freescale Semiconductor.

4.2.3 Extraction and Modeling of Interdiffusivity under Compressive Strain

The D_R interdiffusivity model in Equation 4-5 can be modified to extract interdiffusivity under compressive strain. For example, in sample 56/31 annealed at 800 °C for 120 min. the top three layers are pseudomorphic to the relaxed $Si_{0.69}Ge_{0.31}$ virtual substrate before and after annealing, according to Raman measurements. Therefore, interdiffusion for $x_{Ge} \leq 31\%$ is under tensile or relaxed strain, to which the D_R model, Equation 4-5, should apply. The local strain for $x_{Ge} > 31\%$ is compressive. From SIMS results, the interdiffusivity under compressive strain (D_C) is significantly larger than D_R. We assume that the compressive strain dependence is exponential, which is generally

accepted [47,48,49]. Then the interdiffusivity in 56/31 can be modeled by a piece-wise exponential model in TSUPREM-4 to fit SIMS profiles using D_C for $x_{Ge} > 31\%$ and D_R for $x_{Ge} \leq 31\%$. Figure 4-10 (a) shows the SIMS profiles and the TSUPREM-4 simulation that best fits the Ge profile of the annealed structure 56/31. Some readers might have the impression that the Ge dose under the as-grown profile is different than that under the simulated profile, which is not the case. Ge dose is conserved in Figure 4-10 (a) TSUPREM-4 simulation, and more details can be found in Appendix I. The two solid segments in Figure 4-10 (b) are the interdiffusivity D_R from Equation 4-5 and D_C that yield the best fit to the SIMS peak profile.

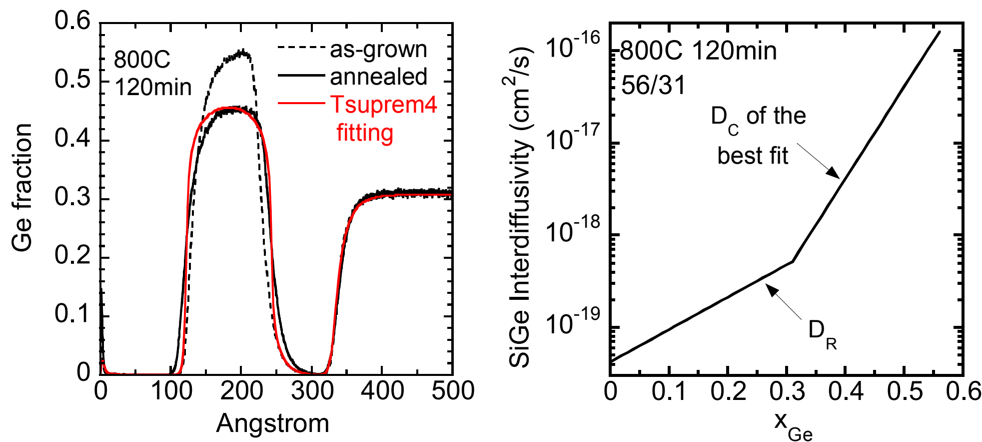

Figure 4-10 (a) SIMS profiles and the TSUPREM4 simulation that best fits the annealed peak of structure 56/31; (b) the interdiffusivities D_R and D_C that generate the best fit profile in (a).

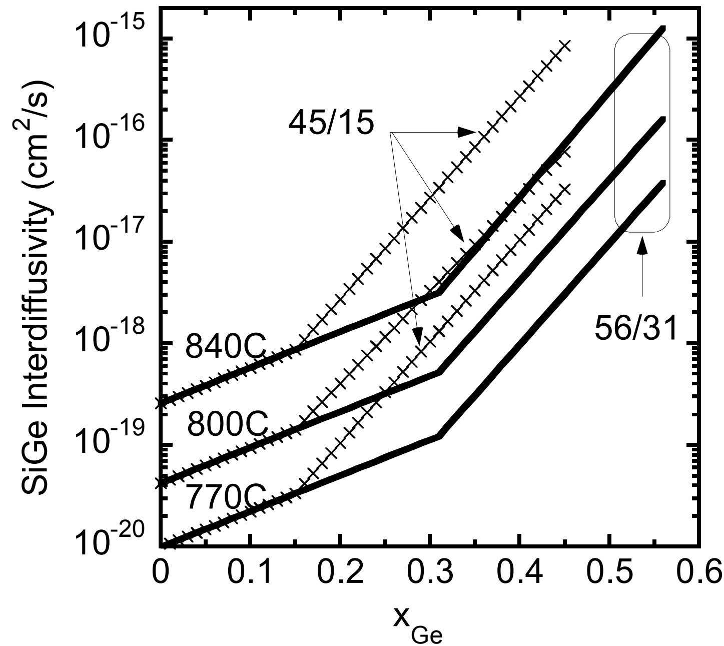

Figure 4-11 Extracted interdiffusivity curves for structure 56/31 (solid lines) and 45/15 (crosses) at temperatures in the range of 770-840 ºC.

Similar extractions were performed for the 56/31 and 45/15 samples annealed at 770, 800 and 840 °C, and the interdiffusivity results for the best fits are summarized in Figure 4-11. The slope of D_C versus x_{Ge} on a semilog scale is denoted as s_C, which includes effects from both local Ge concentration and the compressive strain. Table 4-3 is a summary of all s_C values extracted, which are found to be in the range of 21-27. The strain coupling factor Q'_{inter} is also calculated from s_C and tabulated in Table 4-3. The details of Q'_{inter} calculation will be discussed later in this section.

Structure	Ge30P15	Ge45P15	Ge56P15	Ge45P30	Ge56P30
x_0 =	0.15	0.15	0.15	0.31	0.31
840C, 30mins	"60A", 0% peak drop	"76F","76G": 9% peak drop agree	"61A", 16% peak drop	"62A", 4.5% peak drop	"72F", 10% peak drop
s_C of the bestfit	21 fits	23	21	27	24
Alternative fit	s_C=24 gives 1% more peak drop		s_C=24 gives 2% more peak drop	s_C=24 gives 0.5% less peak drop	
Q'_{inter} = (eV/percent strain)	--	0.342	0.2963	0.4341	0.3652
800C 120mins		"76C" 7% peak drop			"72C" 10% peak drop
s_C of the bestfit		21			23.8
Alternative fit		s_C=24 gives 2% more peak drop			
Q'_{inter} = (eV/percent strain)		0.2856			0.3299
770C, 7hrs		"76e2", 7% peak drop			"72e", 8% peak drop
s_C of the bestfit		23			23
Q'_{inter} = (eV/percent strain)		0.3207			0.3207

Table 4-3 The slopes of D_C against x_{Ge} (s_C) on a semilog scale used in Tsuprem-4 that best fits the SIMS peak drops, and Q'_{inter} calculated based on s_C.

The slope of D_C, s_C, is relatively independent of x_0 in the temperature range studied. To summarize the extracted D_C in Figure 4-11 with one analytic equation, we have:

$$D_C(x_{Ge}) = 310\exp(-\frac{4.66\text{eV}}{\text{kT}})\exp(8.1x_0)\exp[s_C*(x_{Ge} - x_0)] \quad \text{Equation 4-8}$$

where $x_{Ge} > x_0$ for compressive strain and s_C =21-27, with an average value of 23. This equation can be also written as:

$$D_C(x_{Ge}) = D_R(x_{Ge})*\exp[(s_C - 8.1)*(x_{Ge} - x_0)] \quad \text{Equation 4-9}$$

where $D_R(x_{Ge})$ is the interdiffusivity for local x_{Ge} under initial tensile or relaxed strain, and $\exp[(s_C - 8.1)*(x_{Ge} - x_0)]$) is the enhancement factor due to the compressive strain. According to Equation 3-5 and taking 23 as the average value of s_C, the above equation can be written as a function of compressive strain ε_C,

$$D_C(x_{Ge}) = D_R(x_{Ge})*\exp(14.9*\frac{|\varepsilon_C|}{0.042}) \quad \text{Equation 4-10}$$

From Equation 4-7 and 4-8, at the same local x_{Ge}, for every 10% decrease in substrate Ge fraction x_0 (equivalent to 0.42% increase in the absolute value of compressive strain), there is a 4.4X increase in D_C. The x_0 dependence (compressive strain impact) is stronger than the local Ge fraction dependence, which increases by 2.2X for every 10% increase in x_{Ge}. From now on, Equation 4-7 and 4-8 will be referred to as the D_C model for interdiffusion under compressive strain. The combination of the D_R model and the D_C model will be referred to as the D_R-D_C model. Now, we are ready to use this model to predict interdiffusion using TSUPREM-4 simulations. An example of TSUPREM-4 input code is given in Appendix J for reference.

4.2.4 Strain Coupling Factor and Its Origin

Although the compressive strain dependence of interdiffusion is observed, it is not clear whether this strain dependence is due to a change in activation energy, *Ea* or

prefactor, D_0, in the generalized expression $D = D_0\exp(-Ea/\mathrm{kT})$. For dopant diffusion in Si and SiGe, the biaxial strain dependence of diffusivity is generally assumed to be related to a change in activation energy, associated with a change in the formation energy of point defects involved in dopant diffusion [61].

$$E_a(\varepsilon_{C,biax}) = E_a(0) - Q'\left|\varepsilon_{C,biax}\right| \qquad \text{Equation 4-11}$$

Q' is the biaxial strain coupling factor for dopants, and can be calculated from the diffusivity dependence on strain:

$$Q' = -kT\frac{\partial \ln D_{dopant}}{\partial \varepsilon} \qquad \text{Equation 4-12}$$

In this work, the exponential dependence of interdiffusivity on compressive strain is also observed. Cowern et al. demonstrated that $\frac{D(s)}{D(0)} = \exp(\frac{A*\varepsilon_{biax}}{kT})$ for SiGe interdiffusion at low Ge fractions. "A" is a constant which includes both chemical and strain effects. Therefore, it is likely that the origin of the compressive strain dependence observed in this work is the change in Ea. If that is true, the strain coupling factor Q'_{inter} can be calculated for Si-Ge interdiffusion under biaxial strain as:

$$Q'_{inter} = -kT\frac{\partial \ln D_{inter}}{\partial \varepsilon} \qquad \text{Equation 4-13}$$

From the D_C results in Equation 4-7, we have:

$$Q'_{inter} = \frac{(s-8.1)*kT}{0.042*q}eV/strain \qquad \text{Equation 4-14}$$

$$Q'_{inter} = \frac{(s-8.1)*kT*100}{0.042*q}eV/percent-strain \qquad \text{Equation 4-15}$$

Q'_{inter} is calculated to be in the range of 0.276 ~ 0.363 eV/percent strain for

temperatures from 770 to 840 °C for interdiffusion under compressive strain (see Table 4-3). In this work, the maximum compressive strain is about -1% as in structure 56/31. Therefore, if the coupling is due to an *Ea* change, under -1% compressive strain, the activation energy should be about 0.3 eV less than the interdiffusivity under relaxed strain. A change in *Ea* of 0.3 eV is actually a subtle change, which is very hard to distinguish from a pre-factor change, with the narrow temperature range used in this work, as illustrated in Figure 4-12. Figure 4-12 shows the temperature dependence of D(x_{Ge}=0.4) under different strain status. For example, $D(x_{Ge}=0.4)$ in structure 45/15 is under compressive strain of –(0.4-0.15)*4.2% = - 1.05%, while $D(x_{Ge}=0.4)$ in structure 56/31 is under compressive strain of –(0.4-0.31)*4.2% = -0.38%. The third case is where D (x_{Ge}=0.4) is under no strain. The activation energies from the least square fitting lines are 4.71, 4.80 and 4.66 eV respectively. From Figure 4-12, it can be seen that the *Ea* uncertainty is larger than 0.3 eV (especially for 45/15), which means we are not able to distinguish a change in *Ea* from a change in pre-factor. One way to reduce the uncertainty in *Ea* is to run multiple samples at each annealing condition to get a statistical average of diffusivity. A more fundamental method to solve this problem is to expand the temperature range.

In previous work on Ge self diffusion, an *Ea* accuracy of 0.1 eV was obtained, using temperature ranges of two to three hundreds degrees [51], [62]. Since the interdiffusivity increases about 4 to 5X for every 40 ºC increase, expanding the temperature range requires extremely short anneals at high temperatures and very long anneals at low temperatures, since the overall amount of profile broadening is limited in these types of structures by critical thickness constraints. For example, the annealing time

for BM20 at 880 ºC in this work is 80 hours. If *Ea* = 4.66eV still holds for temperature range 700-800 ºC, the temperature term for 700 ºC is 1/177 of that at 800 ºC. In order to obtain the same amount of profile motion at 700 ºC, 80*177 hours = 1.42e3 hours = 590 days is required. Therefore, interdiffusivity data for low Ge fraction becomes very difficult to obtain at low temperature, which is fortunately not of technical importance. Interdiffusivity extraction for high Ge fraction (x_{Ge} > 0.6) with high compressive strain at low temperature is more feasible and relevant to Ge-rich and pure Ge MOSFET fabrication, which is a topic for future work. By varying Ge fraction, strain and temperature at the same time, it should be possible to expand the *D* vs. x_{Ge} plot in Figure 4-4 and Figure 4-11 to a wider temperature range, which will help to obtain more accurate understanding of the impact of strain on *Ea*.

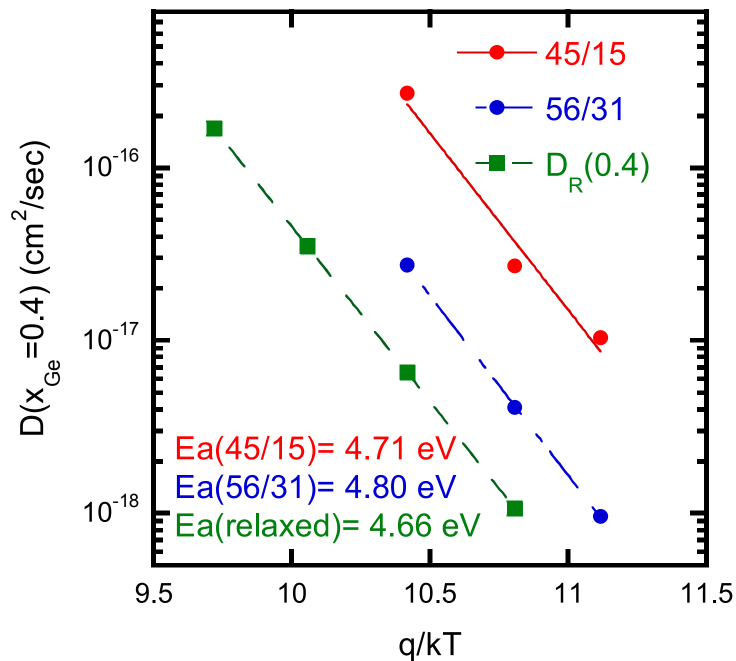

Figure 4-12 Temperature dependence of D(x_{Ge}=0.4) under different strain status and the corresponding activation energies. The lines are the best fit lines using least square method.

4.2.5 Error Analysis

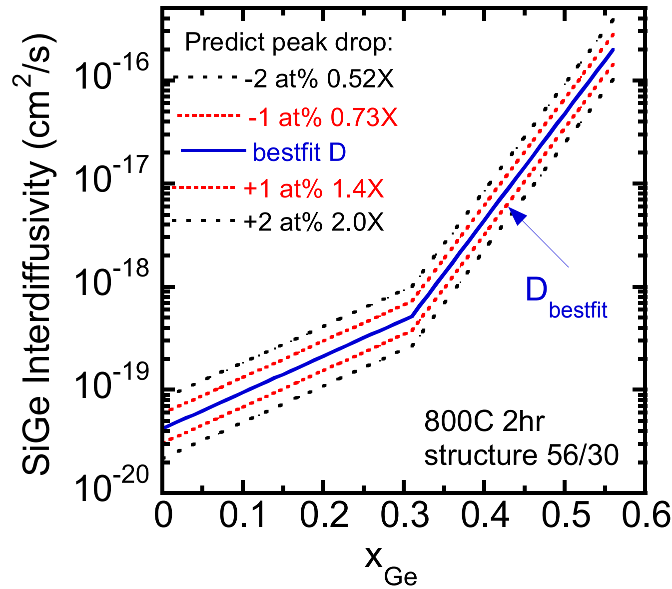

Figure 4-13 Interdiffusivity curves and error bars for structure 56/31. The solid line is the interdiffusivity curve $D_{bestfit}$ that fits SIMS peak profile in Figure 4-10. The dashed and dotted lines are the diffusivity curves which predict peak drops that are off by -2, -1, +1, and +2 at%. The corresponding diffusivity ratios relative to D_{bestfit} are 0.52, 0.73, 1.4 and 2.0.

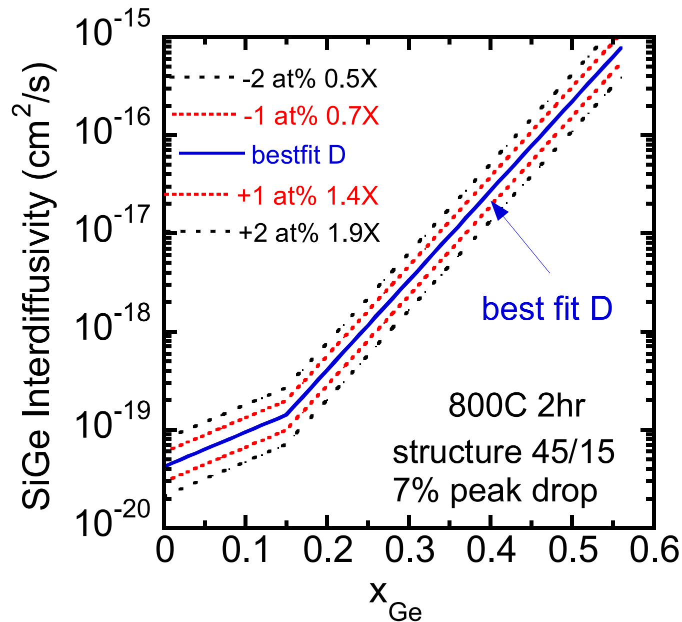

Figure 4-14 Relative error in D extraction caused by SIMS errors assuming SIMS gives errors within ± 2 at% and ± 1 at%. The solid line is the interdiffusivity curve $D_{bestfit}$ that fits SIMS peak profile.

After extracting D_C shown in Figure 4-10 and Figure 4-11, an error analysis was

performed. The main source of error comes from SIMS. The peak drops of this study are from 7 to 10 atomic %. Based on discussions with Dr. Gary Goodman at Evans Analytical Group, where samples of this work were measured, the SIMS accuracy for Ge fraction is around ±1 atomic percent (at.%) for samples measured in a single day, and ±2 at.% for measurements performed on different days. Figure 4-13 shows the relative errors that are introduced when SIMS is off by ±1 at.% or ±2 at.%. The corresponding diffusivity values are 0.7-1.4X and 0.5-2.0X of the best fit interdiffusivity $D_{bestfit}$. In the case that the peak drop is 7%, as in structure 45/15 annealed at 800 °C for 120 min, the relative error is 0.7-1.4X and 0.5-1.9X of $D_{bestfit}$ respectively when the SIMS peak is off by ±1 at.% and ±2 at.%. In this work, most of the as-grown and annealed samples of the same structure were measured by SIMS in one day. Therefore, we estimate the error bar of the interdiffusivity is 70 to 150% of the best fit interdiffusivity.

4.2.6 On the Uniqueness of the Diffusivity Model for the Strain Effect

As mentioned with respect to the D_C extraction, it was assumed that the compressive strain dependence is exponential. Since the measurement of the interdiffusivity is based on fitting peak drops, the extracted interdiffusivity data are most valid in range of Ge fractions near the peak of the profile. It is possible that the exponential assumption is not unique and the extracted data is just one set of solutions which generate good fits in the range of peak drops for the 45/15 and 56/30 samples.

To test the assumption of the exponential dependence on compressive strain, two series of structures were designed on 15% and 30% relaxed virtual substrates respectively. Series (A) includes structures 56/15, 45/15, and 30/15, and series (B) consists of 56/31

and 45/31. Both series of samples were annealed under the same conditions: 840 ºC for 30 min in nitrogen ambient. The peak drops of these samples are different because of the different peak heights and substrate Ge fractions. From SIMS measurements (not shown in this thesis), the peak Ge concentrations dropped according to the values shown in Table 4-4. D_C extraction was performed for all these samples using the same piece-wise exponential dependence and compared in Figure 4-15. The logic for this comparison is the following: if the exponential dependence is a good assumption in the whole range, the extracted data of the structures in the same series (i.e. on the same virtual substrate) should follow the same exponential relation independent of the peak drop ranges; if the exponential dependence is incorrect, then the extracted data of the structures in the same series will not follow the exponential behavior.

Structures	Series (A)			Series (B)	
	30/15	45/15	56/15	45/30	56/30
Pre-anneal peak height	26%	45%	56%	45%	55%
Peak height after 840C 30min anneal	26%	36%	40%	41%	45%

Table 4-4 Ge peak heights before and after 840C 30min anneals for structures in series (A) and (B).

As seen in Figure 4-15, the extracted interdiffusivity data from the same series agree with each other within the error bars (dashed regions). Structure 30/15 in series (a) had no observable peak drop, which agrees with the prediction using the interdiffusivity extracted from 56/15 and 45/15. Therefore, our exponential dependence of interdiffusivity on compressive strain appears to be valid, within the experimental error bar.

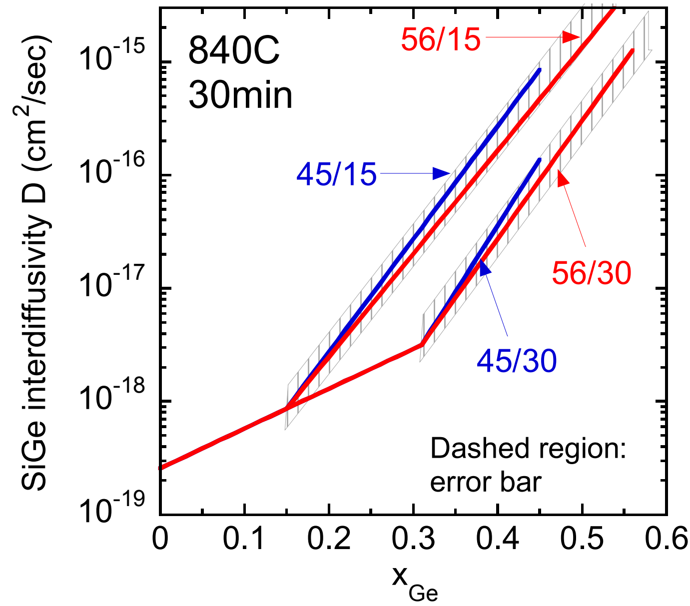

Figure 4-15 Extracted interdiffusivity curves to check the uniqueness of the model concerning the impact of strain on the diffusivity. Series (a) consists of structure 56/15 and 45/15. Series (b) consists of structure 56/31 and 45/31.

4.3 Discussions

4.3.1 Comparison with literature

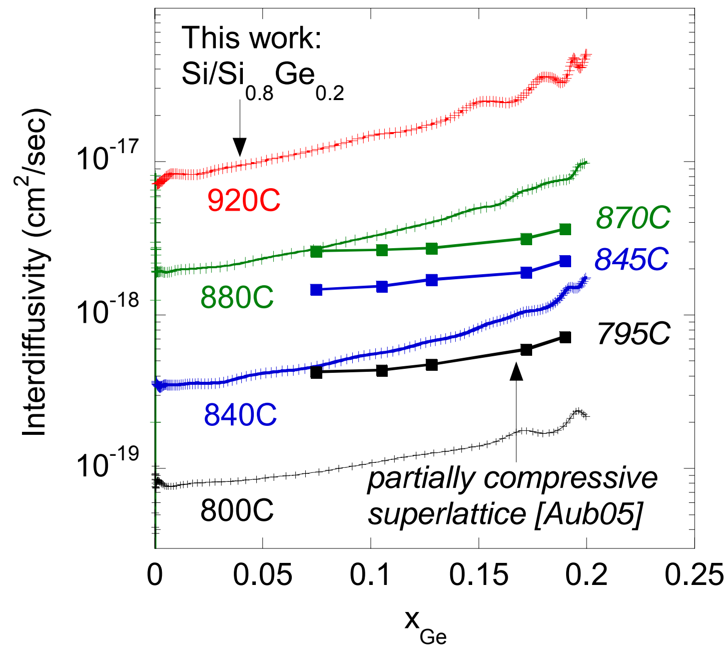

Figure 4-16 Comparison between interdiffusivity from Aubertine et al's work [48] and that extracted using Boltzmann-Matano analysis in this work without TSUPREM-4 refinement, for Ge fraction < 0.2.

To date, the most comprehensive interdiffusivity study was performed by Aubertine et. al. using XRD as a diffusion probing method [48]. The structures used in their work were $Si_{1-x}Ge_x/Si_{1-y}Ge_y$ superlattice structures grown on a Si substrate. Aubertine's work gave interdiffusivity at five discrete average Ge fractions, x_{Ge} = 0.075, 0.105, 0.128, 0.172 and 0.192. These samples exhibited 75%, 56%, 5%, 56% and 73% strain relaxation. Figure 4-16 compares Aubertine's interdiffusivity results with the extracted interdiffusivity of this work. Although there are significant differences in samples structures and experimental techniques between these two studies, the extracted interdiffusivities are in approximately the same range. In terms of activation energy, Aubertine found a Ge fraction dependence to $Ea = 4.69 - 4.05 * x_{Ge}$ (eV) for Ge fraction < 0.2, while Ea = 4.66 eV in this work with little dependence on x_{Ge}. More work needs to be done to extract Ea in wider temperature range to explain the difference in these two studies.

4.3.2 Interdiffusion Mechanisms and the Impact of Strain

The observation in this work that compressive strain enhances interdiffusion is consistent with the findings of Cowern, *et. al.* on Si/200-1200A $Si_{1-x}Ge_x$/Si structures (x = 0.1-0.3) annealed at 900-1050ºC [49]. Si-Ge interdiffusion is considered to be mediated by vacancies more than interstitials [49, 63]. Compressive strain in the SiGe favors vacancy formation, and therefore may be expected to enhance Ge diffusion in the process of Si-Ge interdiffusion. In this work strain is varied by using different relaxed $Si_{1-x}Ge_x$ substrates, which not only changes strain in the $Si_{1-y}Ge_y$ layer but also the strain in the surrounding two strained Si (s-Si) layers. For example, the 56% SiGe peak in structure

56/31 is under biaxial compressive strain of about –1%, and the two surrounding s-Si layers are under biaxial tensile strain of about 1%. For comparison, the 56% SiGe peak in structure 56/56 is unstrained, and the two surrounding s-Si layers are under about 2% biaxial tensile strain. It is possible that strain changes in both the $Si_{1-y}Ge_y$ layer and two s-Si layers contribute to the observed diffusivity changes. In the structures in this study, it is difficult to decouple strain in the $Si_{1-y}Ge_y$ layer and strained Si layers without introducing strain relaxation and thus much higher dislocation density. However, the magnitudes of the influences from compressive strain and tensile strain are different. Our analysis in Section 4.1.5 suggests that tensile strain in SiGe has little impact on Si-Ge interdiffusion. Therefore, by analogy, it is plausible that tensile strain in Si has little effect on interdiffusion in strained Si/SiGe/Si structures, and that it is the compressive strain in the $Si_{1-y}Ge_y$ layer that plays the dominant role in the enhancement of interdiffusion. In the next section, the impact of the surrounding layers on the Si-Ge interdiffusivity is further explored.

4.4 Surrounding Layer and Threading Dislocation Effects

4.4.1 Surrounding Layer Effect

Up to this point, all the extraction and modeling have been performed for the intermixing of Strained Si/SiGe interfaces. Interdiffusion depends on the materials on both sides of the interface. A natural question to ask is whether the D_R-D_C interdiffusivity model applies to the case of $Si_{1-x}Ge_x/Si_{1-y}Ge_y$ intermixing. For the case of Strained Si/SiGe interdiffusion, although the sample begins with a Strained Si/SiGe interface at time zero, once diffusion starts, the "sharp" interface becomes sloped. At any point along the slope, SiGe diffuses into the surrounding SiGe, and this interdiffusion behavior is

captured by the D_R-D_C model. Therefore, the D_R-D_C model should be applicable to the case of intermixing of as-grown $Si_{1-x}Ge_x/Si_{1-y}Ge_y$ interfaces.

Modified 56/31 structures were designed by substituting the surrounding strained Si layers by SiGe layers to measure the surrounding layer effect. The substituting layers are $Si_{0.55}Ge_{0.45}$ as in structure 56/45/31 in Figure 4-17 (b), $Si_{0.68}Ge_{0.32}$ as in structure 56/32/31 in Figure 4-17 (c), and $Si_{0.84}Ge_{0.16}$ as in structure 56/16/31 in Figure 4-17 (d). These structures were annealed in nitrogen at 800 °C for 120 min. Figure 4-17 shows the Ge profiles for these modified 56/31 structures before and after the annealing (Figure 4-17 (b), (c) and (d)) compared with the original 56/31 structure (Figure 4-17 (a)). A similar amount of interdiffusion is observed between Figure 4-17 (a) and (b). Figure 4-17 (c) and (d), with higher Ge contents in the surrounding layers, show less peak drop. This is consistent with a change in the "boundary condition" on either side of the 56% Ge peak layer: the Ge diffuses away much faster when surrounded by 30% and 45% Ge alloy layers. Interdiffusivity extracted by TSUPREM-4 for structures in Figure 4-17 (b), (c) and (d) is shown in Figure 4-18, and compared with interdiffusivity extracted from 56/31. Within the experimental error, the interdiffusivity data for 56/17/31, 56/32/31, 56/45/31 structures agree with that for 56/31, which means that the D_R-D_C model applies to the case of $Si_{1-x}Ge_x/Si_{1-y}Ge_y$ intermixing.

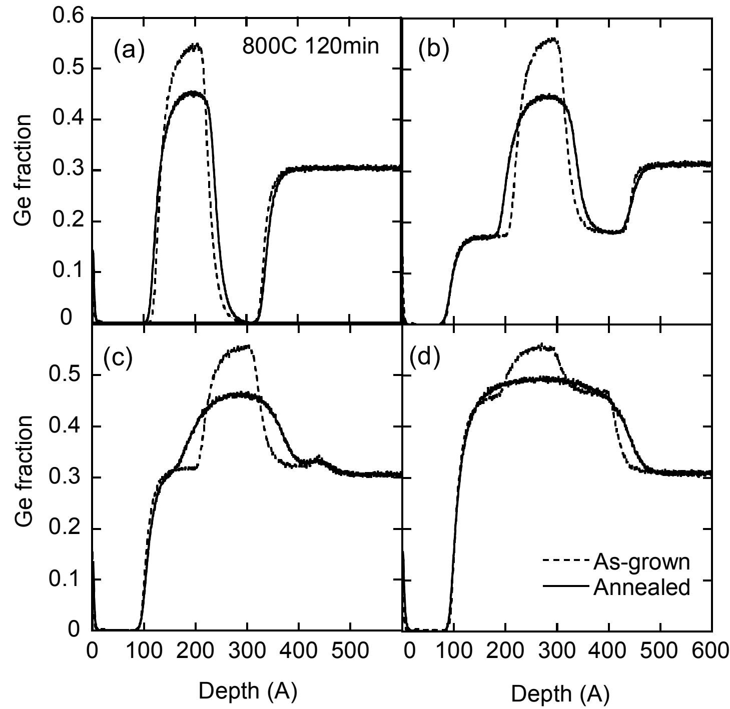

Figure 4-17 As-grown and annealed Ge profiles measured by SIMS for (a) structure 56/31, (b) structure 56/17/31, (c) structure 56/32/31 and (d) structure 56/47/31.

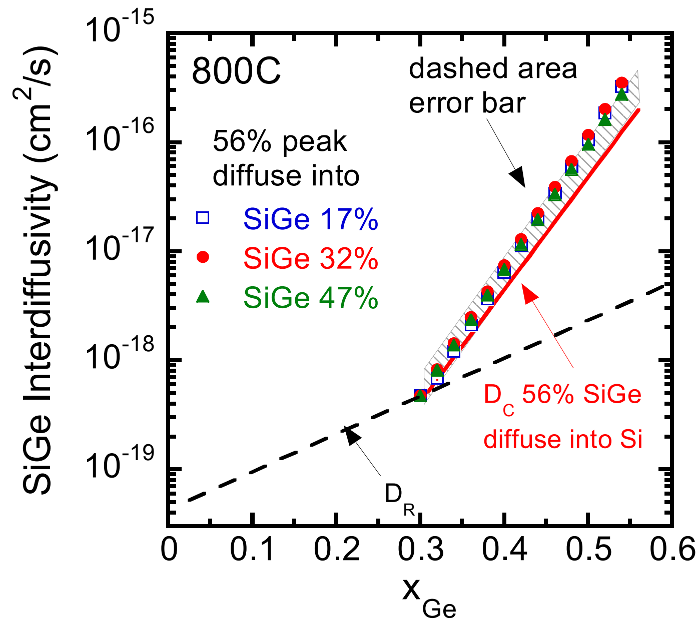

Figure 4-18 Interdiffusivity curves that best fit the annealed profiles in Figure 4-17 (a) to (d). The lines are the interdiffusivity extracted for structure 56/31, i.e. the D_R-D_C model.

4.4.2 Threading Dislocation Effect

The samples studied in this work were grown on different virtual substrates, and may have different threading dislocation densities. It has been suggested that pipe diffusion along vertical threading dislocation segments can contribute to the interdiffusion at Strained Si/SiGe interfaces. To study the threading dislocation effect on interdiffusion, we compared the interdiffusion of structure 30/00 (relaxed Si/compressive $Si_{0.7}Ge_{0.3}$/relaxed Si structure) grown on a CZ substrate and on a highly defected substrate ("virtual Si substrate" with dislocation density on the order of 10^7 cm^{-2}). The defected substrate was fabricated by starting with a CZ Si wafer, which was followed by epitaxial growth of a relaxed graded SiGe layer from 2% up to 30% in Ge fraction, a 1 micron-thick constant-concentration 30% SiGe layer, another graded SiGe layer from 30% SiGe down to 0%, and finally a 1 micron-thick relaxed epitaxial Si layer (see Figure 4-19 (a)). The grading rate was about 10% Ge/um for both graded SiGe layers. The dislocation density measured by etch pit density (EPD) method on the defected substrate is about 2 to 4 x 10^7 cm^{-2}, while that of the thick epitaxial Si layer grown on the CZ substrate is less than 1 x 10^2 cm^{-2}.

Both 30/00 on defected substrate and on CZ substrate were annealed in nitrogen at 880 ºC for 90 min and measured by SIMS. The amount of peak diffusion is similar between these two structures as seen in Figure 4-19 (b), which is consistent with Mooney *et al.*'s findings [58]. However, the low Ge fraction diffusion of these two samples is different. Structure 30/00 on defected substrate has a much bigger tail than the same structure grown on a CZ substrate. Therefore, it is likely that the effect from pipe diffusion along threading dislocations (with density on the order of 10^7 cm^{-2}) is only observable in the low Ge fraction range (i.e. in the profile tail regions), but not large

enough to impact diffusion at high Ge fractions. From etch pit density measurements, the threading dislocation densities of the virtual substrates in this work such as sample BM20, BM40 and BM60 are all on the order of 10^5 cm^{-2}, much lower than 10^7 cm^{-2}. It is reasonable to conclude that the substrate quality has little effect on the major features of Si-Ge interdiffusion studied in this work. However, threading dislocations, originating either from the substrate or in higher densities from the relaxation of a thin layer in the interdiffusion structure, could impact the low-Ge-fraction portion of the profiles, leading to Ge tail regions. Diffusion in these tail regions is not captured by the models in this work and is suggested as an area for future study.

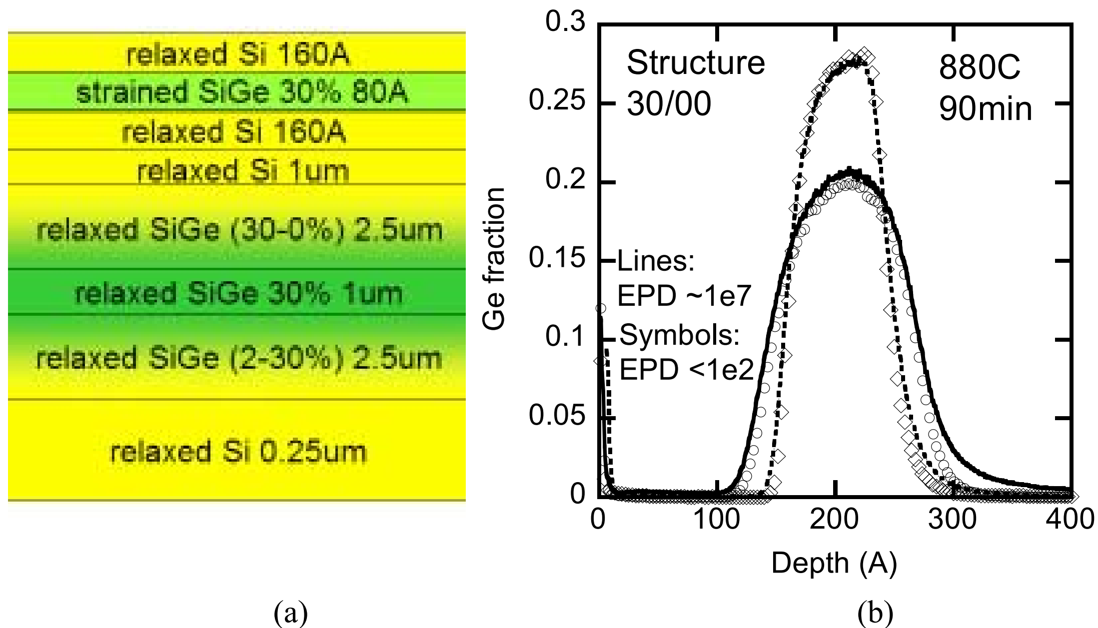

(a) (b)

Figure 4-19 (a) The epitaxial structure of the 30/00 on defected substrate. (b) As-grown and annealed Ge profiles measured by SIMS for structure 30/00 grown on CZ substrate with less than 1 x 10^2 cm^{-2} dislocation density and on defected substrate with about 1 x 10^7 cm^{-2} dislocation density.

4.5 Impact on Technology

In the beginning of Chapter 3, we introduced the significance of SiGe interdiffusion

for various SiGe devices such as CMOS, bipolar transistors, photodiodes. In this work, a Si-Ge interdiffusivity model was extracted for epitaxial strained Si/$Si_{1-y}Ge_y$/strained Si/relaxed $Si_{1-x0}Ge_{x0}$ and strained Si/relaxed $Si_{1-x0}Ge_{x0}$ heterostructures for Ge fractions between 0 and 0.56 over a temperature range of 770 – 920 ºC. These results can be used to predict SiGe interdiffusion, and for optimizing device structure design and process integration. In the following sections, a few examples of the application of the interdiffusivity model are given.

4.5.1 Impact on HOI and Dual-channel MOSFET Design

As mentioned in Section 3.1, heterostructure-on-insulator (HOI) and dual-channel MOSFETs use SiGe layers as high-hole-mobility channels. High thermal budget will degrade the mobility due to interdiffusion. In addition, Ge atoms that diffuse through the Si capping layer to the oxide/Si interface contribute to the density of interface traps and degrade device performance. To minimize interdiffusion, a low-Ge-fraction SiGe layer under tensile or relaxed strain is preferred. However, in terms of mobility, high Ge fraction is desirable and a certain amount of compressive strain is needed to split the valence bands and reduce scattering within the SiGe layer. Therefore, it is essential to design the epitaxial structures and thermal process carefully to balance the requirements from both the device design and process points of view.

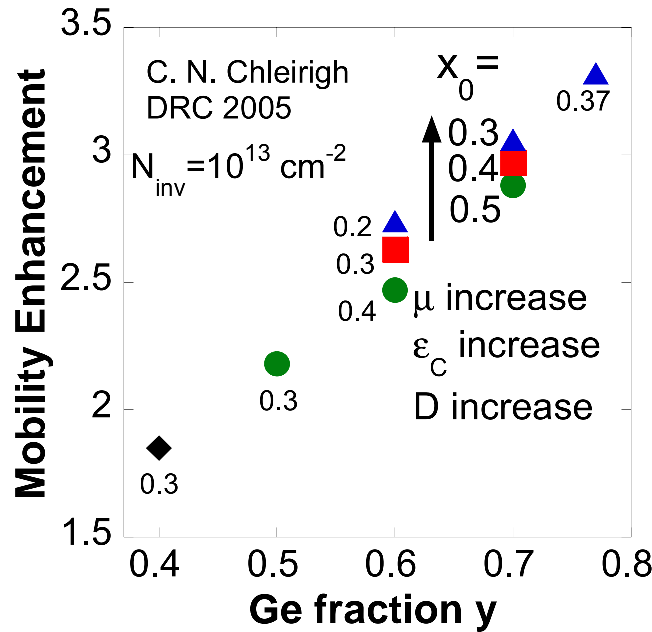

Figure 4-20 Hole mobility enhancement factor for dual-channel p-MOSFETs as a function of Ge fraction *y* in the hole channel layer and Ge fraction x_0 in the virtual substrate after possessing. Figure from [64].

Figure 4-20 shows published hole mobility enhancement factor for dual-channel p-MOSFETs (strained Si/$Si_{1-y}Ge_y$/strained Si/$Si_{1-x0}Ge_{x0}$) as a function of Ge fraction y (in the channel layer) and x_0 (in the virtual substrate) [64]. As seen in Figure 4-20, for a given y, a small change in x_0 doesn't change the mobility enhancement factor significantly. Therefore, it may make sense to increase x_0 somewhat, which reduces the compressive strain in the channel and thus the interdiffusion during processing. In the following device design example, interdiffusion prediction using the D_R-D_C model is combined with the mobility results in Figure 4-20 for device structure optimization.

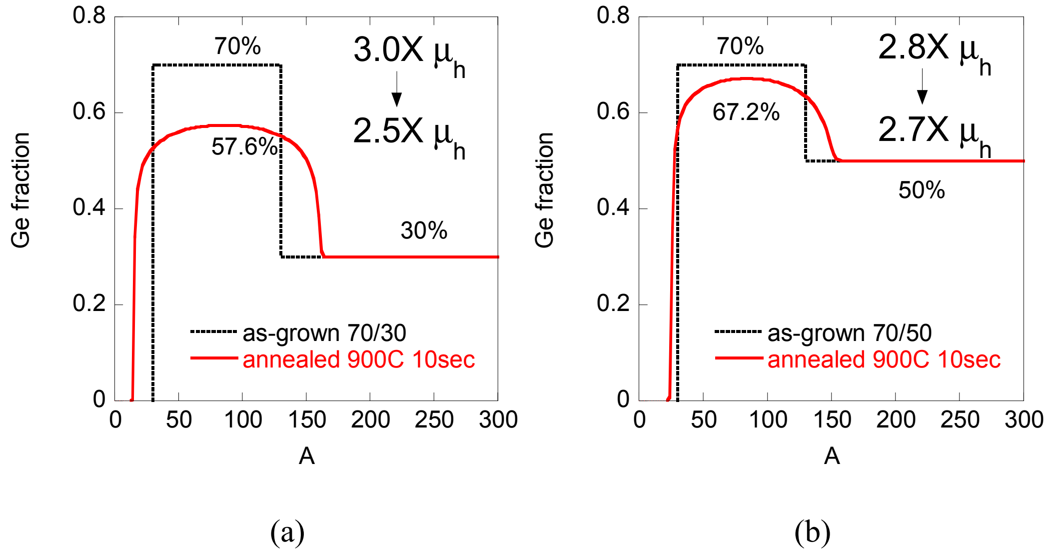

Figure 4-21 An example of dual-channel MOSFET structure design. The RTA is at 900 ºC for 10sec. (a) structure 70/30 (b) structure 70/50. Ge diffusion in (b) is much less than in (a).

Figure 4-21 illustrates an example of dual channel MOSFET structure design. Assume that the thermal budget is limited to 900 ºC for 10 sec., and the design goal is to achieve at least 2.5X hole mobility enhancement. Referring to Figure 4-20, a 2.5X enhancement can be achieved for y = 0.6 and above. Interdiffusion is compared for structures with y=0.7 and x_0 = 0.3 (structure 70/30) and 0.5 (structure 70/50). In structure 70/50, the 70% peak is under less compressive strain than in structure 70/30. The D_R-D_C model is used to predict interdiffusion for a 900 ºC-10 sec. RTA, as seen in Figure 4-21. The as-grown Ge profile was generated to emulate a dual-channel MOSFET structure with a 30 A Si cap and 100 A SiGe channel.

After diffusion, the 70% Ge peak dropped to 58% in (a) and to 67% in (b). From Figure 4-20, we estimate that the hole mobility enhancement factors for post-annealed 70/30 and 70/50 structures are 2.5X and 2.7X respectively. Although the hole mobility enhancement factors are comparable for these two structures, the Ge diffusion is very different. Because of the higher biaxial compressive strain, structure 70/30 has

significantly more Ge diffusion than structure 70/50. When Ge reaches the oxide/Si interface, it degrades oxide quality by introducing interface states. Taking this into account, structure 70/50 is a preferred compared to structure 70/30 due to the reduced Ge diffusion through the Si capping layer during annealing.

4.5.2 Interdiffusion during RTA

As mentioned in Section 3.3, the experiments of this work were carried out using furnace anneals to obtain accurate and repeatable diffusion temperatures. However, RTA is the industry standard thermal processing technique. Interdiffusion behavior during RTA may not agree with furnace annealing due to transient diffusion effects, as RTA time is normally less than a minute, much shorter than typical furnace anneals. Whether the D_R-D_C model based on furnace anneals can apply to RTA is a question.

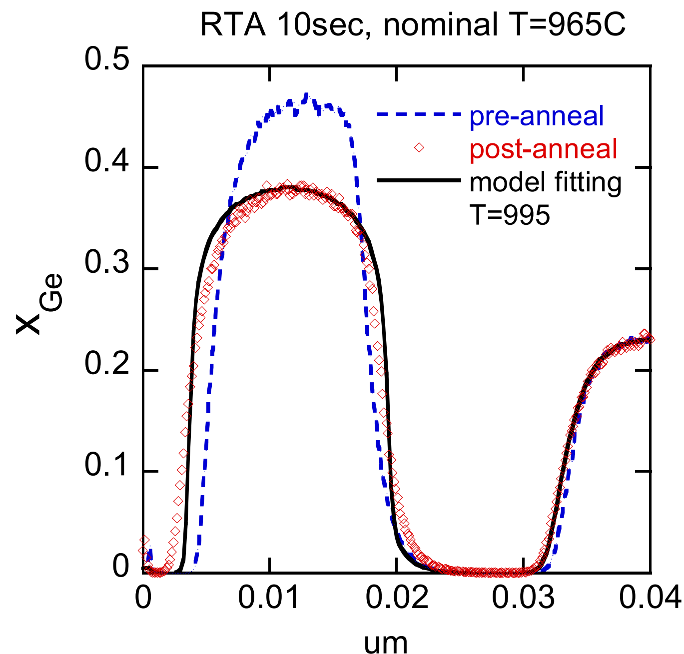

Figure 4-22 Measured Ge SIMS profiles for a HOI structure annealed by RTA compared with the interdiffusion model simulation. SIMS data courtesy of I. Aberg.

To consider the application of the model to RTA data, SIMS data from Ingvar

Aberg obtained on bulk strained Si/strained SiGe/strained Si structures (designed to emulate HOI device structures) are compared with the D_R-D_C model fits in Figure 4-22. The HOI structure in Figure 4-22 is on a relaxed 23% SiGe virtual substrate, and the as-grown SiGe peak has 46% Ge. The nominal RTA annealing condition was 965 ºC for 10 sec, much shorter than the furnace anneals used in this work, which are at least 30 min long. After the RTA, the peak height dropped from 46% to 38%. The D_R-D_C model in Equation 4-5 and 4-7 was used to fit the post-annealed profile by TSUPREM-4, with the annealing temperature taken as the fitting parameter. The best fit is obtained for a temperature T = 995 ºC, which is within 30ºC of the nominal annealing temperature. Considering that the RTA used in Aberg's work was not calibrated to within ~ 50ºC, the D_R-D_C model does a reasonable job of predicting the profile, within the RTA temperature uncertainty. Future work needs to be done to calibrate the RTA annealing temperature, and to adjust the D_R-D_C model for application to RTA.

4.5.3 Implant Damage Enhanced Interdiffusion

Another important application for the interdiffusion model is to investigate implant damage enhanced interdiffusion, which was introduced and discussed in Chapter 2. In source/drain and extension regions of SiGe MOSFETs, dopants are introduced by ion implantation. The resulting implant damage can enhance Si-Ge interdiffusion significantly. This is not desirable since interface traps form when Ge diffuses to the oxide/Si interface, and these traps may increase trap-assisted tunneling leakage in the drain/gate overlap region [64].

In order to study implant damage enhanced interdiffusion quantitatively, it is important to extract the implant enhancement factor. To illustrate such an extraction,

SIMS data from Cait Ni Chleirigh's work on dual-channel MOSFETs, subjected to 800ºC-10sec. source/drain annealing, was used [65]. Figure 4-23 shows the post-annealed SIMS Ge profile with boron implant damage, and the assumed as-grown Ge profile (SIMS data are not available for the as-grown sample). The as-grown structure has a 57A thick strained Si capping layer, which is estimated from the C-V measurement and simulation by Cait Ni Chleirigh. At the surface, Ge pile-up is not evident. Therefore, little loss in Ge dose is assumed. To generate the as-grown step profile, the thickness of the $Si_{0.4}Ge_{0.6}$ layer is adjusted to match the Ge dose of the post-annealed SIMS profile as seen in Figure 4-23. From the D_R-D_C model simulation, if the RTA temperature is accurate, no observable diffusion is expected for this dual channel structure without boron implant for 800 ºC 10 sec RTA. In this work, the implant diffusivity enhancement factor is defined as the ratio between $D_{implant}$ and $D_{unimplanted}$:

$$f_{implant} \equiv \frac{D_{implant}(x_{Ge})}{D_{unimplanted}(x_{Ge})} \qquad \text{Equation 4-16}$$

TSUPREM-4 simulations were used to find the Ge diffusivity enhancement parameter $f_{implant}$ which gives the best fit to the SIMS profile.

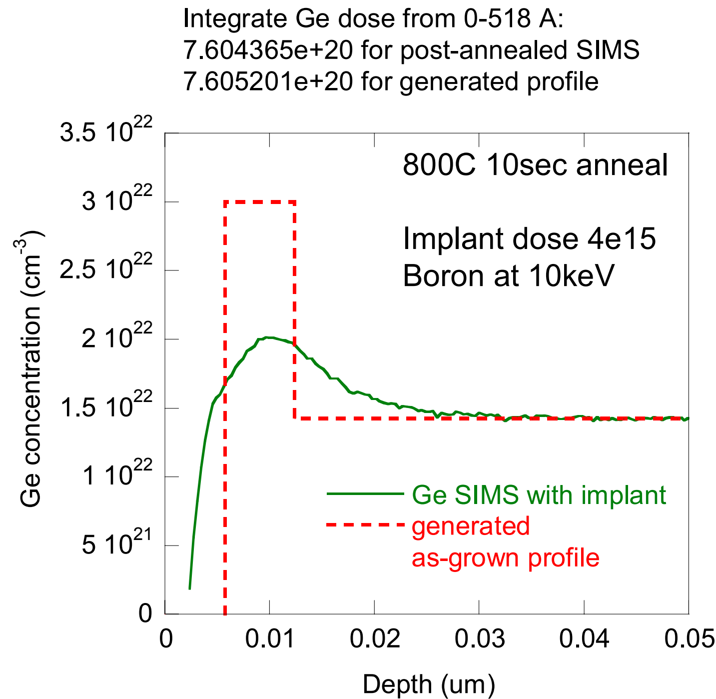

Figure 4-23 Post-annealed SIMS data for a dual-channel MOSFET source/drain region with boron implant. The dual-channel MOSFET structure is a 60A strained Si/ $Si_{0.4}Ge_{0.6}$/ relaxed $Si_{0.7}Ge_{0.3}$. The dashed line is generated to emulate the as-grown Ge profile based on CV measurement and thickness calculation. The Ge dose (area under curve) is the same for both profiles.

Figure 4-24 shows the fitting profiles with different values of $f_{implant}$ = 1000, 3000 and 5000, among which $f_{implant}$ = 3000 gives the best fit. Therefore, the implant damage enhancement factor for the Ge diffusivity is estimated to be on the order of 1000 in this example.

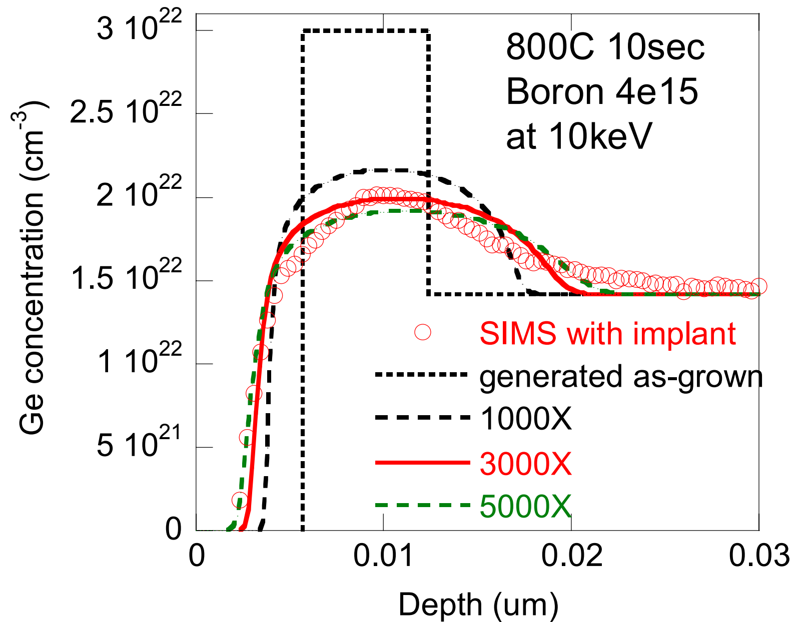

Figure 4-24 TSUPREM-4 fitting curves to the post-annealed SIMS profile in Figure 4-23. (a) $f_{implant}$ = 3000 (b) $f_{implant}$ = 5000 (c) $f_{implant}$ = 1000.

4.6 Summary of Chapter 4

After introducing the experimental method and results of the Boltzmann-Matano analysis in Chapter 3, the detailed diffusivity modeling has been discussed in Chapter 4, which is the largest contribution of this thesis. This chapter began with the SiGe interdiffusivity results for strained Si/relaxed SiGe structures, which display an exponential dependence on the local Ge fraction, x_{Ge}. The process simulation program, TSUPREM-4 was used to refine the interdiffusivity results obtained from Boltzmann-Matano analysis, in order to fit the post-annealed SIMS peak profiles. The refined interdiffusivity for strained Si/relaxed SiGe structures, D_R is shown to increase by 2.2X for every 10% increase in x_{Ge}, and by 4 to 5X for every 40 ºC increase in temperature. After that, the impact of compressive strain on the interdiffusivity was studied in detail.

Significantly enhanced interdiffusivity, D_C is observed for SiGe under biaxial compressive strain ε_C. D_C increases by 4.4X for every 0.42% increase in magnitude of compressive strain, which is equivalent to a 10% decrease in the substrate Ge fraction, x_0. A piece-wise continuous exponential model ("the D_R-D_C interdiffusivity model") that fits the observed diffusion profiles for a variety of composition and compressive strain cases, with peak Ge concentrations in the range of 55%, was constructed.

In Section 4.3, SiGe interdiffusion mechanisms were discussed. Results from the literature are consistent with the interpretation that biaxial compressive strain in the SiGe may enhance the vacancy concentration and thus increase the interdiffusivity. However, further work is needed to understand the details of the mechanism. In the data presented in this work, the strain-enhancement to the diffusivity was modeled as a change in the diffusivity pre-factor, rather than the activation energy. The small temperature range used in this strain study prevents distinguishing these two cases. In Section 4.4, the D_R-D_C interdiffusivity model was shown to apply to the case where SiGe diffuses into SiGe surrounding layers with a wide range of Ge compositions. A threading dislocation density on the order of 10^7 cm^{-2} was shown to have little effect on the major interdiffusion properties for relaxed Si/compressive $Si_{0.7}Ge_{0.3}$/relaxed Si structures. In the last section, several examples were given on the application of this work including the model application to RTA, and the design of Ge fraction and strain to minimize Ge outdiffusion in HOI and dual-channel MOSFETs.

CHAPTER 5 Summary and Future Work

5.1 Summary and Major Contributions of this Thesis

As complementary metal-oxide-semiconductor field-effect transistors (MOSFETs) scale, strained Si and SiGe technology have received more attention as a means of enhancing performance via improved carrier mobility. One of the biggest challenges for strained Si and SiGe technology is Si-Ge interdiffusion during thermal processing.

Two different aspects of Si-Ge interdiffusion are explored in this work. The first part of this work demonstrated that Si-Ge interdiffusion and ion implantation damage during the fabrication of strained Si MOSFETs have significant impact on electron mobility and thus device performance. Long channel n-MOSFETs with different thermal processing and implant conditions were fabricated on both CZ Si wafers and strained Si/relaxed $Si_{0.8}Ge_{0.2}$ heterostructures. In order to avoid scattering by ionized dopant impurities, neutral Si and Ge were implanted into the channel at six different doses ranging from 4 x 10^{12} cm^{-2} to 1 x 10^{15} $atoms/cm^2$. Three different rapid thermal anneals (RTA) were used. It is shown that the mobility enhancement factor is degraded by RTA and ion implantation. For each RTA condition, there is a threshold implantation dose, above which the strained Si mobility starts to degrade significantly. The degradation is larger for devices with larger thermal budgets or implantation doses. Si-Ge interdiffusion at the strained Si/relaxed $Si_{0.8}Ge_{0.2}$ interface was found to be the major mobility degradation mechanism for devices with higher thermal budget, while for devices with lower thermal budget, residual ion implantation damage in the strained Si channel is considered to be the key degradation mechanism. Two-dimensional simulations are performed to generate as-implanted damage profiles of 30-nm scale MOSFETs. By comparing the 2D damage

profiles with those generated by Si blanket implant, it is shown that 30-nm p-MOSFET is more likely to suffer from mobility degradation than n-MOSFETs.

The second part of this work, which is the main focus of this thesis, systematically investigated the Si-Ge interdiffusivity in epitaxial strained Si/$Si_{1-y}Ge_y$/strained Si/relaxed $Si_{1-x}Ge_x$ and strained Si/relaxed $Si_{1-x}Ge_x$ heterostructures for Ge fractions between 0 and 0.56 over the temperature range of 770 – 920 ºC. Based on the interdiffusivity extracted from experiments, an analytic model was established for interdiffusion simulation. To the best of our knowledge, this work is the most complete study of Si-Ge interdiffusion and modeling to date.

Boltzmann-Matano analysis was applied to extract interdiffusivity from the diffused Ge profiles of strained Si/relaxed $Si_{1-x0}Ge_{x0}$ heterostructures, which was later refined by TSUPREM-4 simulations. Si-Ge interdiffusivity was found to increase by 2.2X for every 10% increase in Ge fraction for interdiffusion under relaxed strain. Significantly enhanced Si-Ge interdiffusion was observed in $Si_{1-y}Ge_y$ layers under biaxial compressive strain. Si-Ge interdiffusivity was found to increase by 4.4X for every 0.42% increase in the magnitude of compressive strain, which is equivalent to 10% decrease in the substrate Ge fraction x_0. These results were incorporated into an interdiffusion model that successfully predicts the interdiffusion of various SiGe heterostructures. Examples of the impact of interdiffusion on device design and process integration issues were given.

The contributions of this work include the following:

1. Explored the correlation between processing factors such as implant damage and RTA and the device performance of strained-Si n-MOSFETs. Characterized the electron mobility degradation upon ion implant and thermal processing in strained Si n-

MOSFETs.

2. Determined the critical doses for Si implants for typical RTA conditions, above which significant electron mobility degradation occurs.

3. Demonstrated that the as-implanted damage and Si-Ge interdiffusion are possible mechanisms for the electron mobility degradation under low and high thermal budgets.

4. Used simulations to show that 30-nm node strained Si p-MOSFETs may potentially suffer from mobility degradation from implant damage and annealing.

5. Introduced and calibrated the Boltzmann-Matano method in Si-Ge interdiffusion study and demonstrated that it is an effective tool to study Si-Ge interdiffusion.

6. Systematically quantified the Si-Ge interdiffusivity for Ge fractions from 0 to 0.56 in the temperature range of 770-920 ºC in device-related structures.

7. Demonstrated significantly enhanced interdiffusion for structures with SiGe layers under compressive strain.

8. Constructed the interdiffusivity D_R-D_C model for strained Si/relaxed SiGe and strained $Si/Si_{1-y}Ge_y$/strained Si/relaxed $Si_{1-x}Ge_x$ with compressive strain that generates good fits to experimental data.

9. Demonstrated examples of the use of the D_R-D_C model in RTA diffusion, device design and implant-enhanced interdiffusion.

5.2 Suggestions for Future Work

There are a number of remaining issues to be investigated in the area of Si-Ge interdiffusion. Below are a few suggestions for further study:

1. Si-Ge interdiffusion in Ge-rich alloys ($x_{Ge} > 0.5$). In this thesis work, the focus was on SiGe layers with Ge fraction less than 0.56. Interdiffusion models for high Ge content materials will be very helpful for devices with pure Ge or Ge rich materials such as Ge-on-insulator MOSFET fabricated by layer transfer technique, Ge on Si photodetectors and modulators. Boltzmann-Matano analysis described in this work should apply to the range where Ge fraction is larger than 0.5. A difficult issue is the growth of high content Ge or pure Ge diffusion couple structures for Boltzmann-Matano analysis, within the constraints imposed by the critical thickness and SIMS broadening effects.

2. Residual non-locality of the D_R-D_C model. In the Ge SIMS profiles, especially those on 56% or 45% substrate, the foot or tail appears to be diffusing faster than the local D_R-D_C model would suggest. These foot or tail regions are potentially under a lot of tensile stress, since they differ the most from the Ge fraction of the peak or shoulder. It is possible that the foot or tail region is slightly relaxing, making the diffusivity higher than the calculation from the D_R-D_C model. Or there may be a second-order effect here that the D_R-D_C model has not yet captured, such as pipe diffusion through misfit dislocations. Although the low Ge fraction diffusion has little impact on the peak drop, the main focus of the D_R-D_C model, it is important in determining the oxide interface quality as Ge diffuses in the strained Si cap layer, and the Ge tail approaches the oxide. This is an important topic for future work.

3. Calibration of the D_R-D_C model for RTA applications. This thesis work was based on furnace annealing as it provides more accurate and repeatable diffusion

conditions than RTA. As mentioned in the latter part of Chapter 4, RTA is the industry standard thermal processing technique. It would be very helpful to calibrate RTA and fine tune the D_R-D_C model for RTA applications. This will also provide some information on the time dependence of Si-Ge interdiffusion.

4. Tensile strain impact on Si-Ge interdiffusion. In this work, the tensile strain impact was discussed using indirect evidence in Section 4.1.5. Besides the discussion in Section 4.1.5, a 30/60 structure (s-Si/$Si_{0.7}Ge_{0.3}$/s-Si on relaxed $Si_{0.7}Ge_{0.3}$) was designed to observe tensile strain effect on interdiffusion. The top three layers of 30/60 structure are each about 100 A thick, so that SIMS can resolve Ge peaks without significant artifact. It was found that the top three layers are too thick to retain the target tensile strain. From Raman measurement, the as-grown $Si_{0.7}Ge_{0.3}$ peak is already 50% relaxed, and is fully relaxed after annealing. Therefore, this approach was not successful to observe tensile strain impact on interdiffusion, and alternative approaches should be explored.

5. Si-Ge interdiffusion mechanisms require more study. Most researchers agree that Ge diffusion is mediated by a vacancy mechanism more than by interstitials at low Ge concentration ($x_{Ge} < 0.3$). However, as Ge diffuses into Si, Si also diffuses into Ge, which is "Si-Ge interdiffusion", as distinct from Ge diffusion. Generally interdiffusivity is the weighted sum of the intrinsic diffusivity of both elements: $D_{inter} = xD_{Si} + (1-x)D_{Ge}$. So far, the role of Si in the interdiffusion, the individual terms D_{Si} and D_{Ge} and their corresponding activation energies are still unclear.

6. Determine the origin and the strength of biaxial strain coupling factor Q' and Ge concentration dependence, which are still areas of controversy. The definition of Q' factor is based on the exponential dependence of diffusivity on biaxial

strain: $D(\varepsilon_{biax})/D(0)=\exp(-\frac{\varepsilon_{biax}*Q'}{kT})$, where Q' changes the activation energy of diffusion. This has shown to be suitable for dopant diffusion and low Ge content diffusion [49] [66]. In SiGe interdiffusion, exponential dependence is also seen in the case of interdiffusion under compressive strain. However, it is not clear whether this dependence is due to a change in the activation energy *Ea* or a change in the entropy *S* in the D_0 term or both. The work in the literature is mostly on low Ge alloys with $x_{Ge} < 0.3$ and the strain dependence is treated as a change in *Ea* term. However, there is a large scatter in the reported strength of that dependence. Table 5-1 below shows a summary of the biaxial strain coupling factor Q' and x_{Ge} dependence from various references. For the dependence of the interdiffusivity on x_{Ge}, there is reasonable consistency between reported results and the results of this work. However, the reported Q' dependence shows a wide range of values. More work needs to be done to determine the origin of the strain dependence and resolve these discrepancies. One possible method to obtain a more accurate *Ea* using a wide temperature range is discussed in Section 4.2.4.

7. On the theoretical side, it will be helpful to develop thermodynamic treatment and microscopic process that explain biaxial stress effects on Si-Ge interdiffusion. M. J. Aziz et al. summarized experimental results and theoretical treatment on Q' for Sb and B diffusion in Si and SiGe, with theoretical prediction consistent with Sb experimental results, but inconsistent with B results [66]. P. Ramanarayanan et al. relate the macroscopic dopant diffusion activation energy change with microscopic migration energy change under stress [67]. In Si-Ge interdiffusion, the matrix is no longer the Si lattice, but a Si-Ge alloy with composition that is changing during diffusion. This makes it difficult to use a nearest neighbor approach in the theoretical treatment. However, the

dopant diffusion work provides a useful reference and a starting point for theoretical analysis of Si-Ge interdiffusion.

Source	Structure	Conditions	Q' (eV/ unit strain)	*D* change (every10% x_{Ge})
N. B. Cowern PRL 1994	Si/compressive 10-30% Ge 200-1200A/Si	900-1050ºC N_2, 4mins-4 hour	40±5	insignificant concentration effect
Cowern 1996 4th Symposium on Process Physics and Modeling	Si/ 300-400A compressive 30% SiGe /relaxed Si, s-Si/300-400A relaxed 30% SiGe/s-Si on graded buffer	875ºC 2hours in N_2, 1% O_2 and 100% O_2	$Q'_{(v)}$= =17.8±4.3 (Vacancy) $Q'_{(i)}$= = -12.0±8.0 (Interstitial)	3.3X
Aubertine JAP 2005	Superlattice on Si	700-870ºC in N_2	0	1.3~1.7X
Zangenberg 1999	Ge self diffusion	850-1050ºC under capping layer, effective inert ambient	160±40	3~4X
This work	**heterostructure on bulk type structure (similar to HOI)**	**770-840ºC in N_2**	**32±4**	**2.2X**

Table 5-1 Summary of the biaxial strain coupling factor Q' and x_{Ge} dependence for SiGe interdiffusion under biaxial stress.

As these topics are explored in the future, questions and comments are very welcome, and can be sent to grxia@alum.mit.edu.

Appendix A Example of Source Code for Electron Mobility Calculation.

1) Main Program used to calculate mobility:
filename: calcuH4_100a for wafer 420.7

```
% this program load IV, Cgc, Cgb data, calculate
% gm, Eeff, Qb, Qinv, tox, mobility etc
% x is the concentration of Ge
% the reason why this code is called long is because this one
% give Qb a value and compare that to universal
close all;
clear all;

readme=[
'|  Ion implant damage projetc                      |'
'|  Temperature =  300 K:                           |'
'|  Uses C-V for Qinv, Cmin is the cross point      |']
testID='---- 420.7 die H4 100a'

esi=11.9;  eox=3.9; e0=8.854e-12; ege=16; q=1.6e-19; dV=0.05;
%%%%%%%%%%%%%%%% constant, see thesis P89
x=0.2; % for CZ wafer
ealloy=(x*ege+(1-x)*esi)*e0;
% all the parameters are defined in SI
Na=2.5e17;

w=100e-6;
l=100e-6; % SI
%w = input('What is the gate width, w, in micrometers? ')*1E-6;
%l = input('What is the gate length, l, in micrometers? ')*1E-6;
load R2.txt; % IV
load RC14.txt; % the Cgc file
load RC15.txt; % Cgb file
IVfile=R2;
Cgcfile=RC14;
Cgbfile=RC15;
V=[-1:0.05:2];

%%%% above parameters may need to change for different devices and wafers %%%%
dl=length(V);
x=[-0.025:0.01:0.025];
Vd=[-3e-2:0.01:0.03];
% 7 curves this time
```

```
for i=1:length(x)+1
  ID(:,i)=IVfile((dl*i-(dl-1)):i*dl,3);
  %Id is the 3th column in the data file
end

for i=1:length(x)
  g(:,i)=(ID(:,i+1)-ID(:,i))/0.01;
end

for i=1:length(V)
  %y=ID(i,:);
  %gd(i)=(sum(y)*sum(Vd)-y*Vd')/(sum(Vd)^2-Vd*Vd');
  value=polyfit(x,g(i,:),1);
  gd(i)=value(2);
  if i<=20
     gd(i)=0;
  end
end
% use polyfit to get gd

% caculate gm
for i=1:length(Vd)
  temp(1,i)=0;
  temp(2:dl,i)=ID(1:(dl-1),i);
  gm(:,i)=(ID(:,i)-temp(:,i))/dV;
end

dispiv(testID,V,ID,gd,gm,w,l);

%%%%%%%%%%%% CV characteristics below %%%%%%%%%%%%%%%

Vgatei=Cgcfile(:,1);
t1=Cgcfile(1:12,2);
Cgc=(Cgcfile(:,2)-sum(t1)/12)/w/l*1e8;
%%%%%%%%%%%%%%%%%%%% move Cgc to zero
% Cgc in F

[y,I]=max(Cgc);
for i=1:length(Cgc)
  if (Cgc(i)<0)
    Cgc(i)=0;
  end
  % offset Cgc to zero

  %if (i>I)
   % Cgc(i)=y;
```

```
  %end
  % correction for poly-depletion
end

Vgateb=Cgbfile(:,1);
t2=Cgbfile((length(Vgateb)-6):length(Vgateb),2);
for i=1:length(Vgateb);
  Cgb(i)=(Cgbfile(i,2)-sum(t2)/7)/w/l*1e8;
      %%%%%%%%%% Cgb is in F
end

% Cgc, Cgb are the capacitance per area, pF/cm2, F/m2=1e8pF/cm2

Vmi=-1:dV:1;
if min(Vgateb)==-2
   temp1=20;
end

if min(Vgateb)==-3
   temp1=40;
end

for i=1:length(Vmi)
  Ct(i)=Cgb(temp1+i)+Cgc(i); %%%%%%%%
end

%********* Visually find Cmin from Cgb

done='n';
one=ones(1,41);
figure;
while done == 'n',
  Cmin = input('What is the Cmin in pf? ')/w/l*1e8*1e-12;
  % change Cmin from pf to F/cm2 by *1e-12
        plot(Vgatei,Cgc*w*l*1e-8,'r',Vgateb,Cgb*w*l*1e-8,'b',Vmi,Ct*w*l*1e-8,'k',[-
1:0.1:3],Cmin*w*l*1e-8*ones(1,41),'-');
  title(['Cgc/Cgb/C vs Vg  ',testID]);
  legend('Cgc','Cgb','Ctotal');
  xlabel('Vg  (V)');
  ylabel('C F');
  grid on;
        done = input('Done? ','s');
end;

disp('Cmin= (pF)');
disp(Cmin*w*l*1e4);
Vt = input('What is Vt? ');
```

```
figure;
plot(Vgatei,Cgcfile(:,2),'r',Vgateb,Cgbfile(:,2),'b');
legend('Cgc','Cgb');
xlabel('Vg  (V)');
ylabel('C F');
title(['raw data Cgc, Cgb  ',testID]);
grid on;


figure;
plot(Vgatei,Cgc,'r',Vgateb,Cgb,'b',Vmi,Ct,'k');
title(['Cgc/Cgb/C per area vs Vg  ',testID]);
xlabel('Vg  (V)');
ylabel('C pF/cm2');
legend('Cgc','Cgb','Ctotal');
% plot Cgc vs Vgatei and Cgb vs Vgateb;
% F/m2=1e8pF/cm2
grid on;

%%%%%%%%%%%%%%%%%%%%   Qinv   %%%%%%%%%%%%%%%%%%%%%

Qinv(1)=0;
for i=2:length(Cgc)
  Qinv(i)=Qinv(i-1)+(Cgc(i)+Cgc(i-1))*1e-8*dV/2; % in SI
end

Cox=max(Cgc);
% how to do the average of the curve???
tox=eox*e0/(Cox*1e-8);
Cd=Cmin*Cox/(Cox-Cmin);
Xd=ealloy/(Cd*1e-8); % here I use the esi*e0, Xd in SI
Qb=Na*Xd*1e6*q;  % ******* doping is about 1e17cm-3, change that into
Qb***********

for i=1:1:dl %%%%%%
  Eeff(i)=(Qb+Qinv(i)/2)*1e-8/(ealloy);
  % the relative dielectric constant, use ealloy
end
%MV/cm=1e8V/m

%%%%%%%%%% Qb part in file Qb.m %%%%%%%%%%
for i=18:dl
   if Qinv(i)/q*1e-4 >5e10
  Ueff(i)=l*gd(i)/w/Qinv(i)*1e4;
```

```
    else
    Ueff(i)=0;
    end
end

% note Qinv(i)=0, not taken into account;
% m2/V/s=1e4 cm2/v/s

for i=1:dl
        Ufe(i,:)=(l/w/(Cox*1e-8))*(gm(i,:)./Vd)*1e4;
end
% m^2/V/s=1e4cm^2/v/s

plot0(V,Eeff,testID,Qinv,Ueff, Ufe,Vgatei,q);
compareU(Eeff,Ueff,testID);
readme
fprintf('Vt=  %6.2f (V)\n',Vt);
fprintf('Na=  %6.2e \n',Na);
dispall(Cmin,w,l,Cox,gd,gm,Xd,tox,Qinv,q,Qb,Ueff,Eeff,testID,Vt);


for n=1:20
    Ctot(n)=Cgb(n);
end
for n=21:length(Cgb)
    Ctot(n)=Cgb(n)+Cgc(n-20);
end

Ctot=Ctot'.*1e-4;
figure;
plot(Vgateb,Ctot);
title('Ctot vs Vgate in pF');
grid;

save Ctot.txt Ctot -ASCII;
```

2) Program used to plot figures:

```
function plot0(V,Eeff,testID,Qinv,Ueff, Ufe,Vgatei,q)

figure;
plot(V,Eeff);
title(['Eeff vs Vg  ',testID]);
xlabel('Vg  (V)');
ylabel('Eeff  (MV/cm)');
grid on;
```

```
figure;
plot(Qinv/q*1e-4,Ueff,Qinv/q*1e-4,Ufe);
grid on;
title(['Ueff and Ufe vs Qinv  ',testID]);
ylabel('Ueff Ufe cm^2/v/s  ');
xlabel('Qinv carriers/cm2 ');
%legend('Ueff','@ Vds=-20mV','@ Vds=-10mV','@ Vds=0mV','@ Vds=10mV','@
Vds=20mV');

figure;
plot(V,Ueff,V,Ufe);
grid on;
title(['Ueff and Ufe vs Vgate  ',testID]);
ylabel('Ueff Ufe cm^2/v/s  ');
xlabel('Vg V ');
%legend('Ueff','@ Vds=-20mV','@ Vds=-10mV','@ Vds=0mV','@ Vds=10mV','@
Vds=20mV');


figure;
plot(Vgatei,Qinv/q*1e-4);
title(['Qinv vs V   ',testID]);
% do the integration, plot Qinv vs Vgatei;
xlabel('Vg  (V)');
ylabel('Qinv carriers/cm2');
grid on;


figure;
plot(Qinv/q*1e-4,Ueff,'*');
grid on;
title(['Ueff vs Qinv  ',testID]);
ylabel('Ueff cm^2/v/s  ');
xlabel('Qinv carriers/cm2 ');

figure;
plot(Qinv/q*1e-4,Ufe);
grid on;
title([' Ufe vs Qinv  ',testID]);
ylabel(' Ufe cm^2/v/s  ');
xlabel('Qinv carriers/cm2 ');

figure;
plot(Eeff,Ueff);
```

```
title(['Ueff vs Eeff  ',testID]);
ylabel('Ueff cm^2/v/s  ');
xlabel('Eeff  (MV/cm)');
grid on;

figure;
plot(Eeff,Ufe);
legend('@ Vds=-30mV','@ Vds=-20mV','@ Vds=-10mV','@ Vds=0mV','@
Vds=10mV','@ Vds=20mV','@ Vds=30mV');
title(['Ufe vs Eeff  ',testID]);
ylabel('Ufe cm^2/v/s  ');
xlabel('Eeff  (MV/cm)');
grid on;

figure;
plot(Eeff,Ueff,'k',Eeff,Ufe);
title(['Ueff and Ufe vs Eeff  ',testID]);
legend('Ueff');
%legend('Ueff','@ Vds=-20mV','@ Vds=-10mV','@ Vds=0mV','@ Vds=10mV','@
Vds=20mV');
ylabel('Ueff cm^2/v/s  ');
xlabel('Eeff  (MV/cm)');
grid on;
```

3) Program used to display the key results:

```
function dispall(Cmin,w,l,Cox,gd,gm,Xd,tox,Qinv,q,Qb,Ueff,Eeff,testID,Vt)

fprintf(testID);
fprintf('\nCmin= %6.2f (pF) \n',Cmin*w*l*1e4);
fprintf('Cox/area= %6.2e (F/cm2)  \n',Cox);
fprintf('max(gd)= %6.2e(S)  \n',max(gd)/(w/l));
fprintf('max(gm)= %6.2e(S)   \n',max(gm(:,5))/(w/l));
fprintf('Xd= %6.2f (A)  \n',Xd*1e10);
fprintf('tox= %6.2f (A)  \n',tox*1e10);
fprintf('maxQi= %6.2e(carriers/cm2)  \n',max(Qinv)/q*1e-4);
fprintf('Qb= %6.2e(carriers/cm2)  \n',Qb/q*1e-4);
fprintf('max Ueff= %6.2f(cm2/v sec)  \n',max(Ueff));


fid = fopen('output.txt','w');
fprintf(fid,testID);
fprintf(fid,'\nCmin= %6.2f (pF) \n',Cmin*w*l*1e4);
fprintf(fid,'Cox/area= %6.2e (F/cm2)  \n',Cox);
fprintf(fid,'max(gd)= %6.2e(S)  \n',max(gd)/(w/l));
```

```
fprintf(fid,'max(gm)= %6.2e(S)   \n',max(gm(:,5))/(w/l));
fprintf(fid,'Xd= %6.2f (A)  \n',Xd*1e10);
fprintf(fid,'tox= %6.2f (A)  \n',tox*1e10);
fprintf(fid,'maxQi= %6.2e(carriers/cm2)  \n',max(Qinv)/q*1e-4);
fprintf(fid,'Qb= %6.2e(carriers/cm2)  \n',Qb/q*1e-4);
fprintf(fid,'max Ueff= %6.2f(cm2/v sec)  \n',max(Ueff));
fprintf(fid,'Vt= %6.2f(V)  \n',Vt);

fclose(fid)



Ueff1=Ueff';
save mobility.txt Ueff1 -ASCII;
Eeff1=Eeff';
save Eeff.txt Eeff1 -ASCII;
Qinv1=Qinv'/q*1e-4;
save Qinv.txt Qinv1 -ASCII;
gd1=gd';
save gd.txt gd1 -ASCII;

% save the mobility result to the result folder, all the vables to its own directory
```

Appendix B Fabrication Steps of Strained Si *n*-MOSFETs.

Implant splits:

1) 4 Si implant splits ranging from 4e12 to 5e14 cm $^{-2}$
2) 2 Ge implant splits ranging from 4e12 to 5e14 cm $^{-2}$
3) no implantation

RTA splits:

1) 1000°C for 1 sec
2) 1000°C for 10 sec
3) 950°C for 10 sec

wafer splits:

1) 10 strained Si wafers
2) 9 CZ control wafers

Reoxidation splits:

1) wafer 420.10 has no reoxidatioin.

1) Zero Alignment Marks (etch 1-1.5 μm of Si/SiGe)

- Lithography: Mask CA
- AME5000 (recipe Hasansil- ~92 A/sec) to etch alignment marks
- Asher

2) Field ion implantation

- Lithography: Mask CF (block materials dies)
- ion implantation B11, dose 3e13 cm^{-2}, energy 25 keV, 7 degree tilt, 0 rotation

3) Field Oxide

- 2 p-cleans
- rca clean (SC1 substituted with p-clean)
- LTO deposition (~3000 A)
- Lithography: MASK CD to open active area (clear materials dies)
- AME5000 etch (HASANFOX ~20 A/sec) to dry etch ~2500Å LTO
- Image the LTO using the SEM (NSL)
- Asher

- Wet etch 50:1 HF to etch ~1200Å LTO

4) Body Implants

- ion implantation splits- see implant splits

5) Gate Stack (45 A SiO_2/1500 A poly-Si)

- 45 A gate oxide: tube A1. rec 144, time 30mins
- 1500 A poly: tube A6 rec 461, T=25mins

6) Gate Etch

- Lithography (mask CP) (clear surface analysis and S/D blank die, leave poly on gate blank die)
- Etch poly-Si: AME50000 (rec: KEITH CP)
- Image gate etch and poly stringers (SEM)

7) Reoxidation

- rca clean
- 11mins at 800 ^{o} C in dry O2 ambient. Rec: 800°C REOX

8) Deep S/D and poly-Si I/I

- use resist to block surface analysis dies
- 10 keV, 5e15 cm^{-2} Phosphorus, 0 tilt, 0 rotation (SIMS was used to check the P diffusion)

9) Clear backside

- Hardbake frontside with photoresist
- Etch 30Å reox/1500Å poly/45A gate oxide using BOE dip and AME5000 (rec Tony_LTO) to remove oxide and poly
- asher

10) RTA

- 2 p-clean
- RCA with no HF dip
- 3 RTA splits (rec: mg1000b and mg950)

11) Contact Cuts

- rca clean
- deposit ~2500 A LTO
- lithography (mask CC) (leave LTO on materials dies for metal etch)

- AME5000 (rec Hasanfox) to etch 1750Å LTO.
- remove remaining 1200 LTO wet etch 50:1 HF (overetch so that LTO on poly-Si is removed)
- asher

12) Metal Deposition and etch

- P-clean and HF dip (remove native oxide)
- 1000 A Ti/ 1 μm Al sputtering using ENDURA
- lithography (Mask CM) (clear materials dies)
- wet etch metal using PAN etch to remove Al and 50:1 BOE to remove Ti
- asher
- sinter in TRLtube A3, forming gas 35~40mins

Appendix C Example of Source Code for MEDICI Simulations of C-V.

Filename: SS20M.inp

```
$ this structure is for long channel Strained Si nMOSFET

assign  name=polydope         n.val=8e19
assign  name=welldope   n.val=3.7e17

$ physical dimensions
assign  name=Lgate    n.val=100.0
assign  name=Lsd      n.val=9
$ source drain are too narrow to show up in the figures <0.1 um
assign  name=Tpoly    n.val=0.150
assign  name=Tlto     n.val=0.025
assign  name=Tox      n.val=0.0046
assign  name=Tsi      n.val=0.200

$ tags
assign  name=xmin     n.val=-@Lgate/2-@Lsd
assign  name=xmax     n.val=@Lgate/2+@Lsd
assign  name=ymin     n.val=-@Tox-@Tpoly
assign  name=ymax     n.val=@Tsi

assign name=T.CAP  n.val=0.010
$ thickness of strained Si, 100Å
```

```
assign name=T.PCH  n.val=0.010
assign name=T.BOT  n.val=0.010

assign name=Y1           n.val=@T.CAP
assign name=Y2           n.val=@Y1+@T.PCH
assign name=Y3     n.val=@Y2+@T.BOT
$ ************************************************************ $

mesh RECTANGU smooth.k=1

$ lateral mesh
x.mesh x.min=@xmin width=@Lsd h1=@Lsd/3 h2=@Lsd/36
x.mesh width=@Lgate/4 h1=@Lsd/36 h2=@Lgate/10
x.mesh width=@Lgate/4 h1=@Lgate/10 h2=@Lgate/10
x.mesh width=@Lgate/4 h1=@Lgate/10 h2=@Lgate/10
x.mesh width=@Lgate/4 h1=@Lgate/10 h2=@Lsd/36
x.mesh width=@Lsd h1=@Lsd/36 h2=@Lsd/3

$ depth mesh
y.mesh y.min=@ymin depth=@Tpoly h1=@Tpoly/3 h2=@Tox/2
y.mesh depth=@Tox h1=@Tox/2
y.mesh depth=@T.CAP h1=@Y1/25 h2=@Y1/25
y.mesh depth=@T.PCH h1=@Y1/25 h2=@Y2/25
y.mesh  depth=@T.BOT h1=@Y2/25 h2=@Y3/25
y.mesh y.max=@ymax h1=@Y3/25 h2=@Tsi/5

eliminate        columns
 +        x.min=@xmin x.max=-@Lgate/2 y.min=@ymin y.max=-@Tox
eliminate        columns
 +        x.min=@Lgate/2 x.max=@xmax y.min=@ymin y.max=-@Tox

eliminate        columns
 +        x.min=@xmin x.max=@xmax y.min=@ymax/2 y.max=@ymax

$ ************************************************************ $

$ left LTO and nitride
REGION        name=4 oxide
+        x.min=@xmin x.max=-@Lgate/2 y.min=-@Tox-@Tlto y.max=-@Tox
REGION        name=4 oxide
+        x.min=-@Lgate/2-@Tlto x.max=-@Lgate/2 y.min=@ymin y.max=-@Tox
REGION        name=5 nitride
+        x.min=@xmin x.max=-@Lgate/2-@Tlto y.min=@ymin y.max=-@Tox-@Tlto

$ right LTO and nitride
REGION        name=6 oxide
```

```
+        x.min=@Lgate/2 x.max=@xmax y.min=-@Tox-@Tlto y.max=-@Tox
REGION        name=6 oxide
+        x.min=@Lgate/2 x.max=@Lgate/2+@Tlto y.min=@ymin y.max=-@Tox
REGION        name=7 nitride
+        x.min=@Lgate/2+@Tlto x.max=@xmax y.min=@ymin y.max=-@Tox-@Tlto

$CAP
REGION name=CAP  sige
+ x.min=@xmin x.max=@xmax y.min=0 y.max=@Y1

$PCHANNEL
REGION name=PCHANNEL sige
+ x.min=@xmin x.max=@xmax y.min=@Y1 y.max=@Y2

$BOTCAP sige
REGION  name=BOTCAP sige
+ x.min=@xmin x.max=@xmax y.min=@Y2 y.max=@Y3

$BUFFER
REGION name=BUFFER sige
+ x.min=@xmin x.max=@xmax y.min=@Y3 y.max=@ymax

$ gate polysilicon
region  name=1 silicon         x.min=-@Lgate/2 x.max=@Lgate/2 y.min=@ymin
y.max=-@Tox

$ gate oxide
region  name=2 oxide x.min=@xmin x.max=@xmax y.min=-@Tox y.max=0

$ ************************************************************ $

$ contacts
electrode name=drain x.min=@xmax-@Lsd/3 x.max=@xmax y.min=0 y.max=0

electrode name=gate  x.min=-@Lgate/2 x.max=@Lgate/2
+                    y.min=@ymin y.max=@ymin+@Tpoly

electrode name=source          x.min=@xmin x.max=@xmin+@Lsd/3 y.min=0 y.max=0

electrode name=bulk  bottom

$************************************************************$
$ poly doping
$profile n-type region=1 uniform n.peak=@polydope

$body doping
```

```
profile p-type uniform n.peak=@welldope

$source doping
profile n-type  n.peak=1.700000e+20
+       y.min=0.000000e+00 y.max=0.000000e+00 y.char=1.65e-02
+       x.min=@xmin x.max=-@Lgate/2 x.char=0.5e-02

$drain doping
profile n-type  n.peak=1.700000e+20
+       y.min=0.000000e+00 y.max=0.000000e+00 y.char=1.65e-02
+       x.min=@Lgate/2 x.max=@xmax x.char=0.5e-02

contact name=gate      n.polysi resistan=0
contact name=bulk      neutral resistan=0

$relaxed- Si0.8Ge0.2
material sige
+         x.mole=0.2
+         permittivity=12.73
+         eg.model=0
+         affinity=4.05
+         eg300=1.06

$strained-Si on relaxed- Si0.8Ge0.2
material region=(CAP)
+         x.mole=0
+         permittivity=11.9
+         eg.model=0
+         affinity=4.05+0.126
+         eg300=1.06-0.126+0.126

$strained- Si0.2Ge0.8 on relaxed- Si0.8Ge0.2
material region=(PCHANNEL)
 +        x.mole=0.2
 +        permittivity=12.73
 +        eg.model=0
 +        affinity=4.05
 +        eg300=1.06

$strained-Si on relaxed- Si0.8Ge0.2
material region=(BOTCAP)
 +        x.mole=0.2
 +        permittivity=12.73
 +        eg.model=0
 +        affinity=4.05
 +        eg300=1.06
```

```
plot.2d grid boundary fill

plot.1d log doping x.start=0 y.start=0 x.end=0 y.end=0.1

plot.1d log doping x.start=@xmin y.start=0 x.end=@xmax y.end=0

plot.2d x.min=@xmin x.max=@xmax y.min=0 y.max=0.1
contour doping log min=-19 max=-17 del=.1 line=1 fill=false

plot.2d ^clear x.min=@xmin x.max=@xmax y.min=0 y.max=0.1
contour doping log min=16 max=20 del=.5 line=2 fill=false
```

Appendix D Temperature profiles in furnace anneals

All the samples were annealed in dry N_2 ambient in furnace tube-B3 in TRL. The ramping up speed is about 15-17 º C/min, and the ramping down speed is about 6-7 º C/min. A typical temperature profile during anneal is shown in Figure D-1.

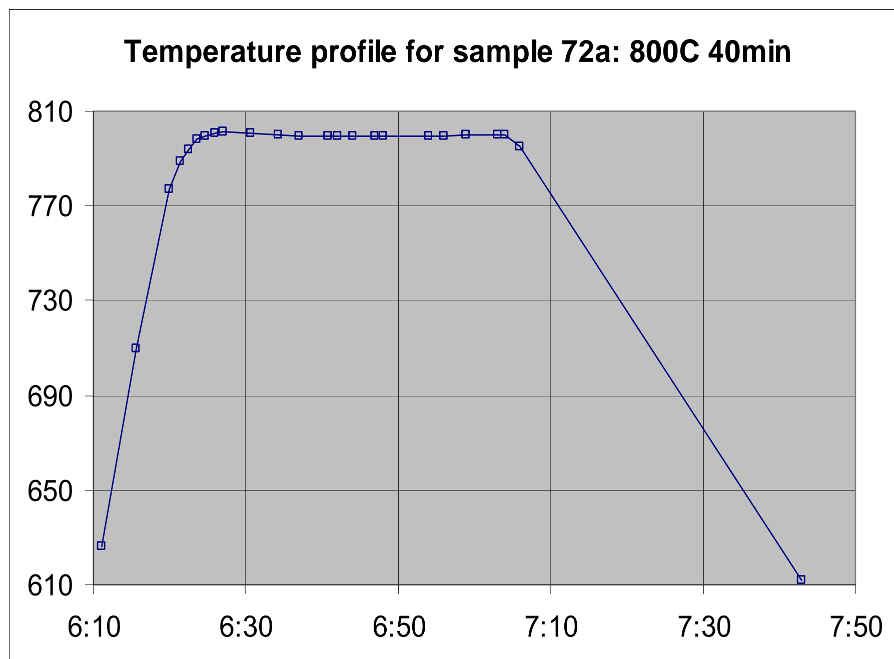

Figure D-1 A typical temperature profile for N_2 anneal in furnace tube-B3 in TRL.

Appendix E Matlab code for Boltzmann-Matano Analysis

```
% this code load fuzzy real data BM20A.txt, smooth it and do BM without interpolation
clear all;
close all;
clc;
 % load Ge profile: unit is um vs cm-3.
 load BM20A.txt;
% the format is depth in um and Ge density in cm-3

rawdata=BM20A;
fulldata=BM20A;
anneal_time=60;
%anneal time
 x=rawdata(:,1);
y=rawdata(:,2);
temp=smooth(y,3);
temp=smooth(temp,3);
 for i=1:30
temp=smooth(temp,3);
end
for i=1:30
temp=smooth(temp,3);
end
 smoothed_final=smooth(temp,5);

% ----------- smoothing is needed for real data -----------
 depth=x'*1e-4;
% now depth unit is cm, 1cm=1e4um
Cge=smoothed_final';
n=length(Cge);
figure;
plot(fulldata(:,1)*1e-4,fulldata(:,2),'b-',depth,Cge,'r-');
ylabel('Ge concentration'); xlabel('cm');
grid; legend('all data','after smoothing');

 %%%%%%%%%%% from here, only use depth and x0 %%%%%%%%%%%%%
 x0=(0.0:0.001:0.02)'*1e-4;
%x0 unit is cm
m=length(x0);
inter(1:m)=0;
for j=1:m
   for i=2:n
```

```
    dc=Cge(i)-Cge(i-1);
    s(i)=(depth(i)+depth(i-1))*dc/2;
    inter(j)=(inter(j)+s(i));
    end
inter(j)=inter(j)-x0(j)*Cge(n);
end
 % inter is a function of x0
 figure;
plot(x0,inter); xlabel('depth');ylabel('intergral');
grid; title('find x0');
x0=input('x0=  (cm):');
% -------------- need to find x0 manually ------------------
 depth=depth-x0;
 figure;
 plot(Cge,depth,'r');
title('minus x0');
grid;
 %anneal_time=input('annealing time is (min)');
 time_term=-1/2/60/anneal_time;
 % the diffusion time is 62x60 seconds

int2(1)=0;
slope(1:n)=0;
[maxCge,maxindex]=max(Cge);
% make sure the integral ends at the highest Cge

for i=2:n-1
    temp0=depth(1:i);
    dc=Cge(i)-Cge(i-1);
    s(i)=(depth(i)+depth(i-1))*dc/2;
    int2(i)=int2(i-1)+s(i);
    dc2=Cge(i+1)-Cge(i-1);
    if (dc2~=0)

       slope(i)=(depth(i+1)-depth(i-1))/dc2;
    %slope is the average slope of 3 points
    end
    D(i)=time_term*slope(i)*int2(i);
end

int2(n)=int2(n-1)+(depth(n)+depth(n-1))*(Cge(n)-Cge(n-1))/2;
% int2 is the integral from Ca=0 to C
% ======= int2(Cmax)=0 by definition??============
slope(n)=(depth(n)-depth(n-1))/(Cge(n)-Cge(n-1));
slope_raw=slope;
temp=smooth(slope,3);
```

```
for i=1:30
temp=smooth(temp,3);
end
 slope=temp;
D=time_term*slope.*int2;
figure;
subplot(1,3,1);
plot(depth,slope_raw,'x',depth,slope,'r-');
grid; axis tight;
title('slope_raw vs depth');
 subplot(1,3,2);
plot(Cge,'x');grid; axis tight;
title('Cge vs #');
subplot(1,3,3);
 plot(depth,Cge,'x');grid; axis tight;
title('Cge vs depth');
D(n)=time_term*slope(n)*int2(n);

%%%%%%%%%%% plotting %%%%%%%%%%%%%%%%%%
 figure;
plot(Cge(1:n)/5e22,int2(1:n),'-');
title('int2 vs Ge fraction');
grid; xlabel('X_G_e');ylabel('int2');

figure;
plot(int2(1:n),'x-');
title('int2 vs #');
grid; xlabel('#');ylabel('int2');

figure;
plot(depth+x0,slope(1:n),'x-');
title('slope vs depth');
grid; xlabel('depth');ylabel('slope');
figure;
plot(Cge(1:n)/5e22,abs(slope(1:n)),'x-');
title('slope vs Ge fraction'); axis tight;
grid;xlabel('X_G_e');ylabel('dx/dc');

figure;
subplot(1,3,1);
semilogy(Cge(1:n)/5e22,slope(1:n),'x-');
title('slope vs Ge fraction'); axis tight;
grid;xlabel('X_G_e');ylabel('dx/dc');
subplot(1,3,2);
plot(Cge(1:n)/5e22,int2(1:n),'-');
title('int2 vs Ge fraction');
```

```
axis tight;
grid; xlabel('X_G_e');ylabel('int2');
 subplot(1,3,3);
semilogy(Cge(1:n)/5e22,D(1:n),'x');
%AXIS([0.01 0.17 2e-18 8e-18])
 % -------------- need to give the range manually ------------------
 title('D vs Ge fraction'); xlabel('X_G_e');ylabel('D cm2/sec');
 grid;

figure;
semilogy(Cge(1:n)/5e22,D(1:n),'x');
title('D vs Ge fraction'); xlabel('X_G_e');ylabel('D cm2/sec');
AXIS([0.01 0.55 1e-18 1e-13])
axis tight;
grid;

figure;
absD=abs(D(1:n));
subplot(1,2,1)
semilogy(Cge(1:n)/5e22,absD,'x');
title('abs(D) vs Ge fraction'); xlabel('X_G_e');ylabel('D/minD cm2/sec');
axis tight;
grid;
subplot(1,2,2);
semilogy(Cge(1:n)/5e22,D(1:n),'x',Cge(1:n)/5e22,absD,'r');
title('D vs Ge fraction'); xlabel('X_G_e');ylabel('D cm2/sec');
axis tight;
 grid;
 %%%% save D(x) data %%%%%%%%
Cge=Cge';
Xge=Cge/5e22;
D=abs(D');
data=[Xge D];
save Xge_D_BM20A_920_less_noise.txt data -ASCII -tabs;
```

Appendix F The effect of initial condition of interdiffusion

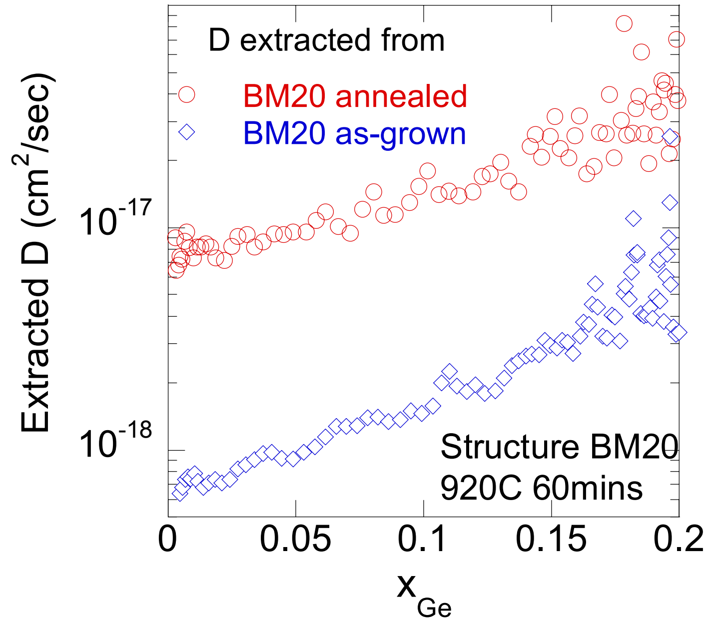

Figure F-1 Interdiffusivity extracted from as-grown BM20 and annealed BM20 structures.

After the discussion on Boltzmann-Matano assumptions and the SIMS broadening effects, careful readers might ask whether the measured as-grown Ge profile is the true Ge profile, and whether the Boltzmann-Matano analysis is still valid. These are questions to be addressed in this Appendix. Figure 3-7 shows the as-grown and annealed SIMS profiles of structure BM20. In the calculation of the interdiffusivity using Boltzmann-Matano analysis, only the annealed profile was used, assuming the starting profile is a perfect step. To check the error associated with this assumption, it is necessary to create a time scale for the diffusion. Assume at $t = 0$, the starting profile is a perfect step. At 920 ºC, we let it diffusion for time $t1$, resulting in the as-grown SIMS profile. Also at 920 ºC,

at t = $t2$, it diffuses to the position of the annealed SIMS profile. In the Boltzmann-Matano analysis, only the annealed SIMS profile was used, and it was assumed that diffuses from the perfect step profile for a time t = $t2$. If in fact, the starting profile is closer to the measured SIMS profile, then the effective time of diffuses should be $t=t2-t1$. Then, the extracted diffusivity is overestimated by a factor of $\frac{t2}{t2-t1}-1=\frac{1}{\frac{t2}{t1}-1}$, where $t2$ is the nominal diffusion time of the annealing experiment.

In order to find the ratio of $t1$ to $t2$, we need to measure how much Dt is associated with the sloped as-grown and annealed SIMS profiles. Since D should be the same for both profiles (assuming time independent D), then $\frac{D*t1}{D*t2}=\frac{t1}{t2}$. In order to obtain the Dt ratio, we extracted D' from the as-grown SIMS profile as if it is a diffused profile from a perfect step under the same annealing condition. Then we compared D' with D extracted from the annealed profile. As shown in Figure F-1, D' is about 10% of D. and $D*t1$ is about 10% of $D*t2$. In other words, $\frac{t1}{t2}=0.1$. The overestimation factor is $\frac{1}{\frac{t2}{t1}-1}=11\%$, which means by assuming the starting profile is a perfect step will only overestimate the diffusivity by about 10% in extraction, which significantly smaller than other sources of error in the extracted diffusivity.

Appendix G SIMS noise and Matano plane position

This Appendix discusses several issues related to the interdiffusivity extraction technique and experimental artifacts. In Figure G-1 (b), we removed the spikes in apparent diffusivity at low Ge fractions, which are due to the SIMS noise at very low Ge fractions. SIMS noise at the maximum, constant Ge fraction introduces another spike such as the spike at 20% for the BM20 structure. Since the raw SIMS data is fairly noisy, in the Matlab code, the SIMS data was smoothed to generate interdiffusivity curves with less noise, as illustrated in Figure G-2.

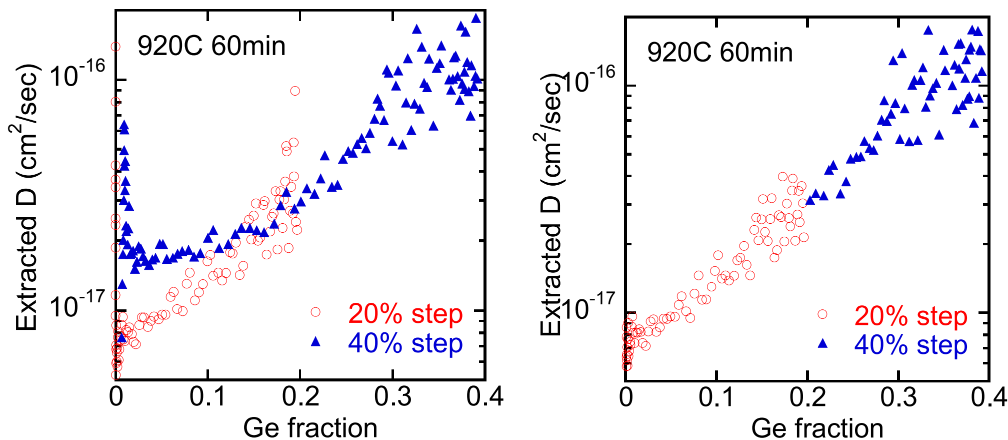

Figure G-1 (a) unprocessed extracted interdiffusivity from SIMS profiles of BM20 and BM40 structures (structures illustrated in Figure 3-7)**, and (b) processed interdiffusivity with the low x_{Ge} data blocked for the BM40 structure.**

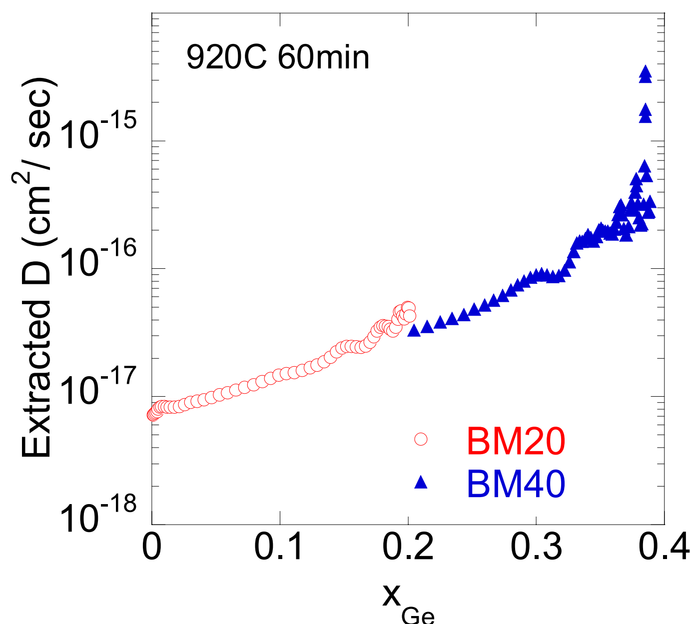

Figure G-2 Extracted interdiffusivity from smoothed SIMS profiles of BM20 and BM40 structures (structures illustrated in Figure 3-7)**.**

Another important source of error is the position of the Matano plane. As seen in Equation 3-6, z_M has significant influence to the interdiffusivity results. At the same time, since z_M is determined by the shape of diffused profile, it is not easy to find the exact position. Especially in SiGe system, the profile approaches a constant level very slowly due to the strong dependence of interdiffusivity on Ge fraction. In one SIMS job performed by Evans Analytical Group, it is possible to profile with high depth resolution to a certain depth. Therefore, it is possible that the profiling stopped before reaching a truely constant Ge concentration. It is even harder to tell whether the SIMS profiling depth is enough when there is background noise involved. To evaluate the error introduced by the choice of Matano plane, sample BM60B was analyzed under different conditions. The extracted interdiffusivity results were compared by varying the position

of z_M. Figure G-3 (a), (b) and (c) show the integral term $\int_{C_L}^{C'}(z - z_M)dC$ as a function of C'

(which is Ge concentration) for different values of z_M to indicate the cases where the integral is significantly larger than 0, close to 0 and significantly less than 0. As seen in Figure G-4, the position of z_M shifts the interdiffusivity curves up and down with similar shape. The cases in Figure G-3 (a) and (c) are considered the worst-case scenarios where the integral is far from zero. The diffusivities associated with these large shifts in z_M are within a factor of 3X of the diffusivity extracted with an accurate determination of z_M, as seen in Figure G-4.

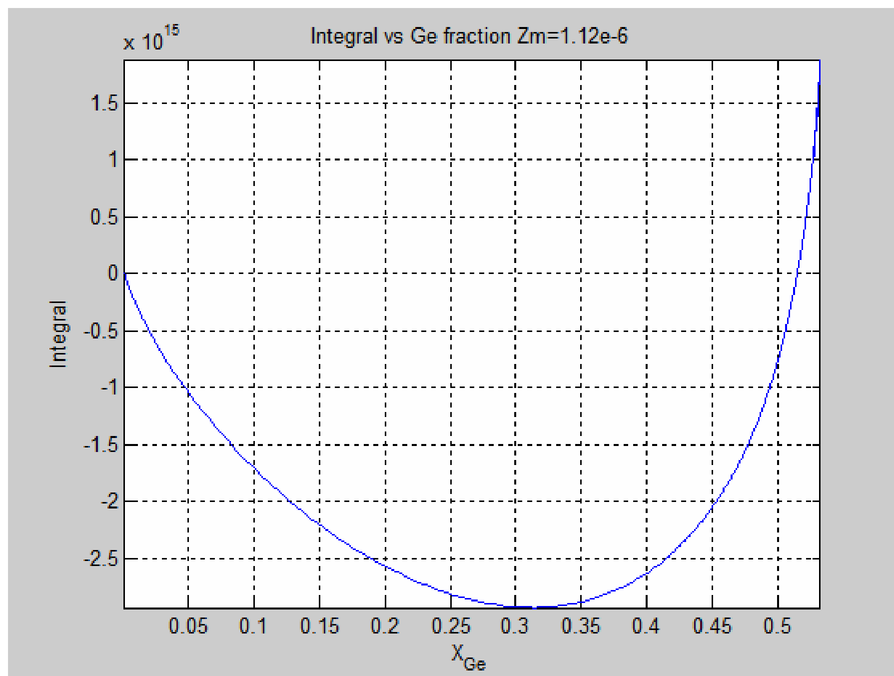

(a) z_M=112A

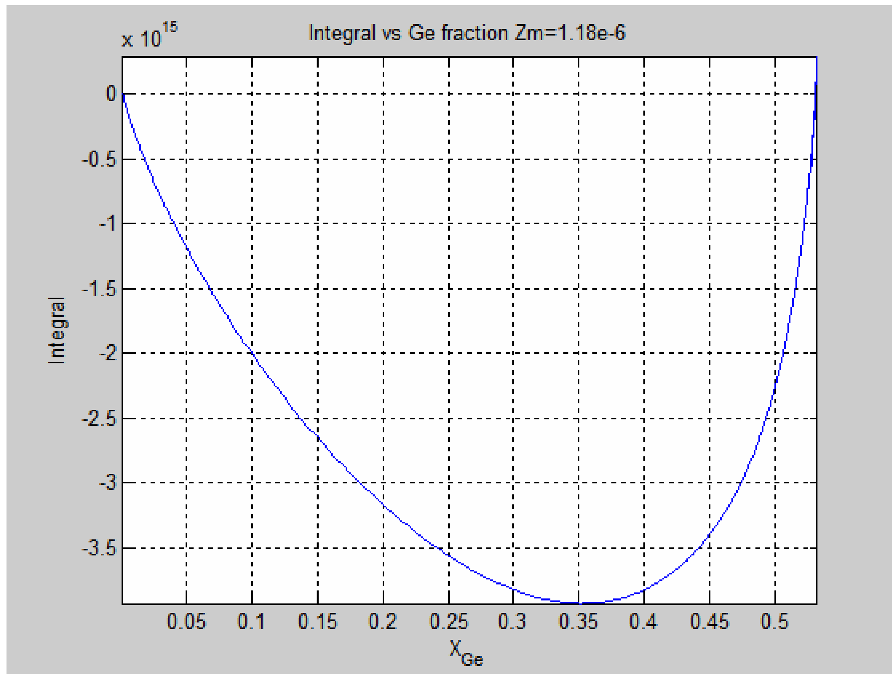

(b) z_M =118A

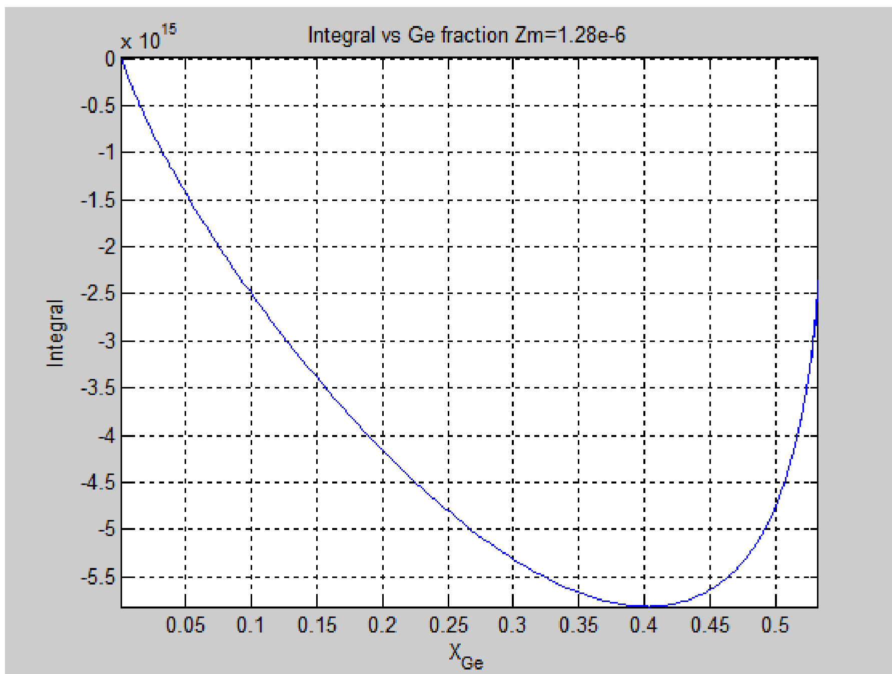

(c) z_M =128A

Figure G-3 Integrals for different z_M =112A, 118A and 128A.

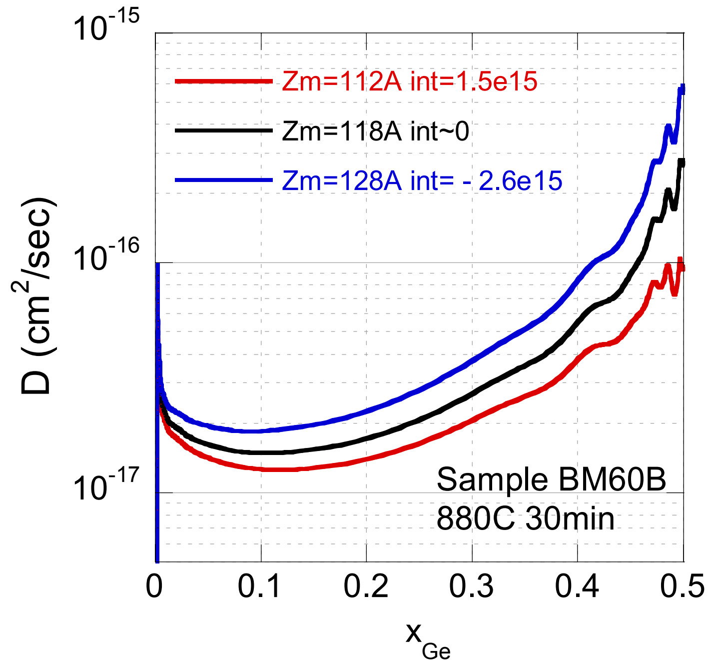

Figure G-4 Interdiffusivity curves extracted from BM60B annealed profile with different z_M values.

Appendix H Calculation of Thermal Mismatch Strain

So far, the thermal mismatch strain of different layers has been ignored. In this section, the upper limit of the magnitude of thermal mismatch strain is estimated, and is shown to be small enough to be safely ignored.

V. V. Zhdanova et al. studied the thermal expansion coefficient α of $Si_{1-x}Ge_x$, and showed that for $x < 0.85$ at 300 K [68]

$$\alpha = (2.6 + 2.55x) * 10^{-6}\ K^{-1} \qquad \text{Equation H-1}$$

For temperatures higher than 300 K, the dependence on x is smaller. The thermal mismatch strain due to different thermal expansion coefficient of strained Si and SiGe

layers can be expressed as

$$\varepsilon_{th} = \int_{T1}^{T2} (\alpha_{SiGe} - \alpha_{Si}) dT \qquad \text{Equation H-2}$$

in which T1 is the epitaxial growth temperature and T2 is room temperature, 300 K. The thermal mismatch strain after cooling down to 300 K is negative (compressive strain), since the thermal expansion coefficient of SiGe is larger than that of Si. The upper limit for the absolute value of ε_{th} is:

$$|\varepsilon_{th}| < \max(\alpha_{SiGe} - \alpha_{Si}) * (T1 - T2) \qquad \text{Equation H-3}$$

In this work T1 is about 525 to 600 ºC. The maximum difference between the two thermal expansion coefficients is at 300 K and between Si layer and the highest concentration 60% SiGe layer, which is about 2 x 10^{-6} K^{-1}. Substituting these numbers into Equation H-3, we have

$$|\varepsilon_{th}| < 2x10^{-6} * (600 - 300) = 0.06\% \qquad \text{Equation H-4}$$

The upper limit of thermal mismatch strain is 0.06%, equivalent to a difference in substrate Ge fraction, x_0 of 1.5 atomic %. Thus, the thermal mismatch strain is within the error bar of this work, and can be safely ignored.

Appendix I Ge dose conservation in TSUPREM-4 simulation

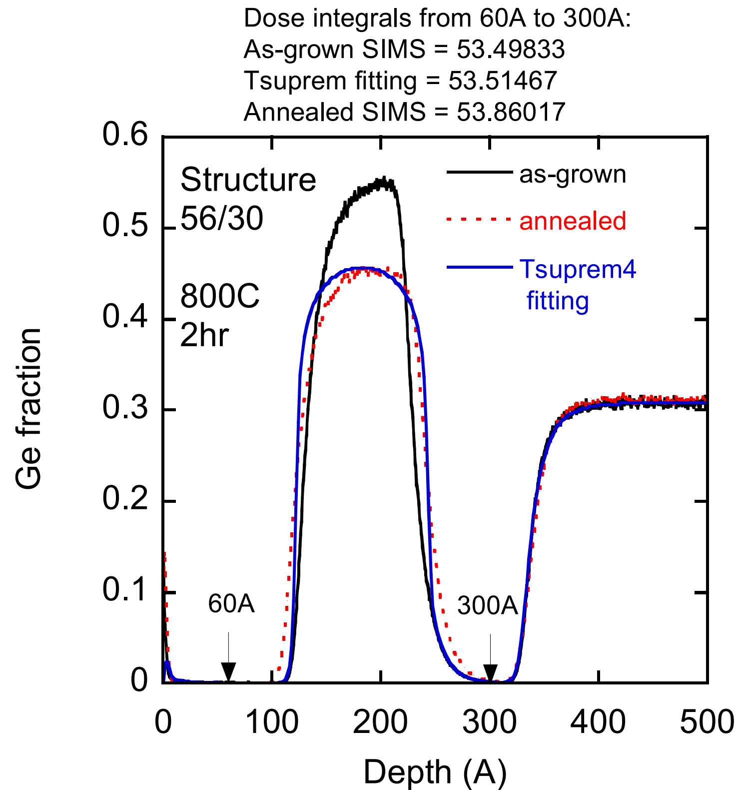

Figure I-1 Example of Ge dose conservation. The structure is 56/30. The as-grown and annealed Ge profiles were measured by SIMS.

As mentioned in Chapter 3, the thermal budgets are designed such that the diffusion fronts won't reach the surfaces. The reason for that is to approximate the infinite long diffusion couple assumption of Boltzmann-Matano analysis, and also to avoid surface transport phenomenon such as Ge evaporation. In this section, Ge dose conservation is confirmed. As-grown, annealed and simulated post-annealed Ge profiles are shown in Figure I-1. The Ge doses of the peaks were integrated over the depth from 60 to 300 A. The Ge doses for as-grown, annealed and simulated post-annealed Ge profiles are 53.498, 53.860, and 53.514 respectively. The initial profile used in TSUPREM-4 simulation is the as-grown SIMS profile. The fact that the Ge doses for the as-grown and simulated post-

annealed profiles are very close (53.498 and 53.514) is not surprising, since TSUPREM-4 conserves the dose of diffusing species. In the experiments, the as-grown and annealed samples of one structure are taken from different areas of one wafer. Samples are normally 10 mm by 10 mm in size, and the area analyzed by SIMS is typically 200 x 200 μm. Any non-uniformity in the epitaxial growth process, together with SIMS errors can contribute to a Ge dose difference in the as-grown and annealed SIMS profiles. From Figure I-1, we see the as-grown and annealed SIMS profiles have close Ge doses (53.498 and 53.860 respectively), which shows good epitaxial uniformity. Figure I-2 shows another set of data for structure 56/15, which gives another evidence of good epitaxial uniformity in the integrated Ge dose.

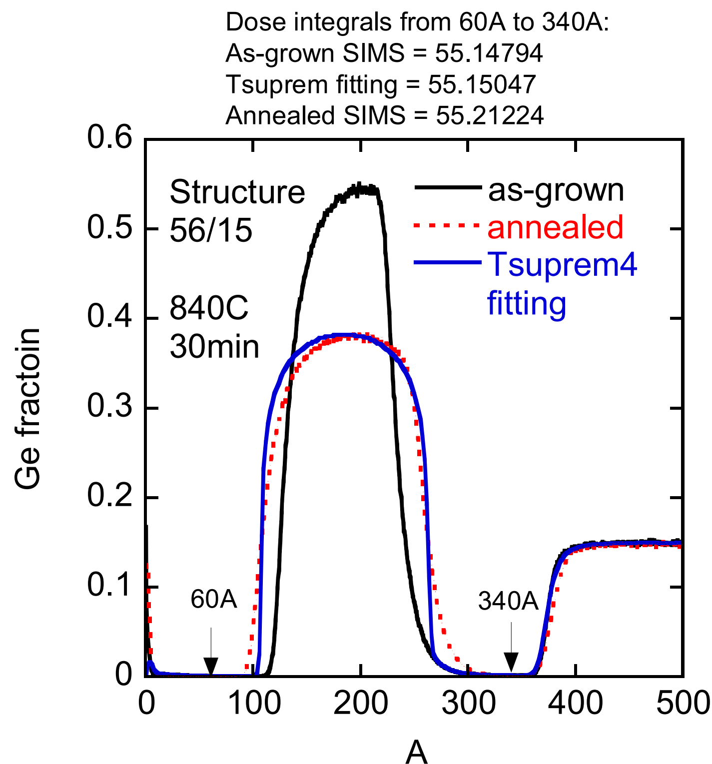

Figure I-2 Another example of Ge dose conservation. The structure is 56/15.

Appendix H TSUPREM-4 Source Code for Interdiffusion Simulation

```
$------------------------------------
line x loc=0     spacing=0.1
line x loc=0.01 spacing=0.01
line y loc=-0.02          spacing=0.0001
line y loc=0.06           spacing=0.0001
line y loc=0.13           spacing=0.0100
line y loc=0.2  spacing=0.0100
init boron=5e16 material=silicon
$------------------------------------
impurity name=Ge new
method variable=Ge none abs.err=0.1
profile impurity=Ge inf="60on30step.txt"
$$$ 60on30step.txt is used because SIMS data for as-grown profile is unavailable
select z=Ge title='singleslope-compressive T=900C 10sec RTA'
plot.1 x.min=0.0 x.max=0.04 y.min=0  y.max=3.2e22
label x=0.015 y=2.8e22 label="b1=8.1 b2=23 Xge0=0.30"
label x=0.015 y=2.7e22 label="30A and 100A thickness"

intermed name=Xge express=Ge/5e22
intermed name=Xge0 value=0.30

intermed name=b1 value=8.1
intermed name=b2 value=23
intermed name=D00 value=310
intermed name=Eav value=4.66
intermed name=D01 express=D00*exp(-Eav/kT)

intermed name=D02 value=D01*exp(b1*Xge0)
intermed name=D express=(Xge<=Xge0 ? D01*exp(b1*Xge):D02*exp(b2*(Xge-Xge0)))


equation variable=Ge mat=Si +
addtoexp=DIV(D*GRAD(Ge))

diffusion temp=900 time=10/60 inert
sel z=Ge
plot.1 ^axis ^clear color=2 line.typ=1

SELECT Z=Ge
EXTRACT OUT.FILE=annealed900C-60on30.txt +
PREFIX="% Ge profile simulated"
FOREACH DEPTH (0 TO 0.08 STEP 0.0002)
EXTRACT SILICON X=0.0 DISTANCE=@{DEPTH} +
```

```
Y.EXT VAL.EXT
END
EXTRACT CLOSE


label x=0.013 y=.6e22 label="60/30 as-grown-step" c.line=1 line.typ=1
label x=0.013 y=.4e22 label="singleslope model prediction" c.line=2 line.typ=1
```

Bibliography:

[1] S. Ito, H. Namba, K. Yamaguchi, T. Hirata, K. Ando, S. Koyama, S. Kuroki, N. Ikezawa, T. Suzuki, T. Saitoh, and T. Horiuchi, "Mechanical Stress Effect of Etch-Stop Nitride and its Impact on Deep Submicron Transistor Design," in *IEDM Tech. Dig.*, 2000, pp. 247-250.

[2] A. Shimizu, K. Hachimine, N. Ohki, H. Ohta, M. Koguchi, Y. Nonaka, H. Sato, and F. Ootsuka, "Local Mechanical-Stress Control (LMC): A New Technique for CMOS-Performance Enhancement," in *IEDM Tech. Dig.*, 2001, pp. 433-436.

[3] T. Ghani, M. Armstrong, C. Auth, M. Bost, P. Charvat, G. Glass, T. Hoffmann, K. Johnson, C. Kenyon, J. Klaus, B. McIntyre, K. Mistry, A. Murthy, J. Sandford, M. Silberstein, S. Sivakumar, P. Smith, K. Zawadzki, S. Thompson, and M. Bohr, "A 90 nm high volume manufacturing logic technology featuring novel 45 nm gate length strained silicon CMOS transistors," in *IEDM Tech. Dig.*, 2003, pp. 978-980.

[4] V. Chan, R. Rengarajan, N. Rovedo, Jin Wei, T. Hook, P. Nguyen, Jia Chen, E. Nowak, Xiang-Dong Chen, D. Lea, D. Chakravarti, A. Ku, V. Yang, S. Steegen, A. Baiocco, C. Shafer, P. Hung Ng, Shih-Fen Huang, C. Wann, "High speed 45nm gate length CMOSFETs integrated into a 90nm bulk technology incorporating strain engineering" in *IEEE IEDM Tech. Dig.*, 2003, page 3.8.1- 3.8.4

[5] Dick James, "2004 – The Year of 90-nm: A Review of 90 nm Devices 2005", IEEE/SEMI Advanced Semiconductor Manufacturing Conference.

[6] K. Uchida, R. Zednik, Ching-Huang Lu, H. Jagannathan, J. McVittie, P. C. McIntyre, Y. Nishi, “Experimental study of biaxial and uniaxial strain effects on carrier mobility in bulk and ultrathin-body SOI MOSFETs” in *IEEE IEDM Tech. Dig.*, 2004, pp. 229 – 232.

[7] K. Rim, J. L. Hoyt, and J. F. Gibbons, "Transconductance enhancement in deep submicron strained Si n-MOSFETs," in *IEEE IEDM Tech. Dig.*, 1998, pp. 707-710.

[8] C. W. Leitz, M. T. Currie, M. L. Lee, Z. -Y. Cheng, D. A. Antoniadis, and E. A. Fitzgerald, “Hole mobility enhancements in strained Si/$Si_{1-y}Ge_y$ p-type metal-oxide-semiconductor field effect transistors grown on relaxed $Si_{1-x}Ge_x$ $(x<y)$ virtual substrates,” *Appl. Phys. Lett.*, vol. 79, pp. 4246-4248, 2001.

[9] J. Jung, M. L. Lee, S. Yu, E. A. Fitzgerald, and D. A. Antoniadis,“Implementation of both high-hole and electron mobility in strained Si/strained $Si_{1-y}Ge_y$ on relaxed $Si_{1-x}Ge_x$ $(x<y)$ virtual substrate,” *IEEE Electron Device Lett.*, vol. 24, pp. 460-462, 2003.

[10] M. L. Lee and E. A. Fitzgerald, “Optimized strained Si/strained Ge dual-channel heterostructures for high mobility P- and N-MOSFETs,” in *IEDM Tech. Dig.*, 2003, pp. 429-43

[11] K. Rim, K. Chan, L. Shi, D. Boyd, J. Ott, N. Klymko, F. Cardone, L. Tai, S. Koester, M. Cobb, D. Canaperi, B. To, E. Duch, I. Babich, R. Carruthers, P. Saunders, G. Walker, Y. Zhang, M. Steen, and M. Ieong, “Fabrication and mobility characteristics of ultra-thin strained Si directly on insulator (SSDOI) MOSFETs,” in *IEDM Tech. Dig.*, 2003, pp. 47-52.

[12] I. Åberg, C. Ní Chléirigh, O.O. Olubuyide, X. Duan, and J.L. Hoyt, “High electron and hole mobility enhancements in thin-body strained Si/strained SiGe/strained Si heterostructures on insulator,” in *IEDM Tech. Dig.*, 2004, pp.173-176.

[13] T. Mizuno, N. Sugiyama, A. Kurobe, and S. Takagi, “Advanced SOI p-MOSFETs with strained-Si channel on SiGe-on-insulator substrate fabricated by SIMOS technology,” *IEEE Trans. Electron Devices*, vol. 48, pp. 1612-1618, Aug. 2001.

[14] Zhiyuan Cheng, Matthew T. Currie, Chris W. Leitz, Gianni Taraschi, and Eugene A. Fitzgerald, Judy L. Hoyt, and Dimitri. A. Antoniadis, “Electron mobility enhancement in strained-Si n-MOSFETs fabricated on SiGe-on-insulator (SGOI) substrates”, *IEEE Electron Device Lett*., vol 22, issue 7, pp. 321 –323, July 2001.

[15] E. A. Fitzgerald, Y. H. Xie, D. Monroe, P. J. Silverman, J. M. Kuo, A. R. Kortan, F. A. Thiel, and B. E. Weir, “Relaxed Ge/sub x/Si/sub 1-x/ structures for III-V integration with Si and high mobility two-dimensional electron gases in Si,” *Journal of Vacuum Science & Technology B (Microelectronics Processing and Phenomena)*, vol. 10, pp. 1807, 1992.

[16] J. Welser, J. L. Hoyt, and J. F. Gibbons, “NMOS and PMOS transistors fabricated in strained silicon/relaxed silicon-germanium structures”, in *IEDM Tech. Dig*., 1992, pp. 1000-1002.

[17] J. Welser, J. L. Hoyt, S. Takagi, and J. F. Gibbons, “Strain dependence of the performance enhancement in strained-Si n-MOSFETs,” in *IEEE IEDM Tech. Dig*., 1994, pp. 947.

[18] K. Rim, J. Welser, J. L. Hoyt, and J. F. Gibbons, “Enhanced hole mobilities in surface-channel strained-Si p-MOSFETs,” in *IEEE IEDM Tech. Dig*., 1995, pp. 1026.

[19] S. Takagi, A. Toriumi, M. Iwase, and H. Tango, "On the universality of inversion layer mobility in Si MOSFET's: Part I — effects of substrate impurity concentration," *IEEE Trans. Electron Devices*, vol. 41, pp. 2357-2362, Dec. 1994.

[20] K. Rim, S. Koester, M. Hargrove*, J. Chu, P. M. Mooney, J. Ott, T. Kanarsky", P. Ronsheim*, M. Ieong", A. Grill, H.-S. P. Wong, "Strained Si NMOSFETs for High Performance CMOS Technology" in *Symp. VLSI Tech. Dig.,* 2001, pp. 59-60

[21] T Tezuka, N Sugiyama, T Mizuno, S Takagi, "High-performance strained Si-on-insulator MOSFETs by novel fabrication processes utilizing Ge-condensation technique", in *Symp. VLSI Tech. Dig*., 2002, pp. 96- 97.

[22] M. T. Currie, C. W. Leitz, T. A. Langdo, G. Taraschi, E. A. Fitzgerald, and D. A. Antoniadis, "Carrier mobilities and process stability of strained Si n- and p-MOSFETs on SiGe virtual substrates," *J. Vac. Sci. Technol. B*, vol 19(6), pp. 2268-2279, Nov/Dec. 2001.

[23] J. L. Hoyt, H. M. Nayfeh, S. Eguchi, I. Aberg, G. Xia, T. Drake, E. A. Fitzgerald, D. A. Antoniadis, " Strained silicon MOSFET technology", in *IEEE IEDM Tech. Dig*., 2002, pp. 23-26.

[24] T. Vogelsang and K. R. Hofmann, "Electron transport in strained Si layers on Si/sub 1-x/Ge/sub x/ substrates," Applied Physics Letters, vol. 63, pp. 186-8, 1993.

[25] K. Rim, S. Narasimha, M. Longstreet, A. Mocuta, and J. Cai, "Low Field Mobility Characteristics of Sub-100 nm Unstrained and Strained Si MOSFETs," in *IEDM Tech. Dig.,* 2002, pp. 43-46.

[26] C. G. Van de Walle and R. M. Martin, "Theoretical calculations of heterojunction discontinuities in the Si/Ge system," *Physical Review B (Condensed Matter)*, vol. 34, pp. 5621-34, 1986.

[27] C. Zeller and G. Abstreiter, "Electric subbands in Si/SiGe strained layer superlattices," *Zeitschrift fur Physik B (Condensed Matter)*, vol. 64, pp. 137-43, 1986.

[28] M. V. Fischetti, F. Gámiz, and W. Hansch, "On the enhancement electron mobility in strained-silicon inversion layers", *J. Appl. Phys*., vol. 92, pp 7320-7324, Dec. 2002.

[29] J. W. Matthews and A. E. Blakeslee, "Defects in epitaxial multilayers. I. Misfit dislocations," *J. of Crystal Growth*, vol. 27, pp. 118-25, 1974.

[30] D. Misar, P. K. Swain, "Strain relaxation in SiGe due to process induced defects and their subsequent annealing behavior", *Microelectronics Reliability*, vol 38, pp. 1611-1619, 1998.

[31] D. C. Houghton, "Strain relaxation kinetics in Si/sub 1-x/Ge/sub x//Si heterostructures," *J. of Appl. Phys.*, vol. 70, pp. 2136-51, 1991.

[32] S. B. Samavedam, W. J. Taylor, J. M. Grant, J. A. Smith, P. J. Tobin, A. Dip, A. M. Phillips, and R. Liu, "Relaxation of strained Si layers grown on SiGe buffers" *J. Vac. Sci. Technol. B*, vol 17, pp. 1424-1429, July 1999.

[33] R. Hull, J. C. Bean, J. M. Bonar, G. S. Higashi, K. T. Short, H. Temkin, and A. E. White, "Enhanced strain relaxation in Si/GexGe1-x/Si heterostructures via point-defects concentrations introduced by ion implantation," *Appl. Phys. Lett.*, vol 56(24), pp2445-2447, June 1990.

[34] B. Hollander, St. Lenk, S. Mantl, H. Trinkaus, D. Kirch, M. Luysberg, T. Hackbarth, H. J. Herzog, and P. F. P. Fichter, "Strain relaxation of pseudomorphic Si1-xGex/Si(100) heterostructures after hydrogen or helium ion implantation for virtual substrate fabrication," *Nucl. Instr. And Meth. in Phys. Res. B*, vol 175-177, pp357-367, 2001.

[35] H. M. Nayfeh, C.W. Leitz, A. J. Pitera, E. A. Fitzgerald, J. L. Hoyt, and D.A. Antoniadis, "Influence of high channel doping on the inversion layer electron mobility in

strained silicon n-MOSFETs", *IEEE Electron Device Lett.*, vol 24, pp.248 -250. April 2003

[36] P. M. Rousseau, P. B. Griffin, S. Luning, and J. D. Plummer, "A model for mobility degradation in highly doped arsenic layers," *IEEE Trans. Elec. Dev.*, vol 43, pp. 2025-2027, Nov. 1996.

[37] J. D. Plummer, M. D. Deal and P. B. Griffin, *Silicon VLSI Technology - Fundamentals, Practice and Modeling*, New Jersy: Prentice Hall, 2000, ch. 8.

[38] G. Abstreiter, H. Brugger, T. Wolf, H. Jorke, and H. J. Herzog, "Strain-induced two-dimensional electron gas in selectively doped Si/$Si_{1-x}Ge_x$ superlattices," Phys. Rev. Lett., vol. 54, pp. 2441–2444,1985.

[39] M. I. Alonso and K. Winer, "Raman spectra of c-$Si_{1-x}Ge_x$ alloys," Phys. Rev. B, Condens. Matter, vol. 39, no. 14, pp. 10056–10062, May 1989.

[40] *TSUPREM-4, version 200*2, Synopsys, Inc., Mountain View, CA, 2003.

[41] M. A. Armstrong, Ph.D. thesis, Massachusetts Institute of Technology, 1999.

[42] G. Höck, E. Kohn, C. Rosenblad, H. von Känel, H.-J. Herzog, and U. König, *Appl. Phys. Lett.* **7**6, 3920 (2000).

[43] Jongwan Jung, Shaofeng Yu, Minjoo L. Lee, Judy L. Hoyt, Eugene A. Fitzgerald,and Dimitri A. Antoniadis, *IEEE Transactions on Electron Devices* **5**1, 1424 (2004).

[44] I. Åberg, C. Ní Chléirigh, O.O. Olubuyide, X. Duan, and J.L. Hoyt, "High Electron and Hole Mobility Enhancements in Thin-Body Strained Si/Strained SiGe/Strained SI Heterostructure on Insulator", *IEDM Tech. Dig*. **200**4, 173 (2004).

[45] Jongwan Jung, Shaofeng Yu, Oluwamuyiwa Oluwagbemiga Olubuyide, Judy L. Hoyt, Dimitri A. Antoniadis, Minjoo L. Lee and Eugene A. Fitzgerald, "Effect of thermal processing on mobility in Strained Si/strained SiGe on relaxed SiGe virtual substrates"*Appl. Phys. Lett.* **8**4, 3319 (2004).

[46] John Hennessy, private communication

[47] D. B. Aubertine, M . A. Mander, N. Ozguven, A. F. Marshall, P. C. McIntyre, J. O. Chu, and P. M. Mooney, "Observation and Modeling of the Initial Fast Interdiffusion Regime in Si/SiGe Multilayers"J. of Appl. *Phys*. **9**2, 5027 (2002).

[48] D. B. Aubertine, and P. C. McIntyre, "Influence of Ge Concentration and Compressive Biaxial Stress on Interdiffusion in Si-Rich SiGe Alloy Heterostructures" *J. Appl. Phys*. **9**7, 013531-1 (2005).

[49] N. E. B. Cowern, P. C. Zalm, P. van der Sluis, D. J. Gravesteijn, and W. B. de Boer, "Diffusion in strained Si(Ge)"*Phys. Review Lett*. **7**2, 2585 (1994).

[50] A. Strohom, T. Voss, W. Frank, J. Raisanen, and M. Dietrich, "Self-diffusion of ^{71}Ge in Si–Ge"*Physica B*, **308-310**, 542 (2001).

[51] N. R. Zangenberg, J. L. Hansen, J. Fage-Pedersen, A. N. Larsen, "Ge Self-Diffusion in Epitaxial $Si_{1-x}Ge_x$ Layers"*Phys. ReviewLett*. **8**7, 125901-1 (2001).

[52] L. Boltzmann, *Wiedemanns Ann. Phys.*, 1894, vol. **5**3, p. 959.

[53] C. Matano, *Jpn. J. Phys.*, 1933, vol. 8, p. 109.

[54] C. L. Siu, H. C. Man, C. H. Yeung "Interdiffusion coefficients of various cobalt base alloy coatings for Cu/Au system", *Applied Surface Science* **24**5, 79 (2005).

[55] W. A. O. Arienzo, R. Glang, R. F. Lever, R. K. Lewis, F. F. Morehead, "Boron diffusion in silicon at high concentrations", *J. of Appl. Phys*. **6**3, 116 (1988).

[56] A. Sultan, S. Bhattacharya, S. Batra, and S. Banerjee, “Boltzmann-Matano analysis based model for boron diffusion from polysilicon into single crystal silicon” *Journal of Vacuum Science & Technology B (Microelectronics and Nanometer Structures)* **1**2, 391 (1994).

[57] D. P. Kennedy, P. C. Murley, “Concentration dependent diffusion of arsenic in silicon”, *Proceedings of the IEEE* **5**9, 335 (1971).

[58] P. M. Mooney, J. A. Ott, J. O. Chu, and J. L. Jordan-Sweet, “X-ray diffraction analysis of SiGe/Si heterostructures on sapphire substrates”, *Appl. Phys. Lett*. **7**3, 924 (1998).

[59] MIT course 3.205 “Thermodynamics and Kinetics of Materials” notes, http://ocw.mit.edu/OcwWeb/Materials-Science-and-Engineering /3-205Fall2003/LectureNotes/index.htm

[60] J.C. Tsang, P.M. Mooney, F. Dacol, J.O Chu, “Measurements of alloy composition and strain in thin Ge_xSi_{1-x} layers”, *J. Appl. Phys.* 75, p. 8098, 1994.

[61] M. J. Aziz, “Thermodynamics of diffusion under pressure and stress: Relation to point defect mechanisms”, *Appl. Phys. Lett*. **70,** pp. 2810 (1997).

[62] P. Laitinen, A. Strohm, J. Huikari, A. Nieminen, T. Voss, C. Grodon, I. Riihimäki, M. Kummer, J. Äystö, P. Dendooven, J. Räisänen, and W. Frank, “Self-Diffusion of 31Si and 71Ge in Relaxed Si0.20Ge0.80 Layers”, *Phys. Rev. Lett*. **89**, 085902 (2002).

[63] P. Fahey, S. S. Iyer, and G. J. Scilla, “Experimental evidence of both interstitial- and vacancy-assisted diffusion of Ge in Si”, *Appl. Phys. Lett*. **54,** p843 (1989).

[64] C. Ní Chléirigh, O. O. Olubuyide and J.L. Hoyt, "Mobility and Sub-threshold Characteristics in High-Mobility Dual-Channel Strained Si/Strained SiGe p-MOSFETs", Tech. Dig. Device Research Conference, 2005

[65] Cait Ni Chleirigh, private communication.

[66] M. J. Aziz, Y. Zhao, H- J. Gossmann, S. Mitha, S. P. Smith, and D. Schiferl, " Pressure and stress effect on the diffusion of B and Sb in Si and Si-Ge alloys", Phys. Rev. B, 73, p054101 (2006).

[67] P. Rananarayanan, B. Srinivasan, K. Cho, and B. Clemens, "Migration energy for impurity diffusion in crystalline solids: a closer look", J. of Appl. Phys. 96, p7095 (2004).

[68] Zhdanova, V.V., M.G. Kakna, T.Z. Samadashvili, *Izv. Akad. Nauk. SSSR Neorg. Mater.* **3** , 1967, p1263.